1

CHAPTER 1: INTRODUCTION

1-1 BACKGROUND

The continuous casting of metals is not a very old process in the manufacturing process. The continuous strip casting process was conceived by Henry Bessemer in 1858 but only became widespread in the 1960s [1]. The continuous casting process however increased significantly since then and now, most basic metals are mass-produced using a continuous casting process. In 1992, continuous casting was used to produce over 90% of steel in the world, including carbon, alloy and stainless steel grades [2]. In 2001 over 500 million tons of steel, 20 million tons of aluminium and 1 million tons of copper, nickel and other metals were produced in a continuous casting process [1]. It is estimated that the total world production of crude steel will increase to over 900 million tons per year in 2010 with steel produced by continuous casting still making up 90% of this production [2].

A graphic representation of the continuous casting process is given in Figure 1-1 [3]. This figure shows the different entities of the continuous casting process. These entities are:

- the ladle and shroud,
- the tundish,
- the submerged entry nozzle (SEN) and mould and
- the solidifying strand and slab.

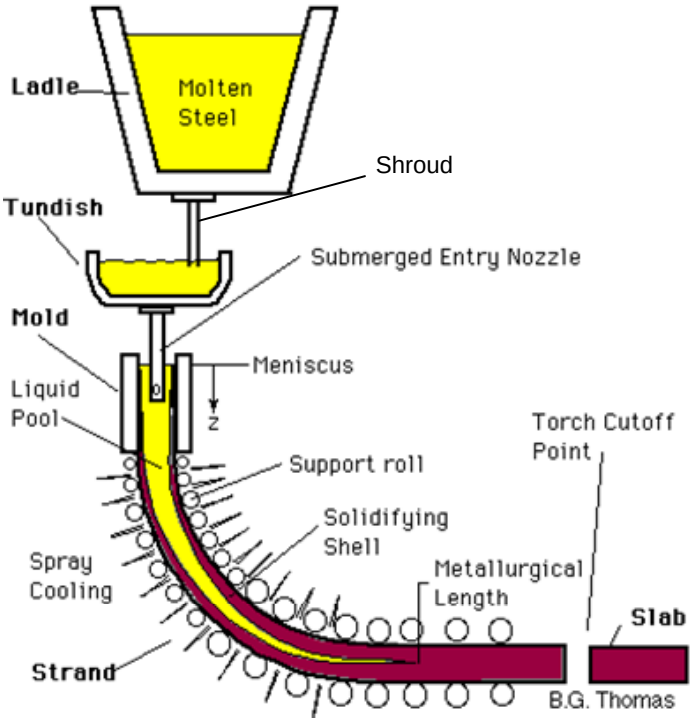

Figure 1-1: Schematic representation of the continuous casting process [3]

The continuous casting process will now be briefly described [4]. Scrap metal and ore are melted in a furnace (typically either in a basic oxygen furnace or an electric arc furnace) upstream of the continuous caster. The steel is then poured from the furnace into a ladle where it undergoes different metallurgical processes before it reaches the continuous caster, i.e., excess oxygen is removed from the molten steel in a vacuum degasser, and second-metallurgy stations ensure the correct composition of the steel. The steel is shielded from the air by using a slag cover on top of the molten steel.

The ladle is then brought to the continuous caster where the steel is poured from the ladle through a ceramic nozzle called the shroud into the tundish. The shroud is used to shield the steel from the air when steel flows from the ladle to the tundish. A control valve at the outlet of the ladle controls the flow rate into tundish. The liquid steel is again shielded from the air by a slag layer to prevent oxidation that would form detrimental oxide inclusions in the steel.

The molten steel flows through the tundish and exits the tundish through the submerged entry nozzle (SEN) into a bottomless mould. The walls of the mould,

usually made of copper, are water-cooled, which causes the steel to solidify on the sides. The sides of the mould are usually oscillating to prevent "sticking" of the steel to the sides of the mould.

Drive rollers lower in the casting machine continuously withdraw the solidifying shell from the mould. The speed of the rollers is set so that the material exiting the mould matches that of the incoming flow into the tundish so that the caster runs in steady state most of the time. Water jets sprayed on the strand, as it exits the mould, cools the strand further, causing the solidifying shell to grow to the core of the strand. The supporting rollers hold the strand in place as the core of the strand solidifies. The core of the strand continues to solidify for a significant length after exiting the mould. The point where the whole slab is fully solidified can be in the order of tenths of meters downstream of the mould.

The solidified strand at the end of the rollers is then cut into slabs by a torch. These slabs are then processed further, e.g., the slabs are hot and cold rolled into sheets, bars, rails and other shapes.

Because of the nature of the continuous casting process, the tundish has traditionally acted purely as a reservoir when one ladle is emptied and when a new ladle is brought into place. In the last couple of decades, the role of the tundish in the continuous casting process has evolved from that of a reservoir between the ladle and mould to being a grade separator, an inclusion removal device and a metallurgical reactor. For both grade separation and inclusion removal, the flow patterns inside the tundish play an important role. For the former, the flow patterns determine the amount of mixing that occurs, while for the latter, the paths of inclusion particles are influenced by the flow field. Several tundish designs and tundish devices or furniture exist that have as their aim the modification of tundish flow patterns, to either minimize mixed-grade length during transition, and/or to increase inclusion particle removal by the slag layer.

At the initiation of this study, steel producing plants in South Africa are experiencing difficulties with more economical and higher quality steel production in the

continuous casting process. Tons of steel are downgraded or scrapped at continuous casting plants. The typical difficulties of these plants are:

- downgrading or scrapping of steel due to inclusions and slag entrainment in the ladle, tundish and mould,
- downgrading or scrapping of mixed-grade sections during grade transitions,
- downgrading or scrapping of first section of new cast,
- break-outs of the strand,
- nozzle clogging due to solidifying steel,
- low yield levels in the tundish when draining the tundish at the end of a sequence due to slag entrainment and vortex formation.

1-2 EXISTING KNOWLEDGE

Tundish design is traditionally performed through experimental plant trials or water modelling. For the former, due to the nature of the process, it is difficult to have an exact knowledge of the flow field. Indirect measurements such as copper traces and oxygen sensing give an indication of the residence time and inclusion particles present in the tundish. Water modelling on the other hand, provided that Reynolds number and Froude number similarity for steady-state conditions can be achieved [5,6,7,8], can provide more insight into the mixing characteristics. In order to include thermal effects however, water models require significant modification to address cases where buoyancy effects and natural convection plays a measurable role [9,10].

With the advent of powerful computers and fluid flow modelling software, Computational Fluid Dynamics (CFD) has become an alternative tool with which to assess different tundish designs [11,12,13,14]. Not only can the thermal effects be incorporated, but also every detail of the flow field becomes available for extracting measures of performance.

1-3 RESEARCH OBJECTIVES

The objectives of this study are to:

- develop a methodology for the design optimisation of tundish and tundish furniture,
- apply the methodology to the design of specific products used in the tundish in the South African continuous casting industry.

1-4 SCOPE OF THE STUDY

In this study, the focus is placed on the design of a tundish and the tundish furniture to improve the molten steel flow patterns. The method developed in this study will be applied to a single strand caster of Columbus Stainless Steel as well as the two strand continuous caster of ISCOR Vanderbijlpark. The optimisation methodology can however be extended to other areas of the continuous casting process as well as other fluid flow and heat transfer applications where CFD is used to analyse the design.

CFD as analysis tool only, has limitations in that the variation of many parameters require trial-and-error simulations of which the interpretation relies heavily on the insight of the modeller. This usually leads to non-optimal solutions and furthermore requires a lot of manual labour by the engineer doing the modelling. In this study, a more efficient method is developed which combines CFD with mathematical optimisation. This means that the design parameters become design variables and that the performance trends with respect to these variables are taken into account automatically by the optimisation algorithm. Using this method, an optimum design for the tundish and its furniture can be found.

1-5 ORGANISATION OF THE THESIS

The thesis consists of the following chapters:

- Chapter 2 gives the appropriate literature pertaining the modelling of tundishes and optimisation tools. This chapter describes the relevant theory behind physical modelling and numerical modelling of tundishes. The chapter also

gives the theory of two mathematical optimisation methods that will be used in the rest of the study.

- Chapter 3 then develops the methodology for optimising tundish furniture. This chapter looks at the different important aspects in the tundish and tundish furniture design using a mathematical optimisation method. The different steps involved in a mathematical optimisation study is given and it is shown how an optimisation method links with a commercial CFD code.
- Chapter 4 applies this methodology to four different case studies. The methodology developed in Chapter 3 is applied to these case studies to show that the optimisation methodology is a viable alternative in the design of tundish and tundish furniture.
- Chapter 5 gives the conclusions drawn form this study.
- Chapter 6 give recommendations and possibility of future research in this field.

2

CHAPTER 2: LITERATURE STUDY

2-1 INTRODUCTION

This chapter gives the literature pertaining to this thesis. The literature study is divided into two main parts. The first part is on the modelling and design of the tundish and tundish furniture. The second part provides a background to mathematical optimisation. The modelling and design section is divided into three main parts, i.e., physical modelling, plant trials and numerical modelling. The mathematical optimisation section describes the theory behind mathematical optimisation and a description of the different optimisers used in this thesis.

2-2 TUNDISH MODELLING AND DESIGN

2-2.1 The Continuous Casting Process

In the last couple of decades, the role of the tundish in the continuous casting process has evolved from that of a reservoir between the ladle and mould to being a grade separator, an inclusion removal device and a metallurgical reactor. For both grade separation and inclusion removal, the flow patterns inside the tundish play an important role. For the former, the flow patterns determine the amount of mixing that occurs, while for the latter, the paths of inclusion particles are influenced by the flow field. Several tundish designs and tundish devices or furniture exist that have as their aim the modification of tundish flow patterns, to either minimise mixed-grade length during transition, and/or to increase inclusion particle removal by the slag layer.

The modelling and design of the tundish and tundish furniture can be divided into three main categories, i.e., physical modelling, plant trials and mathematical modelling. These three categories will now be described in more detail.

2-2.2 Physical Modelling

Physical modelling has great benefits over doing plant trials, i.e.:

- It does not operate under such harsh environments under which the tundish operates in the plant (e.g., extreme high temperatures and almost no visual observations possible).
- It does not interfere with the production of the plant.
- It can be a lot more repeatable due to the more stringent control one has in the laboratory whereas in the plant there are other variables that cannot be controlled.

Most modelling is done using water as the fluid representing the liquid steel. This is due to the similarity of the kinematic viscosity of molten steel at typical temperatures inside the tundish and water at room temperature as shown in Table 2-1 [15].

Table 2-1: Physical properties of water at 20°C and steel at 1600°C [15]

	Water (20°C)	Steel (1600°C)
Molecular viscosity [kg/m·s]	0.001	0.0064
Density [kg/m^3]	1 000	7014
Kinematic viscosity [m^2/s]	1×10^{-6}	0.913×10^{-6}
Surface tension [N/m]	0.073	1.6

In reduced scale isothermal studies, dynamic and geometric similarities must be obeyed. Geometric similarity simply implies that every dimension in the scale model bears a fixed ratio to corresponding dimension in the full scale.

Dynamic similarity implies that the ratio of the different forces acting on a small fluid element must be the same in the scale model and in the full-scale version [16].

Considering dynamic similarity, the inertial, viscous and gravitational forces are of importance in tundish flows. These forces are characterised by two dimensionless numbers. The first is the Reynolds $\left(\mathrm{Re} = \frac{\rho UL}{\mu}\right)$ number that gives the ratio of the inertia forces to the viscous forces. The second is the Froude number $\left(\mathrm{Fr} = \frac{U^2}{gL}\right)$ that gives the ratio of the inertia forces to gravitational forces. When water at room temperature is used as the modelling fluid, matching of both Reynolds and Froude numbers is only possible using full-scale models. In reduced-scale models, either Reynolds or Froude numbers can be satisfied, but not both [17].

Full scale, as well as reduced scale, water modelling has been performed extensively [5,14,18,19,20]. In order to include thermal effects however, water models require significant modification to address cases where buoyancy effects and natural convection plays a measurable role [10, 21]. This makes the use of numerical modelling as discussed later, an attractive alternative.

To quantify the performance of the tundish, two different types of approaches have been commonly applied by researchers [16]:

1. the measurement of residence time distribution (RTD)
2. direct measurement of inclusion separation through aqueous simulation.

The residence time of fluid within a rector is defined as the time a single fluid element spends in the reactor vessel. The theoretical residence time is defined as:

$$\tau \equiv \frac{\text{Filled Volume of the tundish}}{\text{Volumetric flow rate of steel into the tundish}} \qquad (2\text{-}1)$$

Usually flow in any tundish is accompanied by a distribution of residence times for different fluid elements (i.e., some fluid elements stay longer while others spend shorter times within the tundish with respect to the theoretical residence time) [16]. These residence time distributions can be experimentally measured by injecting a tracer (pulse or continuous) at the inlet of the tundish and then dynamically measuring the concentration at the outlet using colourimetry, conductimetry, or spectrophotometry.

When injecting a pulse injection at time $t = 0$, a typical concentration profile at the outlet, also called the C curve [22], is obtained as shown in Figure 2-1 [23]. Typical C curves or Residence Time Distribution (RTD) for different dimensionless tundish widths are shown in this figure.

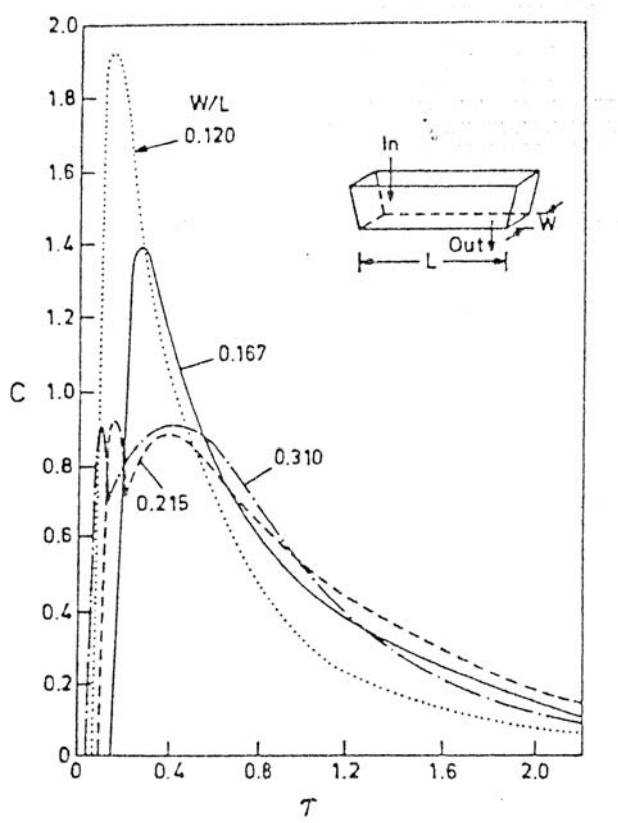

Figure 2-1: Typical measured RTD curve in a water model of a single strand slab casting tundish system at various values of the dimensionless tundish width [23]

From a typical RTD curve, different performance-related criteria for the tundish can be extracted. The values of the minimum break-through time ($\theta_{\min}$ in dimensionless form), time to attain the peak concentration (θ_{peak}), and the average residence time (θ_{av}) can be incorporated into an appropriate flow model to estimate the proportions of dead (V_{dv},) plug (V_{pv}), and well-mixed volumes (V_{mv}). The minimum break through time is also referenced to as the Minimum Residence Time (MRT). Kemeny *et al.* [15] proposed the various fractional volumes as:

$$\begin{aligned} V_{dv} &= 1-\theta_{av} \\ V_{pv} &= \theta_{\min} = \theta_{peak} \\ V_{mv} &= \frac{1}{C_{peak}} \end{aligned} \tag{2-2}$$

As pointed out by Sahai and Ahuja [6] this model has two shortcomings:

1. Considerable axial or longitudinal diffusion is present in tundish systems, causing the minimum break-through time and the time to reach the peak concentration not to be equal.
2. The three volume fractions do not add up to unity, which is a requirement for the mixed model.

Sahai and Ahuja [6] proposed a modified mixed model for tundish systems. Instead of dividing the tundish into a dead volume, plug-flow volume and well-mixed volume, they defined a dead volume, dispersed plug-flow volume (V_{dpv}) and a well-mixed volume as follows:

$$\begin{aligned} V_{dv} &= 1-\theta_{av} \\ V_{dpv} &= \frac{\left(\theta_{\min}+\theta_{peak}\right)}{2} \\ V_{mv} &= 1-V_{dv}-V_{dpv} \end{aligned} \tag{2-3}$$

Several investigators have also carried out direct measurement of particle removal in water models [24,25,26]. In these studies, hollow glass spheres were introduced into the tundish via the shroud. The exit particle

concentration was monitored with various techniques. Nakajama *et al.* [24] showed that any increase in the plug flow volume leads to an increase in the separation efficiency. This type of measurements however needs considerable hardware upgrades to an existing water model.

2-2.3 Plant Trials

The high temperature associated with the continuous casting process makes it very difficult to do on-site plant trials. Typical plant operations take a few discrete temperature measurements at regular intervals. Some tundishes have been instrumented to give on-line tundish wall temperatures [27]

A RTD curve can also be constructed by doing a copper trace trial. A copper dosage is introduced near the shroud of the tundish. Samples are then taken from the mould at regular intervals. These samples are then analysed for the copper concentration using a photo-spectrometer [28]. The principle of the analysis method is optical emission spectroscopy [29]. The sample material is vaporised by an arc. The atoms and ions contained in the atomic vapour are excited into emission of radiation. The radiation emitted is passed to the spectrometer optics via an optical fibre, where it is dispersed into its spectral components. From the range of wavelengths emitted by each element, the composition of the steel can be determined.

The last common practice to be used in plant trials is taking samples at the shroud and SEN to determine the number of inclusions present in the steel. Many measurement techniques exist to evaluate the steel cleanliness as given by Zhang *et al* [30]. The steel cleanliness at the shroud and SEN are then compared to each other to determine the efficiency of tundish in terms of particle removal.

As mentioned earlier, there are two major drawbacks of doing plant trials. Firstly, it interferes with production of the plant. Secondly, due to a large number of other uncontrollable parameters on the plant, the trials are

unrepeatable and therefore it is difficult to isolate the influence of certain parameters on the performance of the tundish.

2-2.4 Numerical Modelling

Computational Fluid Dynamics (CFD) is a numerical modelling technique that solves the Navier-Stokes equations on a discretised domain of the geometry of interest with the appropriate flow boundary conditions supplied. The Navier-Stokes equations are a complex non-linear set of partial differential equations that describes the mass and momentum conservation of a fluid. Additional physics can also be resolved by solving additional conservation equations, e.g., heat transfer, multi-phase flow, and combustion. A CFD analysis consists of the following steps [31]:

- Problem Identification and Pre-Processing
  - Define your modelling goals
  - Identify the domain you will model
  - Design and create the grid
- Solver Execution
  - Set up the numerical model
  - Compute and monitor the solution
- Post-Processing
  - Examine the results
  - Consider revisions to the model

Some of these steps will now be discussed in more detail.

2-2.4.1 Grid Generation

The grid generation process deals with the division of the domain under consideration into small control volumes on which the disretised governing equations will be solved.

The grid generation forms a large part in terms of person-hour time of the CFD analysis. A large amount of time has gone into and is currently going into the development of commercial automated grid

generators. Once such product is GAMBIT (Geometry and Mesh Building Intelligent Toolkit) [32]. GAMBIT uses solid modelling techniques to create a virtual model of the geometry under consideration. Various grid generation tools are available to create a grid in this geometry. The gird generation tools are available to create hexahedron, tetrahedron, prism and pyramid cells.

GAMBIT makes use of a Graphical User Interface (GUI) where the user is able to give commands to manipulate and generate the grid via the input of values and appropriate mouse clicks. An important aspect of GAMBIT with respect to mathematical optimisation is the parameterisation and automation of the set-up of the model and grid generation using journal files. A journal file is a text file that contains text commands that give the instructions to GAMBIT to generate a model without the use of the GUI.

2-2.4.2 Conservation Equations

The governing equations that describe the flow field are a set of non-linear partial differential equations. The equations are derived from mass, momentum and energy conservation. These three different governing equations will now be discussed briefly.

Conservation of Mass

The conservation of mass in Eulerian terms in its most common general form for fluids is given in the following [33]:

$$\frac{\partial \rho}{\partial t} + \mathrm{div}\rho \boldsymbol{V} = S_m \tag{2-4}$$

where ρ is the density, t is the time, $\boldsymbol{V}$ is the velocity vector of the fluid and S_m is a mass source. For a constant density, equation (2-4) simply reduces to the following:

$$\mathrm{div}\boldsymbol{V} = 0 \tag{2-5}$$

The constant density assumption can be made for tundishes when the temperature differences are not too large. The effect of the buoyancy

of the higher temperature steel is then treated through the Boussinesq model in the momentum transport equation. More detail on this model is given below.

Transport of Momentum

The Navier-Stokes equations are derived from the conservation of momentum (Newton's second law). The set of equations can be written in Eulerian terms as a single vector equation using the indicial notation [33]:

$$\rho \frac{D\boldsymbol{V}}{Dt} = \rho \boldsymbol{g} - \nabla p + \frac{\partial}{\partial x_j}\left[\mu\left(\frac{\partial v_i}{\partial x_j} + \frac{\partial v_j}{\partial x_i}\right) + \delta_{ij}\lambda \mathrm{div}\boldsymbol{V}\right] \tag{2-6}$$

where $\boldsymbol{g}$ is the gravitation vector, x_i is the spatial co-ordinate, v_i is the i-component of the velocity vector, μ is the ordinary coefficient of viscosity, λ is the coefficient of bulk viscosity, δ_{ij} is the Kronecker delta function (δ_{ij}=1 if i=j and δ_{ij}=0 of $i \neq j$) and $\frac{D}{Dt}$ the total or substantial derivative. The relation between the ordinary viscosity and bulk viscosity is given by Stokes' hypothesis [34]:

$$\lambda + \frac{2}{3}\mu = 0 \tag{2-7}$$

As an example, equation (2-6) is written out in full for the i-direction in the following equation:

$$\begin{aligned}\rho \frac{Du}{Dt} = \rho g_x - \frac{\partial p}{\partial x} + \frac{\partial}{\partial x}\left(2\mu\frac{\partial u}{\partial x} + \lambda \mathrm{div}\boldsymbol{V}\right) + \frac{\partial}{\partial y}\left[\mu\left(\frac{\partial u}{\partial y} + \frac{\partial v}{\partial x}\right)\right] \\ + \frac{\partial}{\partial z}\left[\mu\left(\frac{\partial u}{\partial z} + \frac{\partial w}{\partial x}\right)\right]\end{aligned} \tag{2-8}$$

When assuming incompressible flow with a constant viscosity, equation (2-6) reduces considerably to the following:

$$\rho \frac{D\boldsymbol{V}}{Dt} = \rho \boldsymbol{g} - \nabla p + \mu \nabla^2 \boldsymbol{V} \tag{2-9}$$

For many natural-convection flows, you can get faster convergence with the Boussinesq model (originally published in [35] as cited in [36]) than you can get by setting up the problem with fluid density as a function of temperature. This model treats density as a constant value in all solved equations, except for a momentum source term in the momentum equation:

$$(\rho - \rho_0)g \approx -\rho_0 \beta (T - T_0)g \tag{2-10}$$

where ρ_0 is the (constant) density of the fluid, T_0 is the operating temperature, and β is the thermal expansion coefficient. Equation (2-10) is obtained by using the Boussinesq approximation $\rho = \rho_0(1 - \beta \Delta T)$ to eliminate ρ from the buoyancy term. This approximation is accurate as long as changes in actual density are small; specifically, the Boussinesq approximation is valid when $\beta(T - T_0) << 1$ [37]. The term on the left of this equation $(\beta(T - T_0))$ is the fraction of the change in density relative to the reference density, implying that the change in density should be small relative to the reference density.

Transport of Energy

The energy equation is derived from the first law of thermodynamics. The energy relation in Eulerian terms is given by the following if it is assumed that the conduction heat fluxes are given by Fourier's Law and that radiative effects are negligible [33]:

$$\rho \frac{Dh}{Dt} = \frac{Dp}{Dt} + \text{div}(k \nabla T) + \Phi \tag{2-11}$$

where h is the fluid enthalpy, k is the thermal conductivity, T is the temperature of the fluid and Φ is the viscous dissipation and is given by:

$$\Phi = \mu \left[2\left(\frac{\partial u}{\partial x}\right)^2 + 2\left(\frac{\partial v}{\partial y}\right)^2 + 2\left(\frac{\partial w}{\partial z}\right)^2 + \left(\frac{\partial v}{\partial x} + \frac{\partial u}{\partial y}\right)^2 + \left(\frac{\partial w}{\partial y} + \frac{\partial v}{\partial z}\right)^2 + \left(\frac{\partial u}{\partial z} + \frac{\partial w}{\partial x}\right)^2 \right] + \lambda \left(\frac{\partial u}{\partial x} + \frac{\partial v}{\partial y} + \frac{\partial w}{\partial z}\right)^2 \tag{2-12}$$

Again assuming incompressible flow as well as a constant thermal conductivity and low-velocity flow where the viscous-dissipation (Φ) is zero, equation (2-11) reduces considerably to the following:

$$\rho c_p \frac{DT}{Dt} = k\nabla^2 T \tag{2-13}$$

2-2.4.3 Turbulence Modelling

Turbulence models are used in CFD because of the fact that the small-scale fluctuations of the flow field cannot be resolved when solving the above-mentioned governing equations on an ordinary grid. Instead, the ensemble average of the basic conservation equations is taken to give the Reynolds-Averaged Navier-Stokes (RANS) formulation. The RANS formulation is derived from the assumption that every solved for quantity consists of a mean part as given and a fluctuating part. For instance, the u_i velocity component is decomposed into a mean part and a fluctuating part as given in equation (2-14).

$$u_i(\vec{x},t) = U_i(\vec{x},t) + u_i'(\vec{x},t) \tag{2-14}$$

Figure 2-2 shows a typical behaviour for the u_i velocity component but all the flow quantities that are solved for are assumed to be of a similar form.

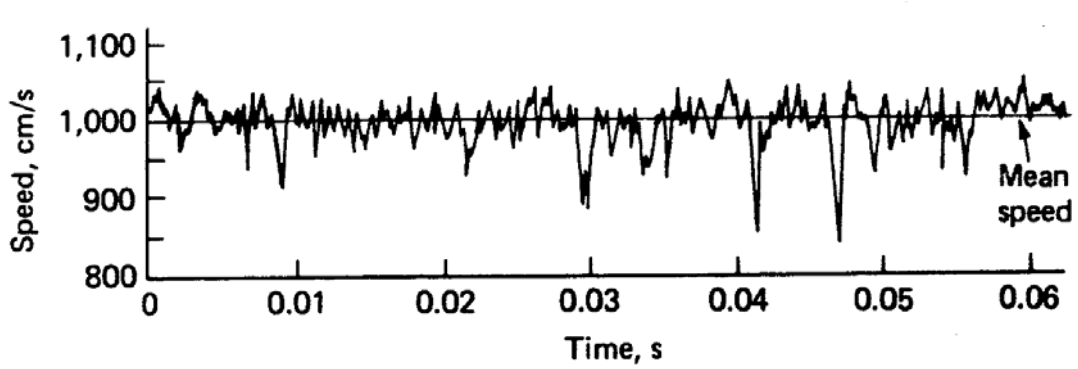

Figure 2-2: Typical time variation of the u_i-velocity component in a flow field [33]

By substituting the assumed decomposition of the solved for quantities as given in (2-14) into the Navier-Stokes and simplifying, we get the RANS equations. For example, the RANS formulation for the momentum equation for incompressible flow with constant viscosity is given in equation (2-15) [33].

$$\rho \frac{D\overline{\mathbf{V}}}{Dt} + \rho \frac{\partial}{\partial x_j}\left(\overline{u'_i u'_j}\right) = \rho \mathbf{g} - \nabla \overline{p} + \mu \nabla^2 \overline{\mathbf{V}} \qquad (2\text{-}15)$$

where u'_i are the small fluctuations in the velocity of the flow field, and $\overline{V}$ and $\overline{p}$ indicate the time-averaged velocity vector and pressure respectively.

Comparing equation (2-9) and equation (2-15) it can be seen that the momentum equation is complicated by an extra term called the turbulent inertia tensor or Reynolds stresses $\left(\overline{u'_i u'_j}\right)$. This term's analytical form is not known beforehand. This symmetrical inertia tensor introduces six new variables in 3-D, which can only be calculated through a detailed knowledge of the turbulent structure. This turbulent structure is however unknown at the start of a calculation. The effect of the small-scale fluctuations is therefore rather represented by a turbulence model than calculating the turbulent inertia tensor. The available turbulence models can be divided into the following groups.

Zero-equation models

These models are simple algebraic models and are computationally inexpensive. The accuracy obtained with these types of models is sometimes not sufficient especially in very complex flow, due to the fact that no information from the surrounding flow field is used. Some examples of these types of turbulence models are the mixing-length model and the Baldwin-Lomax model [38].

One-equation models

One-equation turbulence models model the turbulent kinetic energy (k) equation. These models satisfy the transport of the turbulent kinetic energy. The turbulent length scales in these models are correlated with algebraic equations [39]. The results obtained with these types of models are satisfactory but no better than the zero-equation models resulting in the fact that these models are not very popular. An exception is the Spallart-Almaras model that has been developed for high speed external flow applications.

Two-equation models

In two-equation turbulence models, a second equation is coupled with the turbulent kinetic energy equation used in the one-equation models. The second equation models for example the rate of change of either dissipation (ε), turbulent length scale (L) or vorticity (ω).

The most popular scheme is probably the standard k-ε model [40,41,42] or some derivative of it like the renormalisation group (RNG) k-ε model [43]. This model is also used throughout this study. The two equations that describe the turbulent kinetic energy (k) and turbulent dissipation (ε) are given in the following two equations.

$$\frac{Dk}{Dt} = \frac{\partial}{\partial x_j}\left(\frac{\nu_t}{\sigma_k}\frac{\partial k}{\partial x_j}\right) + \nu_t \frac{\partial \overline{u}_i}{\partial x_j}\left(\frac{\partial \overline{u}_i}{\partial x_j} + \frac{\partial \overline{u}_j}{\partial x_i}\right) - \varepsilon \tag{2-16}$$

$$\frac{D\varepsilon}{Dt} = \frac{\partial}{\partial x_j}\left(\frac{\nu_t}{\sigma_\varepsilon}\frac{\partial \varepsilon}{\partial x_j}\right) + C_1\nu_t \frac{\varepsilon}{k}\frac{\partial \overline{u}_i}{\partial x_j}\left(\frac{\partial \overline{u}_i}{\partial x_j} + \frac{\partial \overline{u}_j}{\partial x_i}\right) - C_2\frac{\varepsilon^2}{k} \tag{2-17}$$

where σ_k, σ_ε, C_1 and C_2 are empirical constants and ν_t is the eddy viscosity. The eddy viscosity is modelled as follows:

$$\nu_t = \frac{\mu_t}{\rho} = \frac{C_\mu k^2}{\varepsilon} \tag{2-18}$$

where C_μ is an empirical constant.

The recommended values for the empirical constants are [33]:

$$C_\mu = 0.09 \quad C_1 = 1.44 \quad C_1 = 1.92 \quad \sigma_k = 1.0 \quad \sigma_\varepsilon = 1.3 \tag{2-19}$$

These values are not universal and have to be modified for other type of flows, e.g., recirculating flows.

Wall-function approach

Equations (2-16) and (2-17) are not valid near a boundary wall because sublayer damping effects are neglected in the model. Wall functions are therefore used near the wall. The use of wall functions also avoids the need for a very fine grid near the wall. An example of wall functions as proposed by Launder and Spalding's law of the wall [40,44] is:

$$U^* = \frac{1}{\kappa}\ln\left(Ey^*\right)$$

$$\text{with} \quad U^* = \frac{U_P C_\mu^{1/4} k_P^{1/2}}{\tau_w/\rho} \tag{2-20}$$

$$\text{and} \quad y^* = \frac{\rho C_\mu^{1/4} k_p^{1/2} y_P}{\mu}$$

where κ is the Von Kármán constant (= 0.42), E an empirical constant (= 9.81), U_P the mean velocity of the fluid at point P, k_P the turbulent

kinetic energy at point P, y_P the distance from point P to the wall, and μ the dynamic viscosity of the fluid.

The effect of turbulence in all the above-mentioned models is modelled as an increase in the viscosity. This is called the eddy-viscosity concept. The dynamic viscosity (μ) used in equations (2-6) and (2-12) is the total viscosity and is expressed as the sum of the molecular viscosity of the fluid plus the turbulent viscosity (μ_t). The turbulent viscosity is directly calculated from the turbulent kinetic energy and turbulent dissipation rate. For the standard k-ε model this relationship is given in equation (2-18).

Other Methods

Another approach in turbulence modelling is to model the Reynolds stresses $\left(-\rho\overline{u_i'u_j'}\right)$ using partial differential equations [45]. These are called the Reynolds Stress Models (RSM). The RSM model is at a level higher than the previous schemes and therefore provides second-order turbulent closure at the cost of computational complexity. Another method to reduce the complexity of the RSM approach, is to model the Reynolds stresses by a purely algebraic equation with the same characteristics than the differential equations [46]. These methods are called the Algebraic Stress Models (ASM). Both these Reynolds stress models, RSM and ASM, have the potential for greater accuracy, mainly because the turbulence in the flow is not assumed to be isotropic as the previous methods (i.e., the zero-, one and two-equation models).

Currently a lot of research is conducted on Large-Eddy Simulation (LES) in which only the smallest fluctuations (or sub-grid scales) are modelled using a simple turbulence model (e.g., k-ε turbulence model). Modelling the turbulence in this way requires an unsteady simulation with a very fine grid distribution, making this model computational

very expensive. For industrial applications, like the tundish, this model is computationally too expensive.

Currently another active research topic is that of Direct Numerical Simulation (DNS). This method for calculating turbulent flow is direct in that it does not use turbulence models. Consequently, a very fine grid and small time step are required. The method is even more computationally expensive than the LES model. This method is currently considered as the state-of-the-art method for turbulent flow calculations but is restricted to very simple flow cases with a low Reynolds number making it impractical for industrial applications of CFD.

2-2.4.4 Inclusion modelling

Modelling of the non-metallic inclusion in steel melt can be done in a number of ways [47]. The different methods will now be briefly discussed.

Lagrangian particle tracking

The trajectory of a discrete phase particle (or inclusion) can be predicted by integrating the force balance on the particle, which is written in a Lagrangian reference frame. This force balance equates the particle inertia with the forces acting on the particle, and can be written (for the *x*-direction in Cartesian coordinates) as [37]:

$$\frac{du_p}{dt} = F_D\left(u - u_p\right) + \frac{g_x\left(\rho_p - \rho\right)}{\rho_p} + Fx \qquad (2\text{-}21)$$

where $F_D\left(u - u_p\right)$ is the drag force per unit particle mass and

$$F_D = \frac{18\mu}{\rho_P d_p^2}\frac{C_D \,\mathrm{Re}}{24} \qquad (2\text{-}22)$$

Here, u is the fluid phase velocity, u_p is the particle velocity, μ is the molecular viscosity of the fluid, ρ is the fluid density, ρ_p is the density

of the particle, and d_p is the particle diameter. Re is the relative Reynolds number, which is defined as

$$\mathrm{Re} = \frac{\rho d_p \left| u_p - u \right|}{\mu} \tag{2-23}$$

The drag coefficient, C_D, is taken from:

$$C_D = a_1 + \frac{a_2}{\mathrm{Re}} + \frac{a_3}{\mathrm{Re}^2} \tag{2-24}$$

where a_1, a_2, and a_3 are constants that apply for smooth spherical particles over several ranges of Reynolds number given by Morsi and Alexander [48].

The effect of a turbulent flow field in the above-mentioned method does not include the effect of turbulence on the particle trajectory. One approach to include the effect of turbulence is through stochastic tracking. This approach predicts the turbulent dispersion of particles by integrating the trajectory equations for individual particles, using the instantaneous fluid velocity, e.g., for the *x*-direction $\bar{u} + u'(t)$, along the particle path during the integration. By computing the trajectory in this manner for a sufficient number of representative particles, the random effects of turbulence on the particle dispersion may be accounted for [37]. The velocity fluctuations that prevail during the lifetime of the turbulent eddy are sampled by assuming that they obey a Gaussian probability distribution. This results in the fluctuation velocity in the *x*-direction to be:

$$u' = \zeta \sqrt{\overline{u'^2}} \tag{2-25}$$

where ζ is a normally distributed random number and $\sqrt{\overline{u'^2}}$ is the local RMS value of the velocity fluctuations. Since the kinetic energy of turbulence is known at each point in the flow (from the appropriate turbulence model), these values of the RMS fluctuating components can be obtained (assuming isotropy) as:

$$\sqrt{\overline{u'^2}} = \sqrt{\frac{2k}{3}} \tag{2-26}$$

The characteristic lifetime of the eddy is best calculated by assuming a random variation about T_L:

$$\tau_e = -T_L \log(r) \tag{2-27}$$

where r is a uniform random number between 0 and 1, T_L is given by $C_L \frac{k}{\varepsilon}$ with $C_L \approx 0.15$ when used in conjunction with the k-ε turbulence model [49].

The particle eddy crossing time is defined as

$$t_{cross} = -\tau \ln\left[1 - \left(\frac{L_e}{\tau |u - u_p|}\right)\right] \tag{2-28}$$

where τ is the particle relaxation time, L_e is the eddy length scale, and $|u - u_p|$ is the magnitude of the relative velocity.

The particle is assumed to interact with the fluid phase eddy over the smaller of the eddy lifetime and the eddy crossing time. When this time is reached, a new value of the instantaneous velocity is obtained by applying a new value of ζ in (2-25) [31].

Inclusion diffusion model

The second method makes use of a species diffusion model to calculate the distribution of small inclusions [47]. This method solves the convection-diffusion equation of a species inside the tundish as given in equation (2-29) to give the time evolution of the inclusion mass fraction, *Y*:

$$\frac{\partial}{\partial t}(\rho Y)+\frac{\partial}{\partial x_i}(\rho u_i Y)+\frac{\partial}{\partial x_i}\left(\rho D_{eff}\frac{\partial Y}{\partial x_i}\right)=0 \qquad (2\text{-}29)$$

where D_{eff} is the local effective diffusion coefficient and is dependent on the local turbulence and dissipation levels as calculated from the turbulence model as given in (2-30):

$$D_{eff}=D_0+\frac{\mu_t}{\rho \mathrm{Sc}_t} \qquad (2\text{-}30)$$

where D_0 is the laminar diffusion coefficient and Sc_t is the turbulent Schmitt number.

The flotation of inclusions, reoxidation, and collision agglomeration are ignored in this model which is only used to investigate general transient mixing behaviour.

Lumped inclusion removal model with size function

The last model calculates the evolution of the inclusion size distribution for the duration of its residence time in the tundish (developed by Miki *et al* [50]). This model considers the collision of particles due to both turbulence and differences in flotation removal rate of each inclusion size. This is a lumped model based on uniform average properties within the tundish. The collision rate due to turbulent eddy motion is governed by the mean turbulent dissipation level, ε, and the cluster size of the inclusion. Details of this model can be found in [47,50].

2-2.4.5 Solution Algorithm

The finite volume approach as implemented in the commercial CFD solver, FLUENT [37] is used in this study. In this method, the governing equations are first integrated on the individual control volumes that were created in the grid generation phase, to construct algebraic equations for the discrete dependent variables such as velocities, pressure, temperature, and conserved scalars. Secondly, the

discretised equations are linearised and the resulting linear equation system is solved to yield updated values of the dependent variables.

In this study, the segregated solution method of FLUENT is used. In this approach, the governing equations are solved sequentially (i.e., segregated from one another). Because the governing equations are non-linear (and coupled), several iterations of the solution loop must be performed before a converged solution is obtained. Each iteration consists of the steps illustrated in Figure 2-3 and outlined below [37]:

- Fluid properties are updated, based on the current solution. (If the calculation has just begun, the fluid properties will be updated based on the initialised solution.)
- The *u*, *v* and *w* momentum equations are each solved in turn using current values for pressure and face mass fluxes, in order to update the velocity field.
- Since the velocities obtained in the previous step may not satisfy the continuity equation locally, a 'Poisson-type' equation for the pressure correction is derived from the continuity equation and the linearised momentum equations. This pressure correction equation is then solved to obtain the necessary corrections to the pressure and velocity fields and face mass fluxes such that continuity is satisfied.
- Equations for scalars such as turbulence, energy and species are solved using the previously updated values of the other variables.
- A check for convergence of the equation set is made.

These steps are continued until the convergence criteria are met.

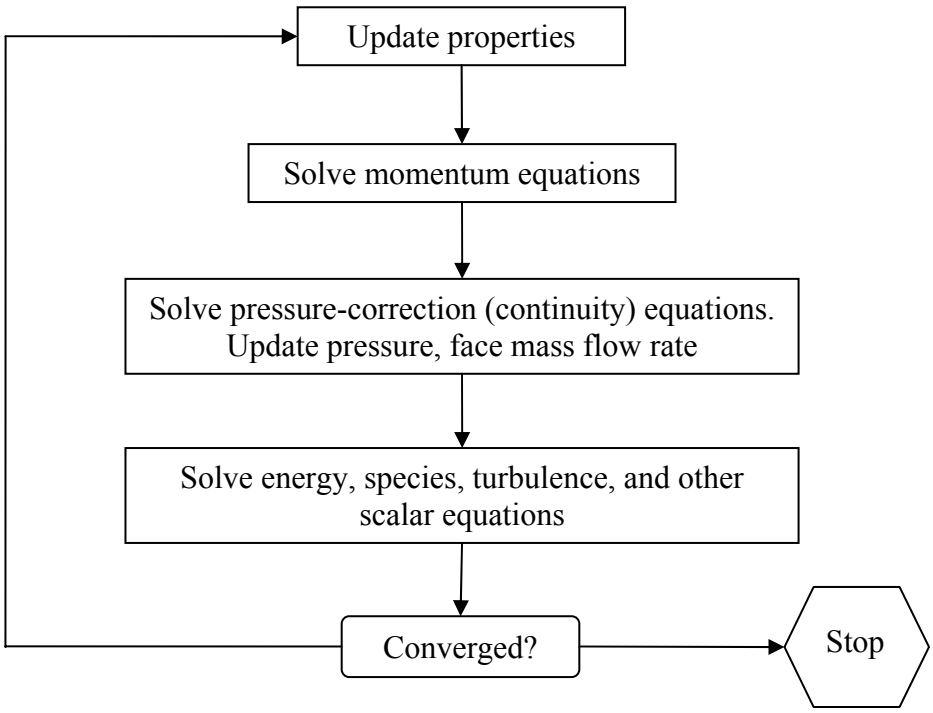

Figure 2-3: Overview of the Segregated Solution Method [37]

2-3 MATHEMATICAL OPTIMISATION

2-3.1 *Definition of Mathematical Optimisation*

Mathematical optimisation can be described as the systematic approach to find the minimum (or maximum) of a specific function given a set of constraints. In an engineering application, this relates to the case of finding the best design under certain design constraints by changing the appropriate design variables.

2-3.2 *The Non-Linear Optimisation Problem*

The non-linear constrained optimisation problem can be defined in general in the following standard way:

$$\min_{\boldsymbol{x}} f(\boldsymbol{x});\ \boldsymbol{x} = [x_1, x_2, \ldots, x_i, \ldots, x_n]^T,\ x_i \in R$$

$$\text{Subject to: } \begin{matrix} g_j(\boldsymbol{x}) \le 0; & j = 1,2,\ldots,m \\ h_k(\boldsymbol{x}) = 0; & k = 1,2,\ldots,p < n \end{matrix} \qquad (2\text{-}31)$$

where $f(\boldsymbol{x})$, $g_j(\boldsymbol{x})$ and $h_k(\boldsymbol{x})$ are scalar functions of the vector $\boldsymbol{x}$.

The function $f(\boldsymbol{x})$ is the objective function (or sometimes called the cost function) that is being minimised. The functions $g_j(\boldsymbol{x})$ and $h_k(\boldsymbol{x})$ are the inequality and equality constraints respectively. The variable n is called the dimension of the optimisation problem. The components of the vector $\boldsymbol{x}$ are called the design variables. The solution to problem (2-31) is given by the vector $\boldsymbol{x}^*$:

$$\boldsymbol{x}^* = \left[x_1^*; x_2^*; \ldots; x_n^*\right]^{\mathrm{T}} \tag{2-32}$$

and gives the lowest value for $f(\boldsymbol{x})$ subject to the specified inequality and equality constraints. The solution $\boldsymbol{x}^*$ may however be non-unique.

If there are no equality or inequality constraints, the optimisation problem becomes an unconstrained optimisation problem. The unconstrained optimisation problem can be more easily solved because the optimisation simply consists of finding the minimum of $f(\boldsymbol{x})$. For a constrained optimisation problem, the optimisation becomes much more complex and the constraints have to be treated in some sort of special way. The most popular way to treat these constraints is by introducing a penalty function, as will be described in the following paragraphs.

A large number of algorithms have been developed to solve the optimisation problem given in equation (2-31). Some of the state-of-the-art methods include multiplier methods and sequential quadratic programming [51, 52]. This chapter will only discuss the optimisation algorithms that were used in this study. The choice of these specific algorithms is guided the way in which each algorithm is suited for problems with computationally expensive function evaluations as well as the robustness of the algorithms. The success of the choices becomes evident in the rest of this study.

2-3.3 Optimisation Algorithms

Two optimisation algorithms are investigated in this study. The first is a gradient-based optimisation algorithm of Snyman called DYNAMIC-Q, while

the second is the Successive Response Surface Method (SRSM) algorithm incorporated into the commercial optimisation program LS-OPT. Both these optimisation algorithms make use internally of another optimisation algorithm, the Leap Frog Optimisation Program (LFOPC), to optimise an approximation to the original optimisation problem. DYNAMIC-Q, SRSM and LFOPC will now be discussed in detail.

2-3.3.1 Snyman's Leap-Frog Optimisation Program (LFOP) Adapted to Handle Constrained Optimisation Problems (LFOPC)

The original LFOP of Snyman [53,54] was subsequently adapted to handle constrained optimisation problems [55,56,57]. This is achieved by applying the original LFOP to a penalty function formulation of the original problem. The appropriate penalty function formulation is given in equation (2-33).

$$p(\boldsymbol{x}) = \gamma f(\boldsymbol{x}) + \sum_{j=1}^{m} \alpha_j g_j^2(\boldsymbol{x}) + \sum_{k=1}^{p} \beta_k h_k^2(\boldsymbol{x}) \qquad (2\text{-}33)$$

where $\alpha_j = \begin{cases} 0 & \text{if} \quad g_j(\boldsymbol{x}) \le 0 \\ \rho_j & \text{if} \quad g_j(\boldsymbol{x}) > 0 \end{cases}$, ρ_j and β_k are large positive numbers and $\gamma = 1$ (unless otherwise stated).

For simplicity, the penalty parameters, $\rho_j, j = 1,2,\ldots,m$ and $\beta_k, k = 1,2,\ldots,p$ take on the same positive value, $\rho_j = \beta_k = \mu$. The unconstrained minimum of $p(\boldsymbol{x})$ tends to the constrained minimum of problem (2-31) as μ tends to infinity. The choice of μ has received a lot of attention. For μ very large, high accuracy is obtained, although the unconstrained minimisation problem can become ill-conditioned. For this reason, the penalty is usually increased gradually, thereby allowing a controlled approach to the solution with limited violation of the inequality constraints in the initial design steps.

The LFOPC applies the LFOP algorithm to the penalty function formulation (as given in (2-33)) in three phases. The three phases are executed in the following way [57]:

Phase 0:

In the first phase, the penalty parameter is introduced at a moderately low value. The penalty function is then minimised using the LFOP. In this phase, the value of μ is set to $\mu_0=10^2$. This initial value of μ was used throughout this study. This is possible because the LFOP automatically scales the constraints ensuring that the spatial violation of a constraint on the penalty function gradient is approximately the same for all the constraints. On convergence, this gives an approximate optimum point. The active inequality constraints are then identified. An active inequality constraint is one that is violated. In the standard formulation (2-31), this implies that the particular inequality constraint g_j is greater than or equal to zero. If no active inequality constraints are found and there are no equality constraints, the algorithm is terminated and the minimum is found. The minimum of the constrained problem in (2-31) is then the same as the minimum of the unconstrained problem. If the computational time of the optimisation program becomes significant, the following phase is sometimes skipped if the number of active constraint plus the number of equality constraint are equal to the number of design variables. The computational time associated with CFD is however, a few orders larger than the computational time of the optimisation program and therefore the following phase has never been skipped in this study.

Phase 1:

In this phase, the penalty parameter is increased. Here a value of $\mu = 10^4$ is used. The LFOP is again used to minimise the penalty function but using the approximate design point from Phase 0 as a starting point. On convergence, a more accurate approximate solution point of the original problem given in (2-31) is found. The active set

of inequality constraints is again identified. This set might not be identical to the set identified in Phase 0.

Phase 2:

In the last phase, the LFOP is used to minimise the penalty function, again using the approximate solution of the previous phase as the starting point but with γ set to zero in the penalty function. This implies that LFOP seeks a solution to the intersection of the active constraints. The constrained minimum of the optimisation problem is at the minimum of the intersection of the active constraints. If the active constraints do not intersect, this algorithm will find the best possible solution by giving a compromised solution. The compromised solution usually violates the active constraints by a small amount. This ability to obtain a compromised solution makes LFOPC a very robust algorithm as will be shown in the optimisation cases investigated in the following chapters.

The dynamic trajectory method described above is applied to a sequence of approximate subproblems until convergence is obtained. The subproblems are constructed due to the fact that is very computationally expensive to evaluate the penalty function due to the required CFD simulations. If the subproblems are not constructed, the function value will have to be evaluated at each iteration of the LFOPC algorithm. Successive subproblems are constructed at relatively high computational cost, but these subproblems are solved economically using the LFOPC algorithm. The construction of the approximate subproblems is described below.

2-3.3.2 Snyman's DYNAMIC-Q Method

In a complex problem where the objective function is unknown and/or is computationally expensive, the successive approximation scheme developed by Snyman *et al* [55,58,59,60] is used. This approach involves the application of the above-mentioned dynamic trajectory

method for unconstrained optimisation adapted to handle constrained problems through penalty formulations as follows. The DYNAMIC method is applied to successive approximate Quadratic subproblems of the original problem, hence the name, DYNAMIC-Q. The successive subproblems are constructed by sampling at relatively high computational expense, the behaviour of the optimisation problem at successive approximate solution points in the design space. These subproblems are approximated using the quadratic approximation of a function as discussed in the following paragraph. These subproblems, which are analytically simple, are solved quickly and economically using the LFOPC discussed above.

Successive quadratic subproblems, P[l]:l=1,2,…, are formed at successive design points $\boldsymbol{x}^{(l)}$. Spherically quadratic approximations are used to approximate the objective function and/or constraints, if these functions are not analytically known or computationally expensive. The approximation of the subproblems will be discussed in detail in the following paragraph.

These spherical quadratic subproblems have favourable characteristics for the optimisation program, e.g., the quadratic subproblem is smooth with no discontinuities and the subproblem usually has only one global optimum.

The application of the DYNAMIC-Q method requires the use of move limits. This is an added feature used to control convergence of the optimisation process. Essentially, it implies the placing of additional constraints that limit the movement of each of the design variables from one design point to the next design point. This is helpful in the initial steps of the optimisation run when the spherical quadratic approximation may have a large error. This implies that the next design point is not allowed to move too far from the current design point.

The move limits are implemented as additional inequality constraints in the following way:

$$\begin{aligned} x_i - x_i^{(l)} - \delta_i &\le 0 \\ -x_i + x_i^{(l)} - \delta_i &\le 0 \end{aligned}; \quad i = 1,2,\ldots,n \tag{2-34}$$

where in general the δ_i are different move limits for each design variable and $x_i^{(l)}$ is the design variable at the current design point.

The DYNAMIC-Q method has the potential to be applied to any engineering optimisation problem in which the numerical simulation is computationally expensive. The only two requirements are that the engineer has confidence in the answer obtained by the numerical analysis and that the engineer can define his/her problem as an optimisation problem. This study will apply the DYNAMIC-Q algorithm to CFD.

Constructing the Successive Approximate Spherical Quadratic Subproblems

The spherical quadratic approximation of a function is used in this study to approximate the functions that are not analytically known and/or computationally expensive to evaluate, to construct the subproblem at design iteration *l*. These functions may be the objective function or one of the constraints, depending on the optimisation problem investigated. By approximating these computationally expensive functions, the computational time is drastically reduced because only a few function evaluations are necessary to obtain the approximation. The way these successive subproblems are constructed will now be discussed in detail [55,58].

The Taylor expansion of a function $f(\boldsymbol{x})$ in the region of the current design point $\boldsymbol{x}^{(l)}$ is given by:

$$f(\boldsymbol{x}) = f(\boldsymbol{x}^{(l)}) + \nabla^{\mathrm{T}} f(\boldsymbol{x}^{(l)})(\boldsymbol{x} - \boldsymbol{x}^{(l)}) + \frac{1}{2}(\boldsymbol{x} - \boldsymbol{x}^{(l)})^{\mathrm{T}} \mathrm{H}(\boldsymbol{x}^{(l)})(\boldsymbol{x} - \boldsymbol{x}^{(l)}) + \mathrm{H.O.T} \tag{2-35}$$

where $\mathrm{H}(\boldsymbol{x}^{(l)})$ is the Hessian matrix at point $\boldsymbol{x}^{(l)}$ and H.O.T are the higher order terms in the expansion. The vector $\boldsymbol{x}^{(l)}$ is the current design point. The Hessian matrix is defined in equation (2-36).

$$\mathrm{H}(\boldsymbol{x}) = \begin{bmatrix} \frac{\partial^2 f}{\partial x_1^2} & \frac{\partial^2 f}{\partial x_1 \partial x_2} & \cdots & \frac{\partial^2 f}{\partial x_1 \partial x_n} \\ \frac{\partial^2 f}{\partial x_2 \partial x_1} & \frac{\partial^2 f}{\partial x_2^2} & \cdots & \frac{\partial^2 f}{\partial x_2 \partial x_n} \\ \vdots & \vdots & & \\ \frac{\partial^2 f}{\partial x_n \partial x_1} & \frac{\partial^2 f}{\partial x_n \partial x_2} & \cdots & \frac{\partial^2 f}{\partial x_n^2} \end{bmatrix}(\boldsymbol{x}) = \nabla^2 f(\boldsymbol{x}) \tag{2-36}$$

Note the symmetry of this matrix because $\frac{\partial^2 f}{\partial x_i \partial x_j} = \frac{\partial^2 f}{\partial x_j \partial x_i}$.

If the higher order terms are ignored, the value of f at a point $\boldsymbol{x}$ in the region of $\boldsymbol{x}^{(l)}$ is given approximately by:

$$f(\boldsymbol{x}) \approx f\left(\boldsymbol{x}^{(l)}\right) + \nabla^{\mathrm{T}} f\left(\boldsymbol{x}^{(l)}\right)\left(\boldsymbol{x} - \boldsymbol{x}^{(l)}\right) + \frac{1}{2}\left(\boldsymbol{x} - \boldsymbol{x}^{(l)}\right)^{\mathrm{T}} \mathrm{H}(\boldsymbol{x}^{(l)})\left(\boldsymbol{x} - \boldsymbol{x}^{(l)}\right) \tag{2-37}$$

The gradient vector $\nabla f\left(\boldsymbol{x}^{(l)}\right)$ in equation (2-37), is approximated using a first-order forward differencing scheme. This first-order gradient approximation needs some special consideration and will be discussed in the following paragraphs.

Because the function f, or its derivatives, is not analytically known, the second-order derivatives need also to be calculated using a finite-difference approximation, e.g., a forward-differencing scheme. Furthermore, if the calculation of the function is computationally expensive to evaluate (as is the case with CFD), the calculation of the Hessian matrix becomes extremely expensive computationally. The Hessian matrix is therefore approximated. The way the Hessian matrix is approximated now follows.

Taking $\mathbf{A}^{(l)}$ as the approximation of the Hessian matrix, the approximation $\tilde{f}(\boldsymbol{x})$ to the function, $f(\boldsymbol{x})$ is given by:

$$\tilde{f}(\boldsymbol{x}) = f\left(\boldsymbol{x}^{(l)}\right) + \nabla^{\mathrm{T}} f\left(\boldsymbol{x}^{(l)}\right)\left(\boldsymbol{x} - \boldsymbol{x}^{(l)}\right) + \frac{1}{2}\left(\boldsymbol{x} - \boldsymbol{x}^{(l)}\right)^{\mathrm{T}} \boldsymbol{A}^{(k)}\left(\boldsymbol{x} - \boldsymbol{x}^{(l)}\right) \tag{2-38}$$

where the approximation of the Hessian matrix ($\boldsymbol{A}^{(l)}$) is given by

$$\boldsymbol{A}^{(l)} = \mathrm{diag}\left(a^{(l)}, a^{(l)}, \ldots, a^{(l)}\right) = a^{(l)}\boldsymbol{I} \tag{2-39}$$

and $\boldsymbol{I}$ is the identity matrix.

The appropriate constant $a^{(l)}$ used in the construction of the approximate Hessian matrix is calculated by using function and gradient information at the design point $\boldsymbol{x}^{(l)}$ and at a previous design point, say at point $\boldsymbol{x}^{(l\text{-}1)}$. The value of $a^{(l)}$ defines the amount of curvature of the spherical quadratic approximation. During an optimisation run the point $\boldsymbol{x}^{(l\text{-}1)}$ is the previous design point where the gradient and function values of the function are already known. The initial value, $a^{(1)}$, depends on the specific optimisation problem being considered. In this study, a value of zero was chosen for the construction of the first subproblem. This implies that the first approximation has no curvature.

If it is specified that $\tilde{f}(\boldsymbol{x})$ interpolates $f(\boldsymbol{x})$ at $\boldsymbol{x}^{(l)}$ and $\boldsymbol{x}^{(l\text{-}1)}$ and that the gradient of $\tilde{f}(\boldsymbol{x})$ matches that of $f(\boldsymbol{x})$ at $\boldsymbol{x}^{(l)}$, equation (2-38) can be rewritten to give $a^{(l)}$ as follows:

$$a^{(l)} = \frac{2\left\{f\left(\boldsymbol{x}^{(l\text{-}1)}\right) - f\left(\boldsymbol{x}^{(l)}\right) - \nabla^{\mathrm{T}} f\left(\boldsymbol{x}^{(l)}\right)\left(\boldsymbol{x}^{(l\text{-}1)} - \boldsymbol{x}^{(l)}\right)\right\}}{\left\|\boldsymbol{x}^{(l)} - \boldsymbol{x}^{(l\text{-}1)}\right\|^2} \tag{2-40}$$

This may be called the backward interpolating spherical approximation to $f(\boldsymbol{x})$ at $\boldsymbol{x}^{(l)}$.

Another way to calculate $a^{(l)}$ is to specify that $\tilde{f}(\boldsymbol{x})$ interpolates $f(\boldsymbol{x})$ at $\boldsymbol{x}^{(l)}$ and $\boldsymbol{x}^{(l-1)}$ and that the gradient of $\tilde{f}(\boldsymbol{x})$ matches that of $f(\boldsymbol{x})$ at $\boldsymbol{x}^{(l-1)}$ and not at $\boldsymbol{x}^{(l)}$ as above. This may be called the forward interpolating spherical approximation. This gives an expression for $a^{(l)}$ as follows:

$$a^{(l)} = \frac{2\left\{f\left(\boldsymbol{x}^{(l)}\right) - f\left(\boldsymbol{x}^{(l-1)}\right) - \nabla^{\mathrm{T}} f\left(\boldsymbol{x}^{(l-1)}\right)\left(\boldsymbol{x}^{(l)} - \boldsymbol{x}^{(l-1)}\right)\right\}}{\left\|\boldsymbol{x}^{(l)} - \boldsymbol{x}^{(l-1)}\right\|^2} \tag{2-41}$$

By averaging the curvature of the backward interpolating quadratic function as in (2-40), and forward interpolating quadratic approximation as in (2-41), an averaged expression for $a^{(l)}$ can be obtained [61] and is given in (2-42).

$$a^{(l)} = \frac{\left(\nabla^{\mathrm{T}} f\left(\boldsymbol{x}^{(l-1)}\right) - \nabla^{\mathrm{T}} f\left(\boldsymbol{x}^{(l)}\right)\right)\left(\boldsymbol{x}^{(l-1)} - \boldsymbol{x}^{(l)}\right)}{\left\|\boldsymbol{x}^{(l)} - \boldsymbol{x}^{(l-1)}\right\|^2} \tag{2-42}$$

Expression (2-42) may be called the backward-forward interpolating spherical approximation and gives more stable values for the curvature. In the following chapters, it will be shown that this results in smoother convergence of the optimisation run. It must be noted that constructing $\tilde{f}(\boldsymbol{x})$ using the averaged value of $a^{(l)}$ means that it no longer necessarily interpolates $f(\boldsymbol{x})$ at point $\boldsymbol{x}^{(l-1)}$.

The DYNAMIC-Q method is terminated when either the normalized step size

$$\Delta x_{\mathrm{norm}} = \frac{\left\|\boldsymbol{x}^{(l)} - \boldsymbol{x}^{(l-1)}\right\|}{1 + \left\|\boldsymbol{x}^{(l)}\right\|} \tag{2-43}$$

or if the normalized change in function value

$$\Delta f_{\mathrm{norm}} = \frac{\left|f^{(l)} - f_{\mathrm{best}}\right|}{1 + \left|f_{\mathrm{best}}\right|} \tag{2-44}$$

are below specified tolerances. The DYNAMIC-Q method does not guarantee a global minimum and typically, a multi-start approach (i.e. starting the optimizer from different starting designs) should be used to ensure that a global optimum is obtained.

2-3.3.3 Successive Response Surface Method (SRSM)

The last optimisation method used is the Successive Response Surface Method (SRSM) [62] as implemented in LS-OPT [63]. LS-OPT is a commercial package available as part of the LS-DYNA software suite. This algorithm uses a Response Surface Methodology (RSM) [64], i.e., a meta-modelling or surrogate technique, to construct linear response surfaces on a subregion from a *D*-optimal subset of experiments. The *D*-optimality criterion is implemented using a genetic algorithm and a 50% over-sampling is typically used. Successive subproblems are solved using a multi-start variant of the Leap-Frog dynamic trajectory method of Snyman [57]. The multi-start locations are selected as the subset of experimental designs, and the best optimum is selected as the optimum of the subproblem. The size of successive subregions is adapted based on contraction and panning parameters designed to prevent oscillation and premature termination [62]. Infeasibility is handled automatically when it occurs through the construction and solution of an auxiliary problem to bring the design within the subregion if possible. As the optimum is approached, the subregion is contracted automatically, implying that inaccuracies in the sensitivity information do not cause large departures from the previous design. Therefore, this handling of the step-size dilemma also provides an inherent move limit to the algorithm.

2-3.4 Gradient Approximation of Objective and Constraint Functions

The Dynamic-Q method of Snyman needs first-order gradients of the objective and constraint functions with respect to each of the design variables. There are different methods available when calculating these gradients. These different methods have certain advantages and disadvantages when using CFD to construct the gradient, as explained in the next section.

Forward-Differencing Scheme

A forward-differencing scheme is used to approximate the gradient vector of the objective function $\left(\nabla f\left(\boldsymbol{x}^{(l)}\right)\right)$ when the function is approximated using the spherical quadratic approximation discussed in 2-3.3.2. The first-order gradients are calculated as follows:

$$\frac{\partial f(\boldsymbol{x})}{\partial x_i} = \frac{f(\boldsymbol{x}+\Delta\boldsymbol{x_i}) - f(\boldsymbol{x})}{\Delta x_i} \quad i = 1,2,\ldots,n \tag{2-45}$$

where

$$\Delta\boldsymbol{x}_i = [0,0,\ldots,\Delta x_i,\ldots,0]^T$$

The first-order gradients of the inequality and equality constraints, when these constraints are approximated using the spherical quadratic approximation, are approximated in a similar fashion and are given in (2-46).

$$\begin{aligned} \frac{\partial g_j(\boldsymbol{x})}{\partial x_i} &= \frac{g_j(\boldsymbol{x}+\Delta\boldsymbol{x_i}) - g_j(\boldsymbol{x})}{\Delta x_i} \qquad j = 1,\ldots m \\ \frac{\partial h_k(\boldsymbol{x})}{\partial x_i} &= \frac{h_k(\boldsymbol{x}+\Delta\boldsymbol{x_i}) - h_k(\boldsymbol{x})}{\Delta x_i} \qquad k = 1,\ldots p \end{aligned} \tag{2-46}$$

again with

$$\Delta\boldsymbol{x}_i = [0,0,\ldots,\Delta x_i,\ldots,0]^T$$

A new CFD simulation is required to approximate each of the gradients. A number of $n+1$ CFD simulations have therefore to be performed at each optimisation iteration. The restart feature of the CFD package can be used to reduce the computation time required to obtain the CFD solution. In some cases, the amount of iterations to obtain a converged CFD solution can be reduced by a factor of ten when using the restart feature of the CFD package.

2-3.5 Effect of Noise Associated with CFD Solutions on the Gradient Approximation

2-3.5.1 Source of Noise in CFD Solutions

In a steady-state CFD solution, the simulation is terminated when the residuals fall below a specified value. The numerical solution is therefore not an exact solution. Furthermore, there may be some round-off error due to the precision of the computer. If too small a Δx is chosen, the function value of the base case and that of the perturbation falls within the accuracy of the numerical analysis and the forward first-order differencing becomes void.

2-3.5.2 Influence of Noise on the Finite Differencing Scheme

Some difficulties may be encountered when approximating the derivatives using a finite differencing scheme on a noisy function. Figure 2-4 shows the effect on the first-order derivative when approximating the derivative using a forward-differencing scheme on a noisy function in one dimension. Figure 2-4(a) shows the approximated gradient for a small Δx. Due to the noise on the function, the gradient with a small Δx gives a totally different value than the one with a large Δx as shown in the right-hand graph of Figure 2-4(b). The gradient in the first graph is more accurate than the gradient in the second graph at point $x^{(l)}$, but when the subproblem is constructed using the gradient of the first graph, the optimisation will clearly end up with a wrong answer. The wavelength of the noise is closely linked to the correct choice of Δx. It is therefore desirable to choose a larger Δx so that the noise does not influence the global gradient of the function. Although the smaller Δx gives a more accurate gradient of the function, a larger Δx will give a more representative gradient when looking globally at the function.

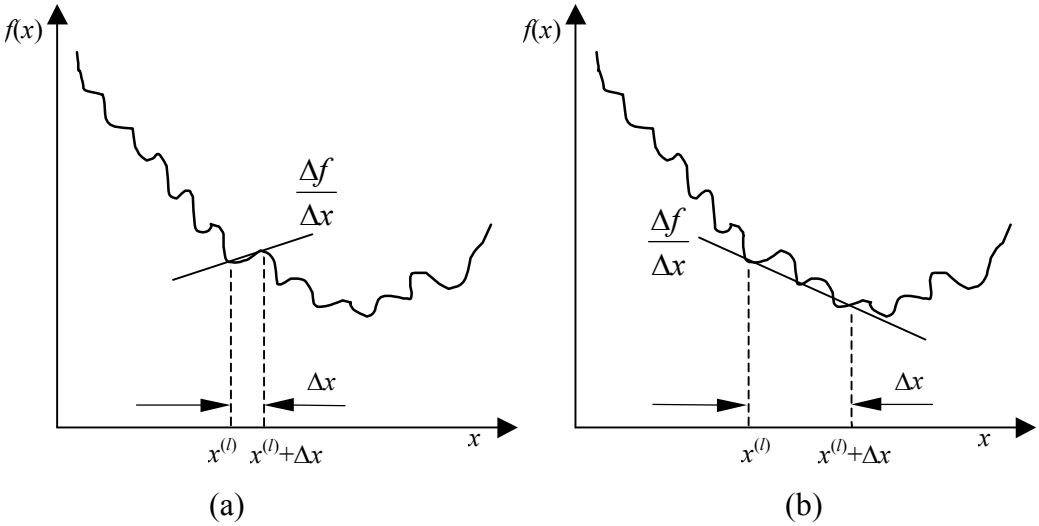

Figure 2-4: Influence of a too small step size on the finite difference approximation of the gradients of a "noisy" function in 1-D

Care must however be taken not to choose a too large Δx. This concept is illustrated in Figure 2-5 in 1-D. Choosing a too large Δx will result in an inaccurate gradient approximation as shown in Figure 2-5(b) compared to the true gradient as shown in Figure 2-5(a). The noise on the objective function, although present, is not shown in this figure.

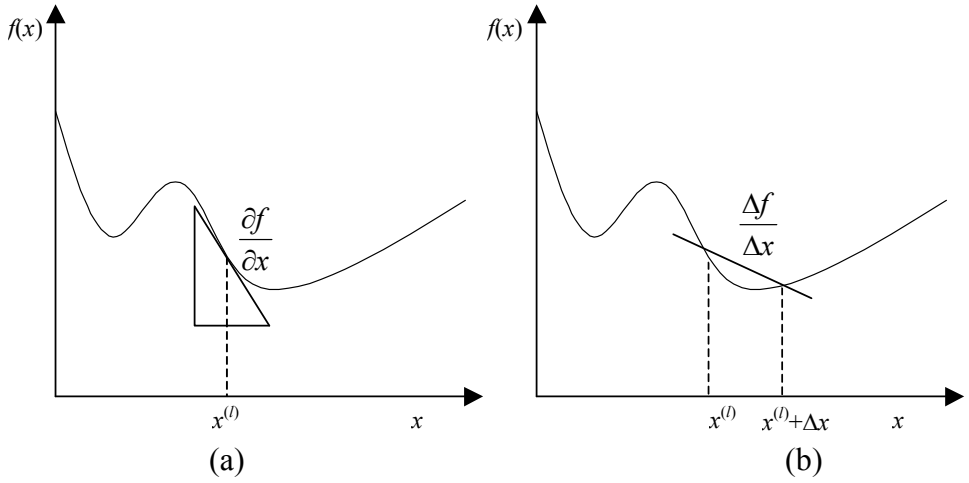

Figure 2-5: Influence of too large step size on the finite difference approximation of the gradients of a function in 1-D

A large Δx may also cause the optimisation problem not to converge and cause the design variables to rock back-and-forth near the optimum. This is illustrated graphically in one dimension in Figure 2-6. The two graphs ((a) and (b)) shown in this figure depict two consecutive design points. Figure 2-6(a), the optimiser starts at point $x^{(l)}$ and calculates a positive gradient of the function objective function, f, due to the forward-differencing scheme. The optimiser will then predict a smaller value for x. The new value $x^{(l+1)}$ as prescribed by the optimiser will however result in a larger function value. As shown in Figure 2-6(b), the optimiser now calculates a negative gradient at point $x^{(l+1)}$, that will predict a larger value for x. The optimiser now moves to point $x^{(l+2)}$, which is just to the right of the original point $x^{(l)}$. This 'rocking' or cyclic motion may continue indefinitely until the optimiser is stopped.

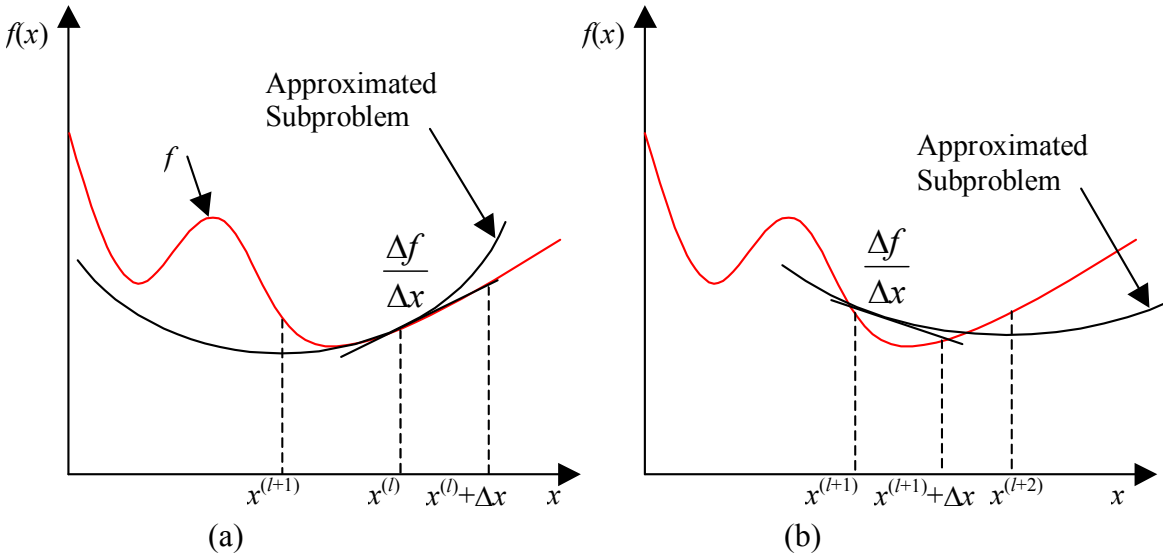

Figure 2-6: Rocking motion of one design variable near the optimum caused by the forward differencing scheme

The right choice of Δx for each of the design variables will come from a sensitivity analysis. The sensitivity analysis is computationally very expensive and usually a good engineering estimate of an appropriate perturbation size will suffice. A general rule of thumb of is to use a perturbation size of about 1/10 of the range of the design variable

There may be a variety of sources that cause the noise in the CFD solutions. This noise may be due to grid changes, convergence, numerical accuracy of the computer etc. This noise and the source of the noise still need some further investigation and falls outside the scope of this study. The better resolved the CFD analysis are, i.e., the finer the mesh, the higher the convergence of the residuals, and the more accurate the models used, the less contribution of noise is expected to be.

2-4 CONCLUSION

The first part of this chapter described the current available literature on tundish and tundish furniture design. A large amount of research has been done on improving the design of tundish and tundish furniture. These improvements are achieved by using two different types of modelling techniques. The modelling is either through physical modelling or through numerical modelling. In the physical modelling, either plant trials or water models are used. Numerical modelling makes use of Computational Fluid Dynamics (CFD). The chapter looked in detail at the techniques, methods and procedures used in CFD to model different aspects of the tundish like turbulence, heat transfer and inclusion removal. All the cases in the literature in which new tundish or tundish furniture have been designed used a trial-and-error method to improve the design using either of the modelling techniques mentioned above.

The second part of the chapter focussed on mathematical optimisation. Mathematical optimisation was formally defined and then three optimisation algorithms were discussed. The effect of numerical noise inherent to a CFD analysis and its effect on gradient-based optimisation algorithms were also shown.

3

CHAPTER 3: TUNDISH DESIGN OPTIMISATION METHODOLOGY

3-1 INTRODUCTION

This chapter describes the methodology developed to optimise tundish and tundish furniture designs. This chapter's aim is also to serve as a guide for the setup of an optimisation problem involving tundishes.

In order to optimise, one must first be confident that the modelling techniques used accurately predict the physical process being modelled. The first section of this chapter describes the validation of the modelling techniques that are going to be used to predict the physical process.

The next step is to formulate the optimisation problem. This is the most important step in the optimisation process. For the complex flow phenomena that exist inside a tundish, a wide range of candidate objective functions and constraints are available for possible use. It is up to the design engineer to decide which criteria and constraints are important and/or essential for his/her specific application.

The last section of the chapter describes the automisation of the optimisation procedure. This forms an essential part of the optimisation process. It is necessary for the optimisation procedure to be executed without any human intervention. This involves the automated setup of the problem being solved, solving the problem and then post-processing the results needed by the optimiser.

3-2 VALIDATION OF CFD MODEL

A crucial prerequisite before an optimisation run can be started is to have confidence in the accuracy of the modelling tool used in the evaluation of the objective and constraint functions. The optimisation results can only be as good as the accuracy of the modelling. For this reason, two validation cases were undertaken to validate the CFD models. These two validation cases are described below.

3-2.1 Validation Case 1

The first validation study undertaken was the validation against a full-scale single-strand water model of the Columbus Stainless Steel Caster. The details of this validation are given in Appendix A [65,66]. In this study a tracer was injected into the tundish at the shroud (refer Figure 1-1) and the concentration was measured at the outlet with a spectrophotometer [67]. The resulting Residence Time Distribution (RTD) curve was then compared with the numerical model as shown in Figure 3-1 (a repeat of Figure A-3, for ease of reference).

From the RTD curve, the relevant RTD data were extracted to compare with the experimental and CFD data. These data are given in Table 3-1 (repeated from Table A-1). Generally, good agreement is found between the experimental and CFD data with the minimum residence time (MRT) being the only value that is not predicted to within 15%. This MRT is however very sensitive to the duration of the injection and the sensitivity of the spectrophotometer (refer Appendix A).

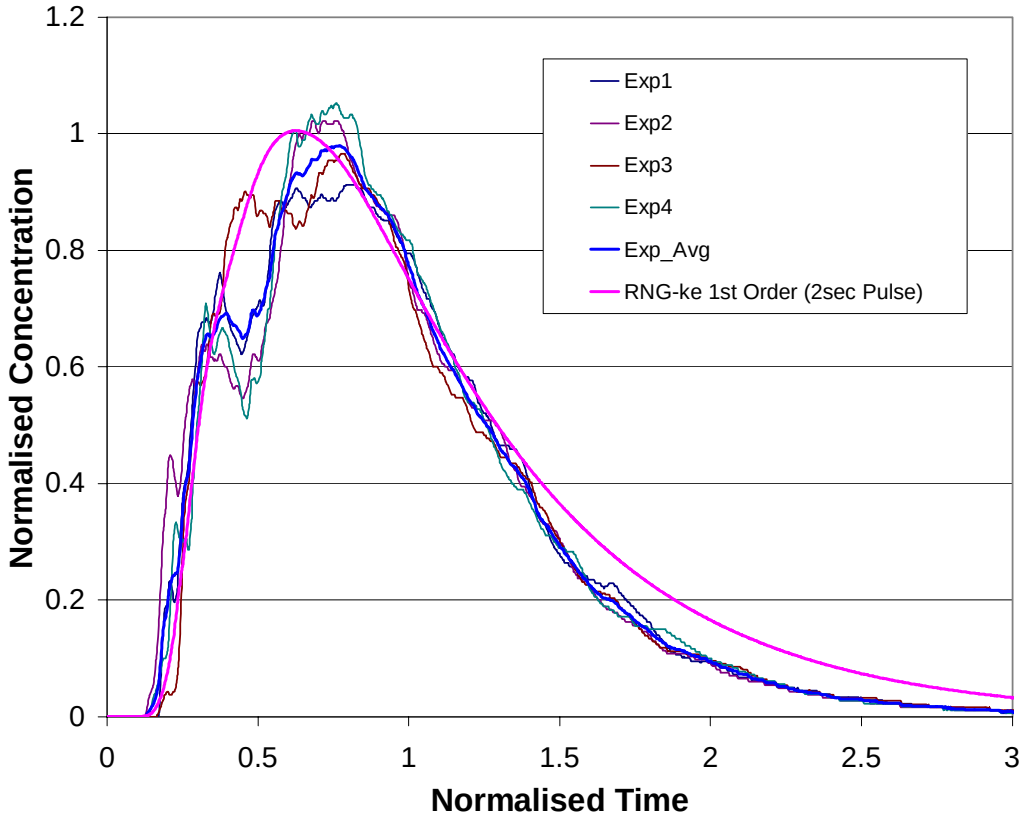

Figure 3-1: Comparison of RTD curves of the water model and CFD model

Table 3-1: Comparison of RTD data of the water model and CFD model

	Water model	CFD	% Difference
MRT	0.128	0.154	20.3%
Dispersed Plug Flow (V_{dpv})	0.450	0.391	13.1%
Mixed Flow (V_{mv})	0.406	0.452	11.3%
Dead Volume (V_{dv})	0.144	0.156	8.3%

3-2.2 Validation Case 2

The second validation was against a copper trace in a plant trial. The details of this validation study are given Appendix B [68]. This trial involved the introduction of copper adjacent to the shroud of the tundish and then

periodically taking samples from the mould. The copper concentration in the samples is then measured using a photospectrometer. This gives a RTD curve for the tundish that can be compared to that of the numerical model as given in Figure 3-2 (repeated from Figure B-2) and Table 3-2 (repeated from Table B-1). It can be seen from this figure and table that the plant trial and CFD are in good agreement. The dead flow volume is the only value that differs significantly with the plant trial results. The comparison is however acceptable, taking into account all the uncertainties associated with the plant trial.

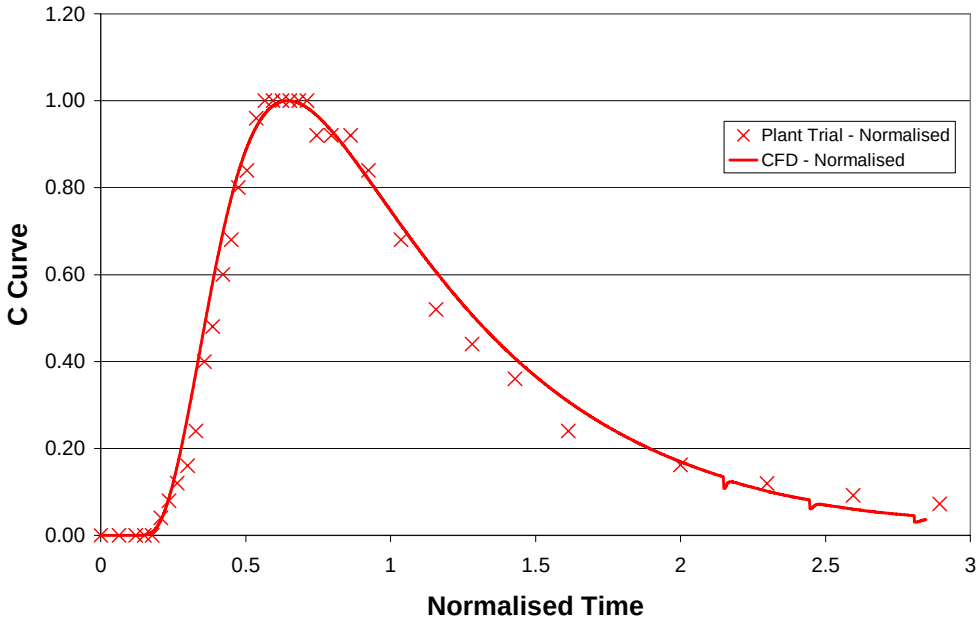

Figure 3-2: Comparison of RTD curves of the plant trial and CFD model

Table 3-2: Comparison of RTD data of the plant trial and CFD model

	Plant Trial	CFD	% Error
Plug flow volume [%]	20.7	18.2	11.9
Mixed flow volume [%]	74.5	75.7	1.6
Dead flow volume [%]	4.8	6.1	27.1

3-3 FORMULATION OF OPTIMISATION PROBLEM

The correct formulation of the optimisation problem is the most important step in any optimisation study. This section shows the different design variables, objective functions and constraints that can be chosen by the design engineer when optimising a tundish and tundish furniture.

3-3.1 Candidate design variables

The design variables are usually the easiest for the design engineer to choose. The variables are usually the design parameters that the engineer can and want to change to improve the design. Design variables for a tundish can be divided into two main categories, i.e., process variables and geometric variables.

The process variables include parameters like flow rate, inlet temperature, etc. Process variables are usually not as easy to change as these are dictated by the operation of the plant. For example, the molten steel inlet temperature is usually a function of the holding time of the ladle and the amount of time the ladle spent at the secondary metallurgy station.

Geometric variables include parameters like the position and height of a dam, or the shape and size of an impact pad or even the total size and shape of a tundish. The geometric variables, especially those linked to refractory components, are parameters that are easier to change and control than the process parameters.

3-3.2 Candidate Objective Functions and Constraints from CFD analysis

A number of candidate objective functions are available when optimising the tundish and tundish furniture design. A list of possible functions and their effect on the performance of the tundish are given below.

3-3.2.1 RTD Curve

As shown in section 2-2.2, various quantities can be extracted from a RTD curve to determine the performance of the tundish. The different quantities and their possible use in an optimisation formulation are given below.

Minimum Residence Time (MRT)

The MRT or minimum break-through time, one typically wants as long a possible. A long MRT indicates a large plug flow volume and therefore smaller mixed volume and dead volume compared to a tundish with a short MRT. This in turn will result in a short mixed-grade length in the slab when casting different grades due to the lower mixed and dead volumes. Therefore, for the design of a tundish that will undergo many grade changes, the design engineer would want to maximise MRT.

Well-mixed volume

The well-mixed volume gives an indication to how much mixing takes place within the tundish. For inclusion particle removal, it is desirable to have a large amount of mixing as this give the particle the opportunity to reach the slag surface. Conversely, for a short mixed-grade length in the slab it is desirable to have a small amount of mixing. Therefore, for the design of a tundish where the quality is of high importance, the design engineer will want to maximise the well-mixed volume.

Dead volume

The dead volume gives an indication of stagnant or recirculating regions. These regions want to be kept as small as possible as this will negatively influence the length of the mixed-grade slab. The optimisation formulation would therefore be to minimise the dead volume.

Usually a trade-off has to be made between the MRT, well-mixed volume and dead volume. A tundish with very little mixing (i.e., a high MRT, low dead volume) gives a short mixed-grade length but low inclusion removal capabilities. On the contrary, a tundish with high mixing (i.e., a high well-mixed volume) will give good inclusion removal capabilities but a long mixed-grade length. It is the design engineer's responsibility to decide which is the most important in his/her specific application and choose the appropriate RTD related quantity.

3-3.2.2 Inclusion removal

For higher quality steel and less defects, the design engineer will opt to maximise the inclusion removal on the slag layer. The inclusion removal modelling can be performed using the methods discussed in section 2-2.4.4. In some cases only the larger sized inclusions' (typically larger than 50micron) removal can be chosen to be maximised as the smaller inclusion (typically smaller than 50micron) will not adversely affect the quality of the steel. The inclusions are removed by sticking to the refractories and absorption into and reaction with the slag layer.

3-3.2.3 Mixed-grade length

The mixed-grade length can be modelled explicitly by doing a transient multi-phase CFD analysis to capture the free surface between the air, slag layer and steel. This must be done to capture the effect of wave formation on the free surface and mixing of the inlet stream with the remaining steel as the tundish is filled with a different steel grade from a new ladle. As the multi-phase analysis is a computationally expensive, an indication of the mixed grade length can however be obtained from a RTD curve (discussed in section 3-3.2.1 above) obtained for a full level or using quasi-steady solutions at various fixed fill levels. This will not be as accurate as doing a multi-phase analysis.

The mixed-grade length will obviously be minimised to reduce the amount of steel that will be downgraded.

3-3.2.4 Temperature

The minimum temperature in the tundish is required to stay above a specified lower value. This is required so that the steel does not solidify inside the tundish. Furthermore, the tundish outlet temperature is required to be within a specified temperature range to carry a certain amount of super heat into the mould. These temperatures will typically be constraint functions that will be specified in the optimisation formulation.

3-3.2.5 Slag layer

It is required that the slag layer is stagnant and that turbulence levels on the slag layer are low. High velocities and turbulence levels on the slag layer might cause slag entrainment into the steel and adversely affect the quality of the steel. Another two possible objective functions would therefore be to minimise the turbulence levels on the slag layer or to minimise the velocities on the slag layer.

3-3.2.6 Cascading

Cascading happens during the first cast when the steel enters the tundish for the first time. During this time, there is no slag cover present and at these high temperatures, significant oxidation occurs. This oxidation results in a poor quality first slab. A possible optimisation formulation would therefore be to minimise the area of steel exposed to the atmosphere. This requires a transient multi-phase flow analysis of the filling that is computationally very expensive and probably not a viable formulation due to the excessive computational effort that will be required.

3-3.3 Other Constraints

Other constraint functions also exist that are not related to the CFD simulation. These constraints are typical geometric constraints as well as manufacturing constraints. A typical manufacturing constraint would be the minimum thickness that a piece of tundish furniture could be. A geometrical constraint can also be derived from the required strength of the specific furniture piece, e.g., what is the minimum thickness that will withstand the ferrostatic head.

Another type of constraint that can be important is the yield that can be achieved by the tundish (i.e., minimising the liquid steel that remains in the tundish when drained). This can be based on a purely geometrical consideration or it can be based on the fact that a vortex forms at the end of a cast when the tundish level drops. The vortex then entrains slag that goes directly into the mould.

3-4 AUTOMATION OF OPTIMISATION PROBLEM

The automation of the optimisation problem forms an important part of the whole optimisation procedure. The automation is done so that no human intervention is required once the optimisation process has started. The optimisation process is shown in the flow diagram given in Figure 3-3. For a given starting design ($\boldsymbol{x}$), the mathematical optimiser generates a set of k designs that need to be evaluated. The number k and the exact values of the design vector to be evaluated ($\boldsymbol{x}_i$) are a function of the specific optimiser to be used. A journal file for the specific design is then generated and is passed to GAMBIT (*gambit.jou*) to generate the geometry and the mesh to be used in FLUENT. The mesh is exported to FLUENT where another journal file (*fluent.jou*) controls the setting up, running and writing of the necessary files for the post-processing of the design. As an example in this flow diagram, a file called *conc.out* is written to the hard disk containing the outlet concentration. The output file(s) are then processed to yield the objective and constraint functions of the specific design. The mathematical optimiser gathers all these data and predicts a new optimum design. The process is repeated until the optimisation converges to specified criteria.

To reduce the time required by the optimiser to reach convergence, either the FLUENT simulation can be run in parallel on a multi-CPU machine or a cluster of machines on a Local Area Network; or each design to be evaluated ($\boldsymbol{x}_i$) can be run on a different computer. Both these methods will reduce the wall-clock time for one optimisation iteration.

The flow diagram in Figure 3-3 is applicable to both optimisers used in this thesis. The Dynamic-Q program of Snyman was adapted to be integrated into FLUENT and GAMBIT. The modified Fortran program is given in Appendix C.

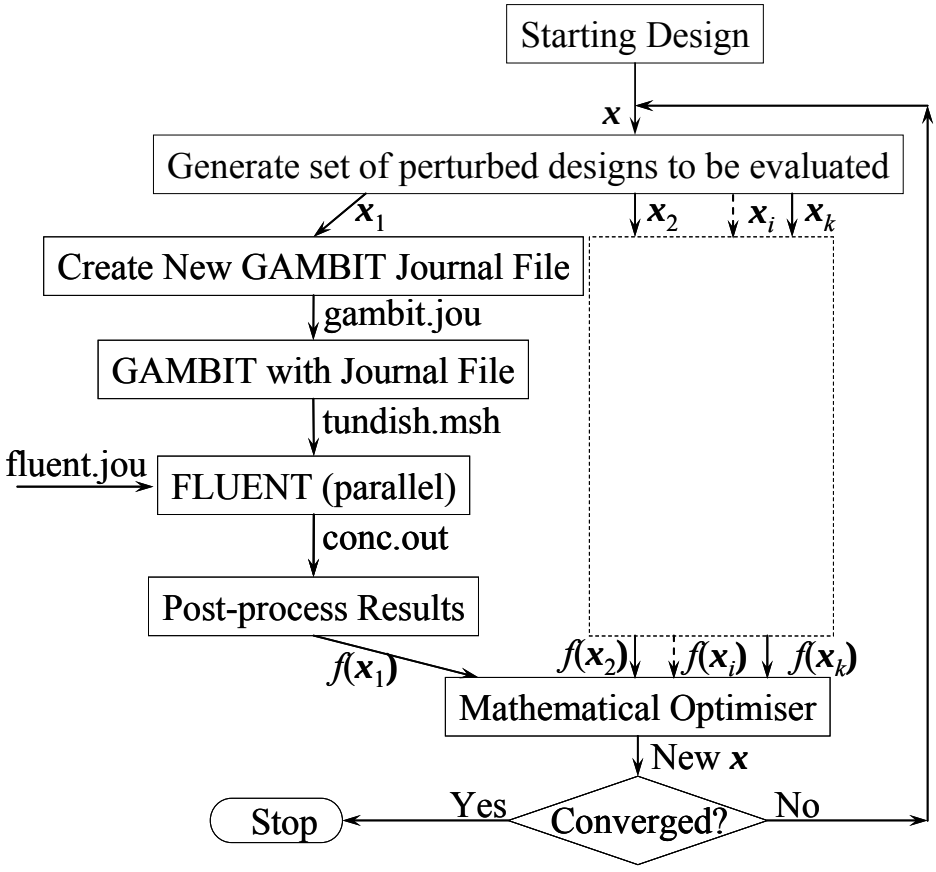

Figure 3-3: Flow diagram of FLUENT coupled to optimiser

3-5 CONCLUSION

This chapter described the methodologies investigated and developed to optimise tundish and tundish furniture. The first part of the methodology is to validate the

numerical model that will be used in the optimisation study. Secondly and the most important, is formulating the optimisation problem. This involves choosing the design variables and the appropriate object function and constraints. Typical design variables, objective function and constraint functions for tundish design were given and discussed. Lastly, the automation of the numerical set-up, solving and extraction of data were described. The following chapter will describe the application of this methodology to different case studies.

4

CHAPTER 4: APPLICATION OF TUNDISH DESIGN METHODOLOGY TO CASE STUDIES

4-1 INTRODUCTION

The design optimisation methodology developed in Chapter 3 has been tested on a number of different case studies. These case studies are given in detail in this chapter. The chapter starts with the optimisation of a simple 1-dam-1-weir configuration. The optimisation of a baffle follows next, with the optimisation of an impact pad and an impact pad with a dam forming the last two test cases.

4-2 CASE STUDY 1: OPTIMISATION OF 1-DAM-1-WEIR CONFIGURATION

The first case study involves the single-strand stainless steel continuous caster in operation at the Middelburg plant of Columbus Stainless. The work of this case study has been published in the Journal of Iron and Steel Institute of Japan International [69] and presented at the 20th International Congress of Theoretical and Applied Mechanics [70].

The tundish geometry considered is shown in Figure 4-1. The flow rate is controlled by the position of the stopper. When injecting a tracer element at the shroud (inlet), this tracer is detected at the SEN (outlet) after a certain amount of time. The concentration at the outlet increases to a maximum where after it decreases. The time history of the tracer concentration as measured at the outlet is called the Residence Time Distribution (RTD) in 2-2.2. The rate of decay is of interest since it correlates with the ratio of plug flow versus mixed flow in the tundish. The amount of tracer left in the tundish after $2\bar{t}$ (twice the mean residence time) is defined in this study as the

dead volume, and is minimised in the first optimisation problem. The second optimisation problem considers the removal of inclusion particles.

As mentioned before, a water model validation study was also undertaken on this specific tundish geometry to ensure the accuracy of the numerical model. The water model tests were done on a full-scale tundish installed at the University of Pretoria by other members of the research group. The results of the water model test and those obtained with numerical model compared favourably. Details of the validation study are given in Appendix A. Water is used as the modelling fluid for the first case study.

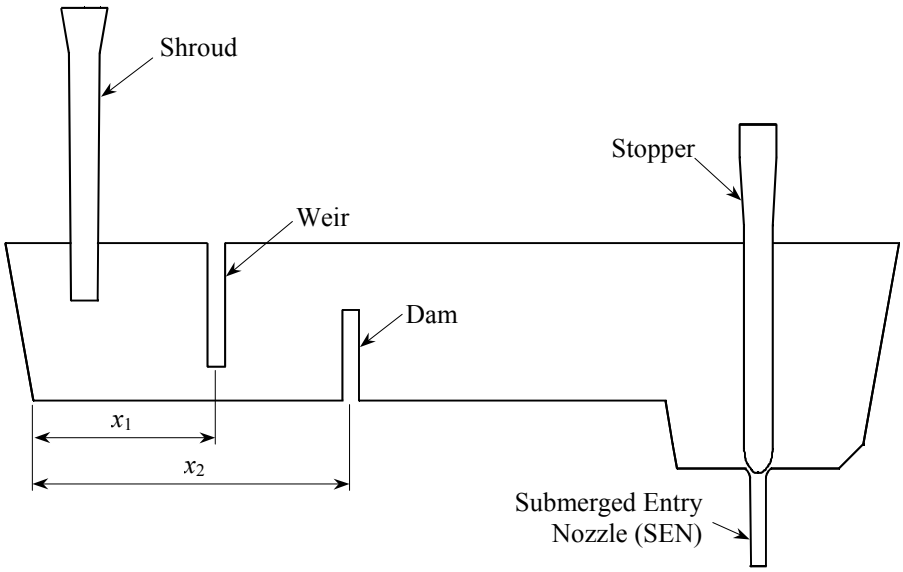

Figure 4-1: Side view of tundish showing dam, weir, stopper, SEN and shroud

The complete mathematical formulation of the optimisation problems, in which the inequality constraints are written in the standard form $g_j(\boldsymbol{x}) \leq 0$, where $\boldsymbol{x}$ denotes the vector of the design variables $(x_1, x_2)^{\mathrm{T}}$, are as follows:

Case 1a:

$$\text{Minimise}\begin{bmatrix} f(\mathbf{x}) = \text{dead volume} \\ = 1 - (\text{concentration at } t = 2\bar{t}) \end{bmatrix}$$

$$\text{subject to: } \begin{cases} g_1 = -x_1 + x_1^{\min} \le 0 \\ g_2 = x_1 - x_2 + \delta \le 0 \\ g_3 = x_2 - x_2^{\max} \le 0 \end{cases} \tag{4-1}$$

where δ is the minimum distance between the dam and the weir and $x_1^{\min}$ and $x_2^{\max}$ are the left most and right most positions of the weir and dam, respectively.

Case 1b:

$$\text{Minimise}\left[f(\mathbf{x}) = \text{Percentage Escaped particles}\right]$$

$$\text{subject to: } \begin{cases} g_1 = -x_1 + x_1^{\min} \le 0 \\ g_2 = x_1 - x_2 + \delta \le 0 \\ g_3 = x_2 - x_2^{\max} \le 0 \end{cases} \tag{4-2}$$

The results for the two cases of the 1-dam 1-weir configuration are presented next.

4-2.1 Case 1a: Dead Volume Minimisation

Parameters

The parameters used in this study are given in Table 4-1. The limits on the design variables and move limits are shown in Table 4-2.

Table 4-1: Parameters used in the numerical model

Parameter	Value
Mass Flow Rate [kg.s^{-1}]	4.75
Tundish Volume [m^3]	2.05
Dead Volume Time [s]	$2\bar{t}$ = 1176
Water density, ρ_{water}[kg.m^{-3}]	998
Water Viscosity, μ_{water} [kg.m^{-1}.s^{-1}]	0.00103
Minimum distance, δ [m]	0.2

Table 4-2: Upper and lower limits and move limits on the design variables

	Weir Position (x_1) [m]	Dam Position (x_2) [m]
Minimum	0.4629	-
Maximum	-	2.7266
Move Limit	0.5	0.5

Flow Results

The outlet concentration and the RTD curve for the initial design iteration ($x_1 = 0.9$, $x_2 = 1.5$) as obtained with a transient simulation are shown in Figure 4-2 and Figure 4-3 respectively. The curves end at $\bar{t} = 2.0$, i.e., 1176s = 19min35s. The dead volume is obtained from 1 minus the concentration at $\bar{t} = 2.0$ in Figure 4-2, since the integral of the curve in Figure 4-3 is equal to 1.0.

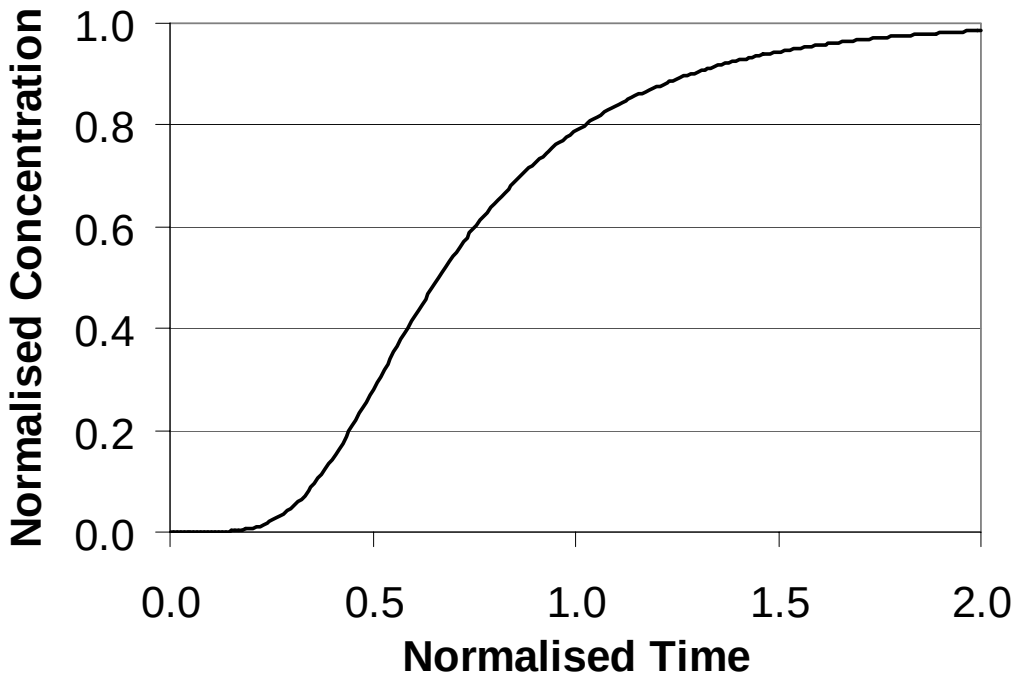

Figure 4-2: Concentration profile of starting configuration ($x_1 = 0.9$, $x_2 = 1.5$)

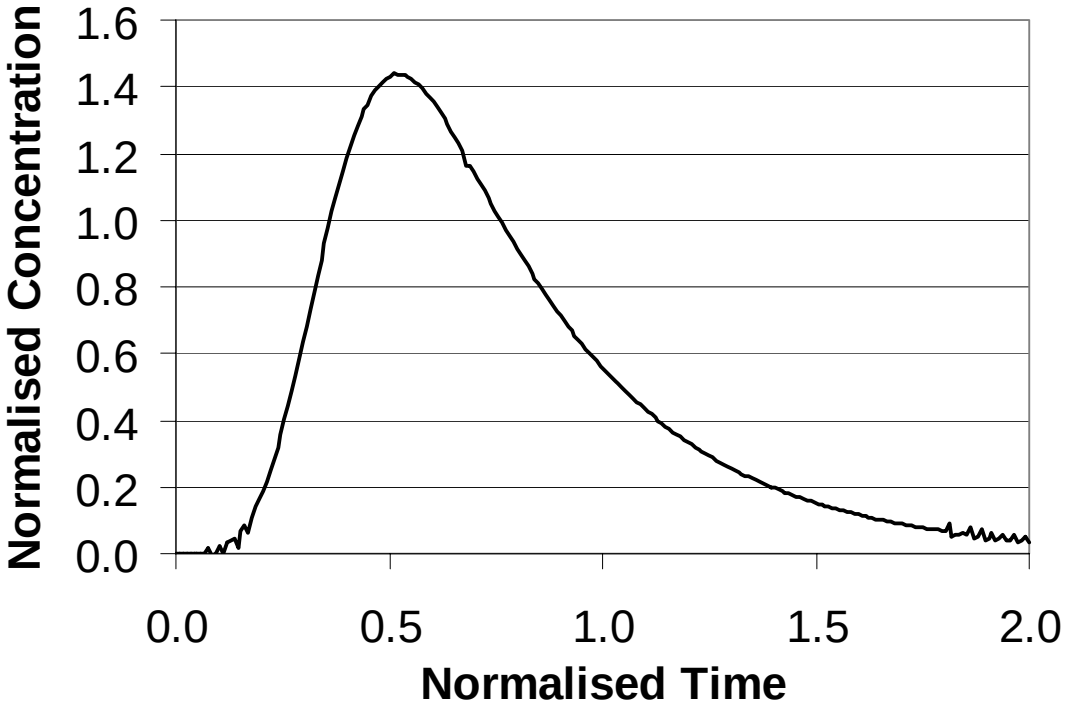

Figure 4-3: RTD curve of starting configuration (x_1 = 0.9, x_2 = 1.5)

Optimisation Results

The results of Case1a are shown in Figure 4-4 and Figure 4-5. The history of the objective function is shown in Figure 4-4 while the history of the design variables is shown in Figure 4-5. A graphical representation of the optimum configuration is also shown in Figure 4-5. It can be seen that the first potential optimum is found in iteration 4, where after the optimiser diverges, but then recovers to find a slightly better minimum. At iteration 4, the constraint on x_1 is only just not active, whereas from iteration 5 onwards, it remains active, with x_1 at its lowest allowable value. Physically, this means that the design pushes the weir as close to the inlet as possible, while it searches for the optimum position of the dam, relatively close to the outlet. The main deduction that can be made from the optimisation results for this two-variable design problem, is that the dead volume is relatively insensitive to the position of the dam and weir. Although the dead volume has been reduced to nearly half its value in the initial design, the dead volume was very small to begin with (1.45%).

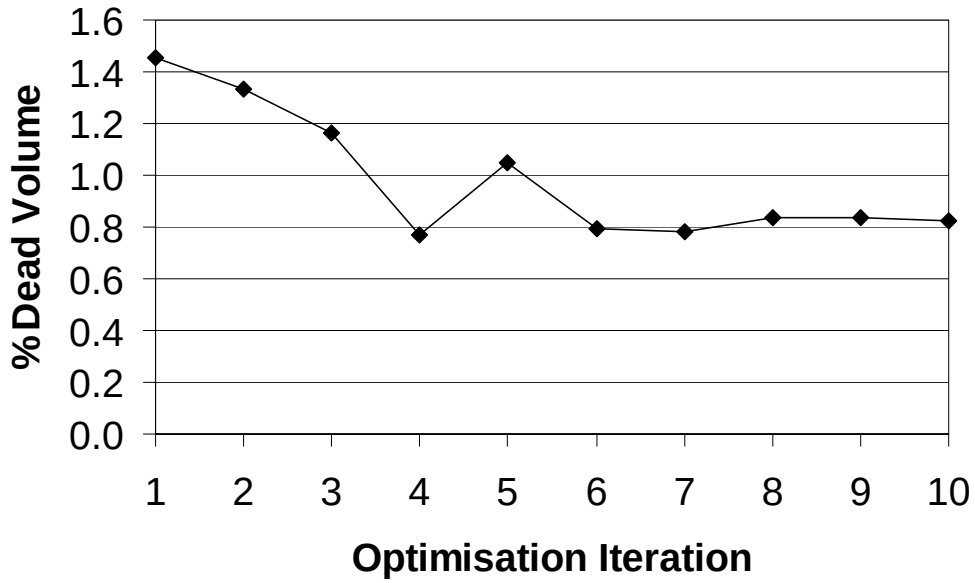

Figure 4-4: Optimisation history of objective function (Case 1a)

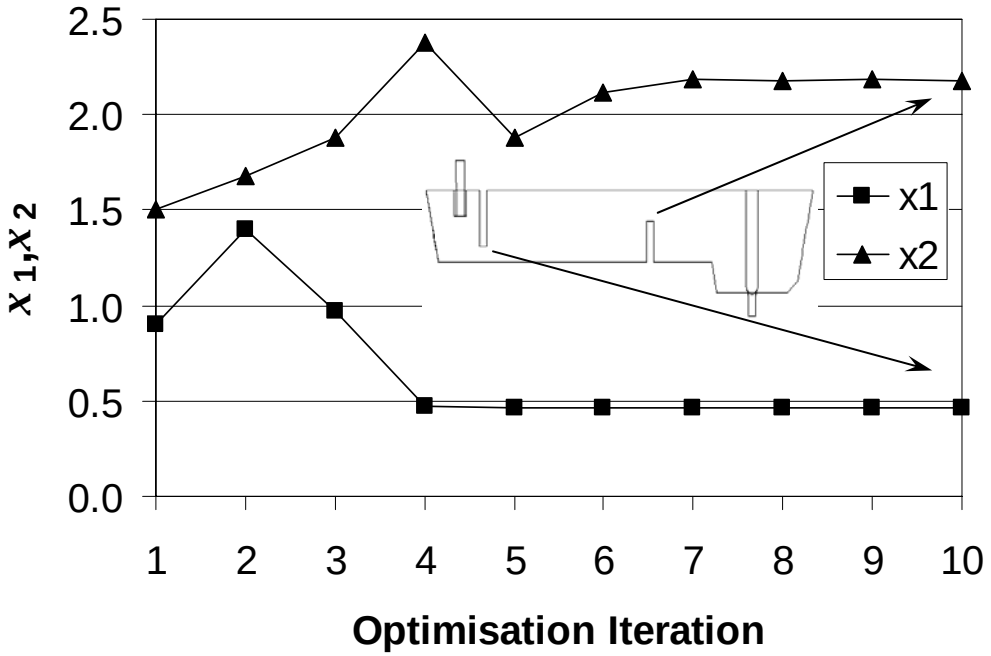

Figure 4-5: Optimisation history of design variables (Case 1a)

4-2.2 Case 1b: Inclusion Removal Optimisation

Parameters

The same parameters and limits on the design variables are used as in Case 1a. The only additional parameters considered is the inclusion size distribution, inclusion particle mass flow and density. The inclusion size distribution is given in Table 4-3. These data were acquired from taking a sample of the steel at the shroud on the plant and then using an image analyser to determine the size distribution. This information was obtained from ISCOR Vanderbijlpark Works [71]. The mass flow is determined from the total percentage of inclusions in the sample and was calculated as $0.469 g.s^{-1}$ for the whole tundish. The density of the inclusions was taken as $456 kg.m^{-3}$ which is 2.2 times smaller than the density of the water (the modelling fluid used). This represents the same density ratio of the alumina inclusions relative to the molten steel in the plant. A total of 2700 inclusions with the same size distribution as in Table 4-3 are released in the CFD simulation.

Table 4-3: Inclusions size distribution obtained from image analyser [71]

Size [mm]	Number of particles
0.024	113
0.093	37.75
0.207	4.5
0.366	0.5
0.571	0.25

Inclusion Tracks

The inclusion tracks for the starting design are shown in Figure 4-6 for two of the inclusion sizes considered (i.e. 0.024mm and 0.207mm), released at one specific location for illustration purposes. It can be seen that the all the larger inclusion are trapped at the slag layer before the weir due to their larger buoyancy forces (Figure 4-6a). The smaller inclusions tend to follow the flow stream and exit at the SEN (Figure 4-6b).

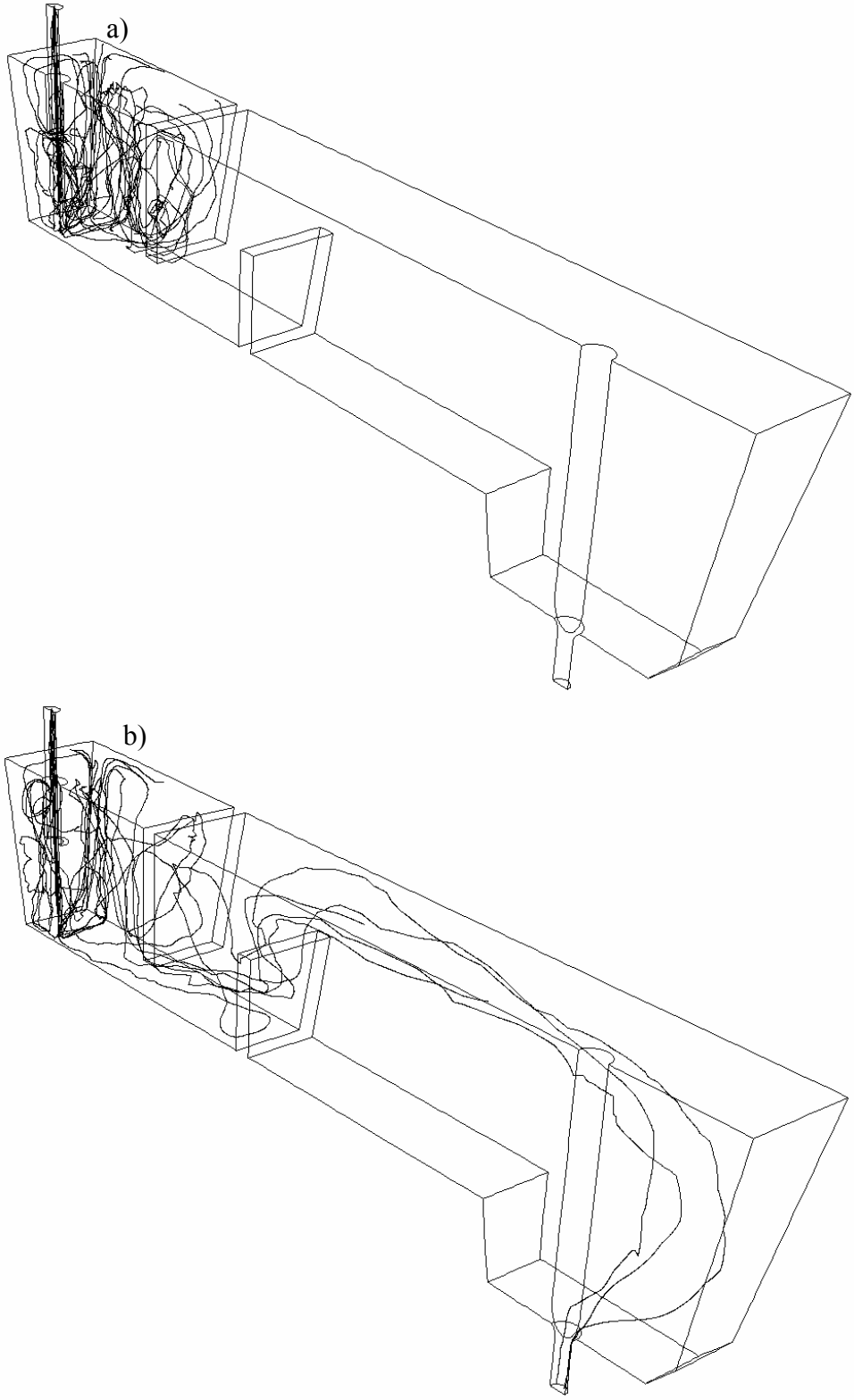

Figure 4-6: Particle tracks for a) 0.207mm b) 0.024mm size inclusions released at one specific location only (Starting configuration: x_1 = 0.9, x_2 = 1.5)

Optimisation Results

The history of the inclusion optimisation is shown in Figure 4-7 and Figure 4-8. The history of the objective function is shown in Figure 4-8, while the history of the design variables is shown in Figure 4-8. It can be seen from Figure 4-8 that the optimiser tends to hit the constraint of minimum distance (δ) between the dam and the weir, and then moves the dam and weir together as a pair. A graphical representation of the optimum configuration is also shown in Figure 4-8. This small distance between the dam and the weir creates a jet with a high velocity directed towards the surface providing a mechanism for particle trapping. This may however cause some entrainment of the slag layer, which was not modelled in this case due to the absence of a free surface in the CFD model.

The reduction in the objective function is quite small as can be seen in Figure 4-7. This shows that the inclusion removal capability of this tundish with these given tundish furniture and constraints are not very good. Also, the improvements that can be made to the design to increase the inclusion removal capability are not great.

It can also be seen that this optimum differs completely from the optimum in Case 1a. The main reason for this is that the two objective functions represent two opposing design criteria.

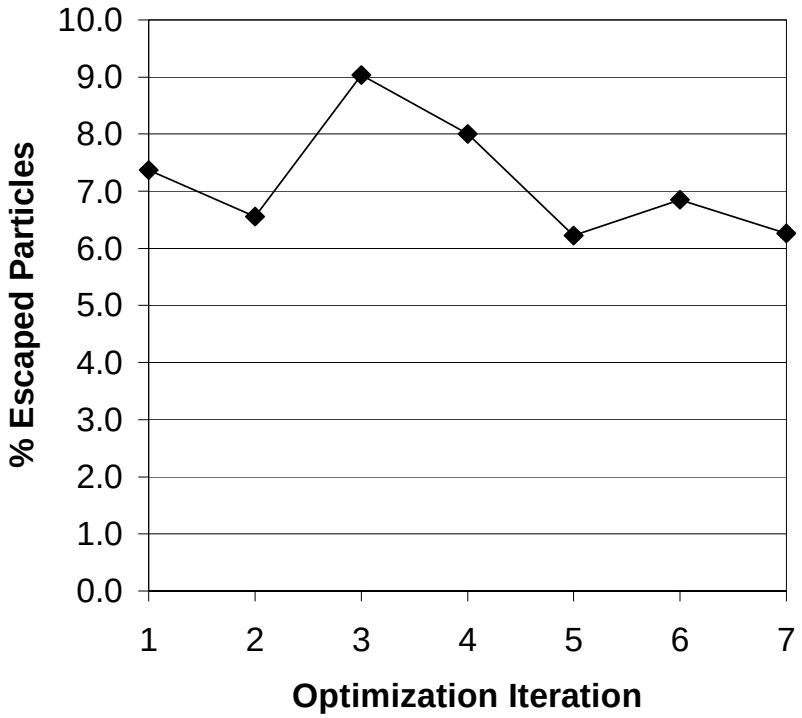

Figure 4-7: Optimisation history of the objective function (Case 1b)

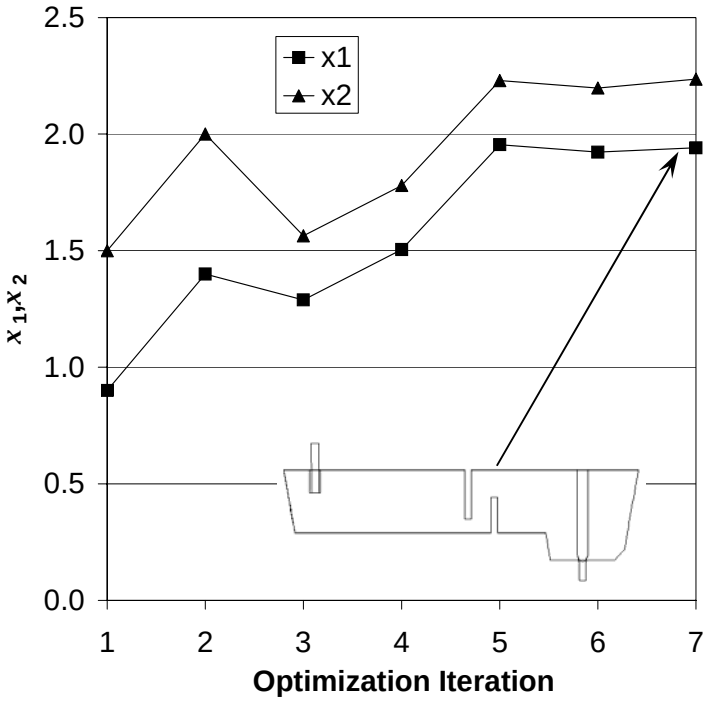

Figure 4-8: Optimisation history of the design variables (Case 1b)

4-2.3 Conclusion

A simple dam and weir configuration was optimised for the single-strand continuous caster of Columbus Stainless Steel. Two different objective functions were defined for two different cases under investigation. It was shown that different optima exist for these different objective functions.

4-3 CASE STUDY 2: BAFFLE OPTIMISATION

This study considers the two-strand continuous caster at ISCOR Vanderbijlpark Works, South Africa. ISCOR was in the process of enlarging the tundish capacity of their two-strand continuous caster from 40 tonnes to 60 tonnes. Part of the consideration of the increased capacity was to design the tundish and tundish furniture in order to improve steel quality. The main design criterion was to improve the cleanliness of the steel produced by this caster. This work has been presented at the 4th European Continuous Casting Conference [72] and published in the Ironmaking and Steelmaking journal [68].

As the caster operates with long sequences, the Minimum Residece Time (MRT) of the tundish is maximised both at operating level and at a typical transition level of 700mm from the bottom of the tundish. A high MRT implies increased plug flow which has been linked to increased inclusion removal. In the numerical model, the MRT is obtained by injecting a passive scalar at the inlet and calculating the time it takes to appear at the outlet. The MRT is defined mathematically, as the non-dimensional time when the outlet concentration of the scalar reaches 0.1% of the constant inlet concentration. The time is non-dimensionalised using the theoretical mean residence time. The optimisation algorithms used in this case study (DYNAMIC-Q and LS-OPT) allow for one objective function. Therefore when two criteria are optimised, it is customary to consider a weighted combination as the objective function. Since the tundish operates predominantly at full level but quality during transition is also of concern, it was decided to combine the two respective MRTs in a 70:30 ratio.

Six geometrical variables of the tundish and tundish furniture are used as design variables. The six design variables are shown graphically in Figure 4-9.

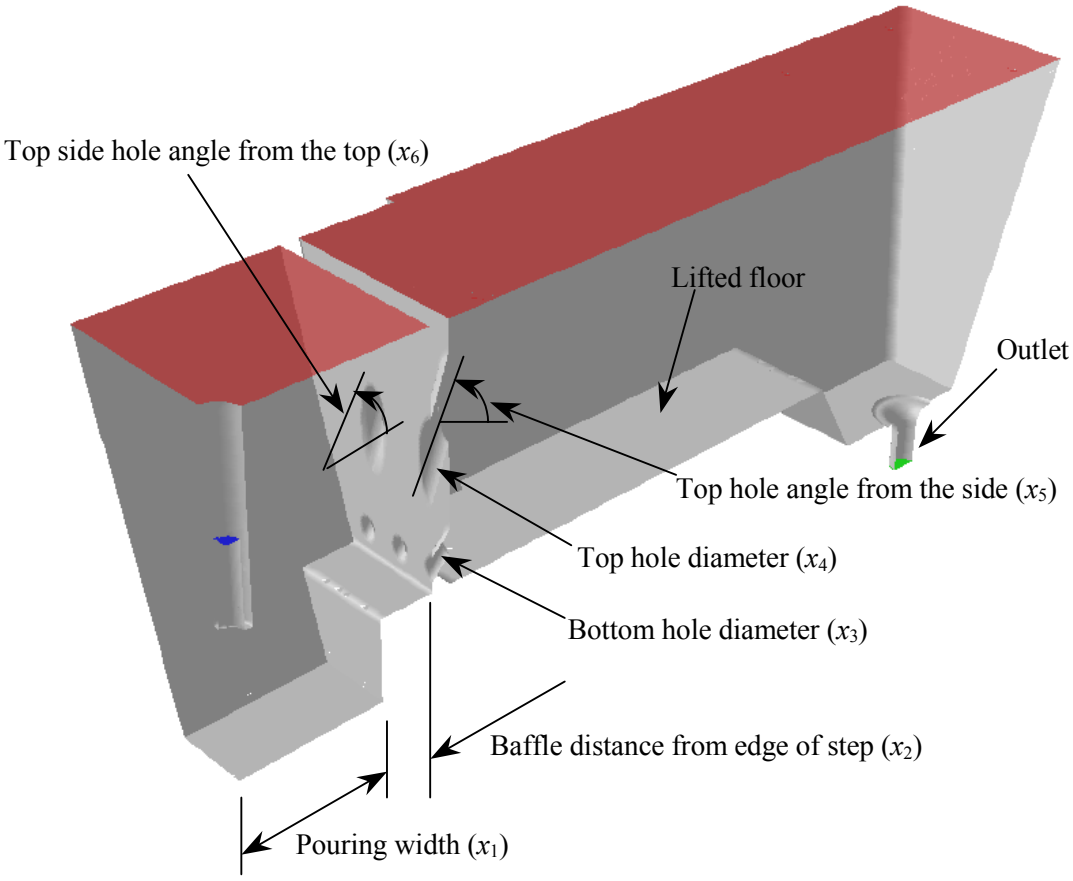

Figure 4-9: Graphical depiction of the design variables (1/4 symmetrical model) (Case 2)

Apart from the design variables chosen, the values of other parameters that were held fixed during the optimisation are shown in Figure 4-10 and enumerated in Table 4-4.

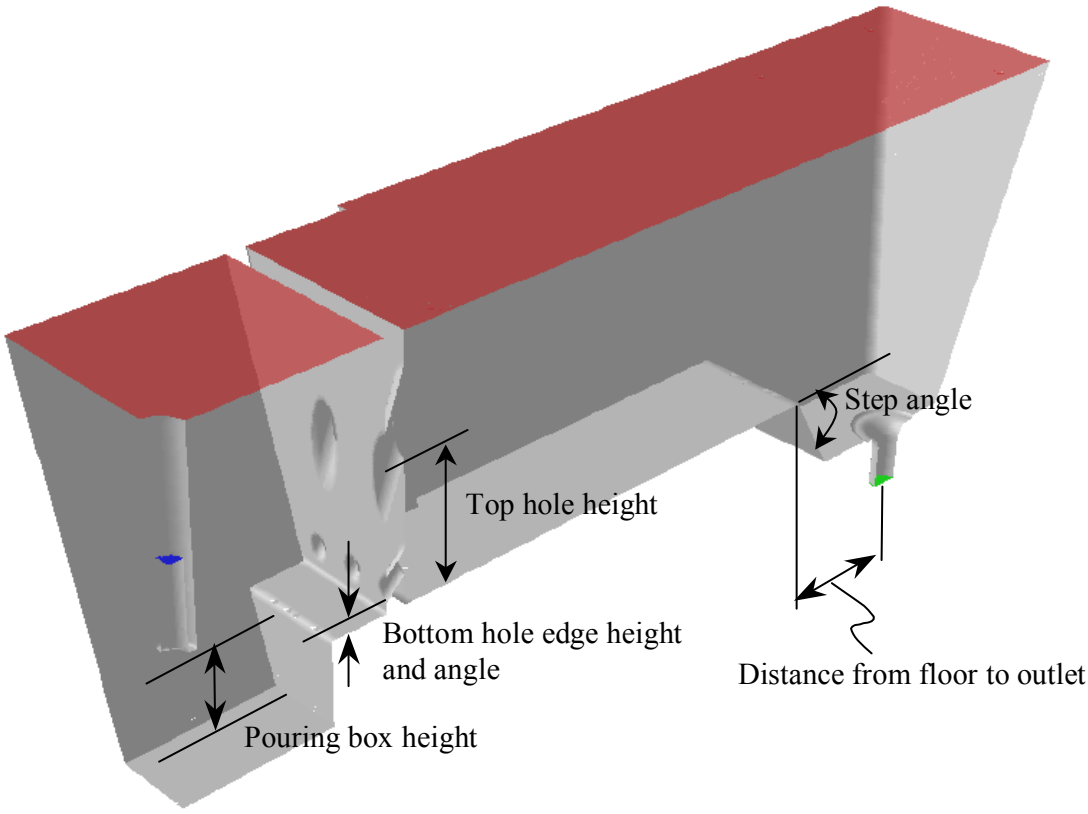

Figure 4-10: Fixed parameters for optimisation of tundish (1/4 symmetrical model) (Case 2)

Table 4-4: Fixed parameters of optimisation problem (Case 2)

Parameter	Value
Bottom hole angle [°]	45
Pouring box height [mm]	300
Distance from floor to outlet [mm]	350
Step angle (at outlet) [°]	80
Bottom hole edge height (from lifted floor) [mm]	50
Top hole height (centre from lifted floor) [mm]	450

The complete mathematical formulation of the optimisation problem, in which the constraints are written in the standard form $g(\boldsymbol{x}) \leq 0$, where $\boldsymbol{x}$ denotes the vector of the design variables $(x_1, x_2, x_3, x_4, x_5, x_6)^T$, is as follows:

$$\text{Maximise } \left[f(\boldsymbol{x}) = 0.7 \times MRT_{full}(\boldsymbol{x}) + 0.3 \times MRT_{700mm}(\boldsymbol{x}) \right],$$

$$\text{subject to: } \begin{cases} g_j = -x_j + x_j^{\min} \le 0; j = 1,2,3\ldots,n \\ g_{j+n} = x_j - x_j^{\max} \le 0; j = 1,2,3\ldots,n \\ g_{2n+1} = \dfrac{x_4}{\cos x_5} + 70 \tan x_5 - 400 \le 0 \end{cases} \quad (4\text{-}3)$$

where $x_j^{\min}$ and $x_j^{\max}$ are suitable minimum and maximum constraints or bounds for the j-component of the design vector, $\boldsymbol{x}$, and $n = 6$. The upper and lower bounds on the variables are given in Table 4-5. No upper bounds are placed on four of the variables. The last constraint in equation (4-3) is derived from the fact that the exit of the top hole should be 50mm below the full operating level of the tundish to prevent possible slag entrainment. For the 700mm level, this hole protrudes above the liquid steel level.

Table 4-5: Minimum and maximum values of design variables (Case 2)

Variable	Minimum	Maximum	Starting Design
Pouring width (x_1) [mm]	250	1075	300
Baffle distance (x_2) [mm]	50	N/A	100
Bottom hole diameter (x_3) [mm]	50	N/A	70
Top hole diameter (x_4) [mm]	50	N/A	100
Top hole angle from side (x_5) [°]	-70	N/A	70
Top hole angle from top (x_6) [°]	-10	10	0

4-3.1 Flow Modelling

Grid

The grids used throughout the optimisation contained about 375 000 and 200 000 cells respectively for the full and half-full (700mm level) cases after refinement. Refinement was based on y^+-values to ensure the correct implementation of the wall-function approach used in the turbulence modelling [33]. A typical grid at operating level used in the optimisation is

shown in Figure 4-11 while a typical grid at transition level is give in Figure 4-12. A section of the internal cells is shown in these figures. A close-up of this section close to the wall is also given. It can be seen that tetrahedral cells combined with prisms cells at the wall boundaries were used. The prisms cells give a good quality mesh near the wall of the tundish for good representation of the moment and thermal boundary layer due to the no-slip condition on the wall.

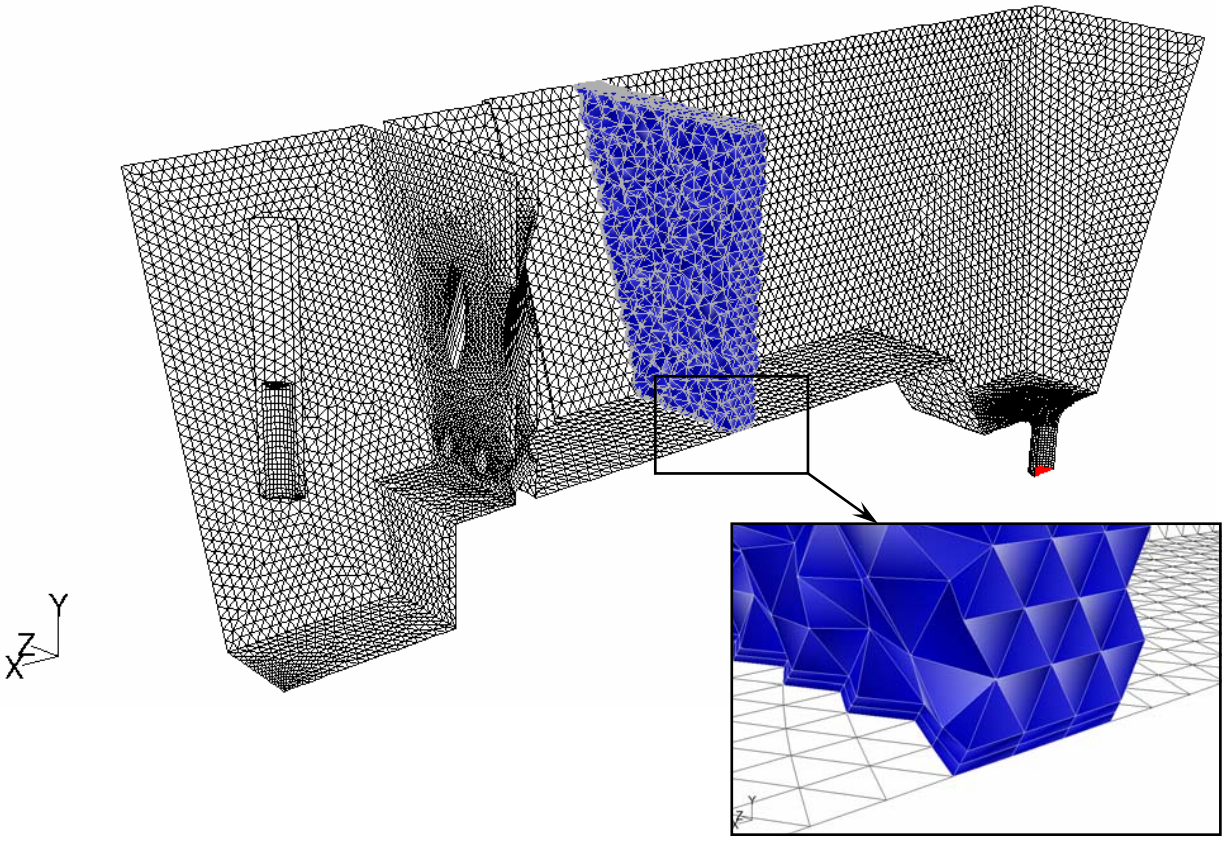

Figure 4-11: Typical grid at operating level (Case 2)

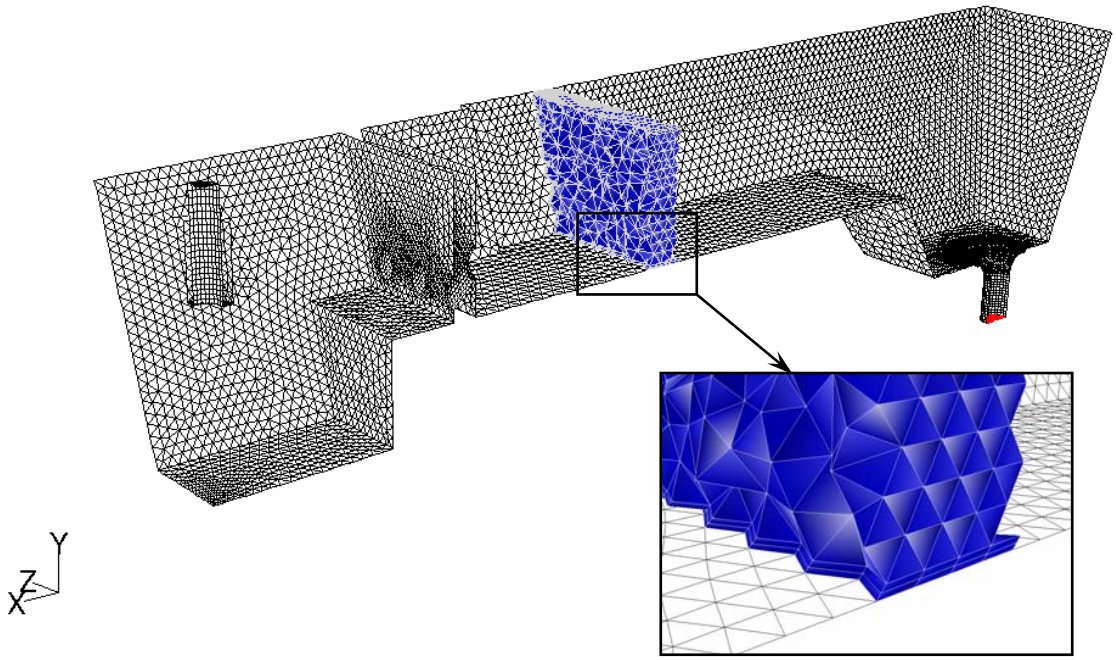

Figure 4-12: Typical grid at transition level (Case 2)

Boundary Conditions and Fluid Properties

The boundary conditions used in the CFD model are shown in Figure 4-13. The effective heat transfer coefficients of the slag layer, side and bottom walls of the tundish are also indicated in Figure 4-13. These values were calculated using the thermal properties of the tundish walls given in Table 4-6 as well as experimental correlations [73] that determine the natural convective heat transfer and radiation on the outside walls of the tundish. The lifted floor of the tundish and the baffle are assumed to be adiabatic. The properties of the liquid steel used are given in Table 4-7.

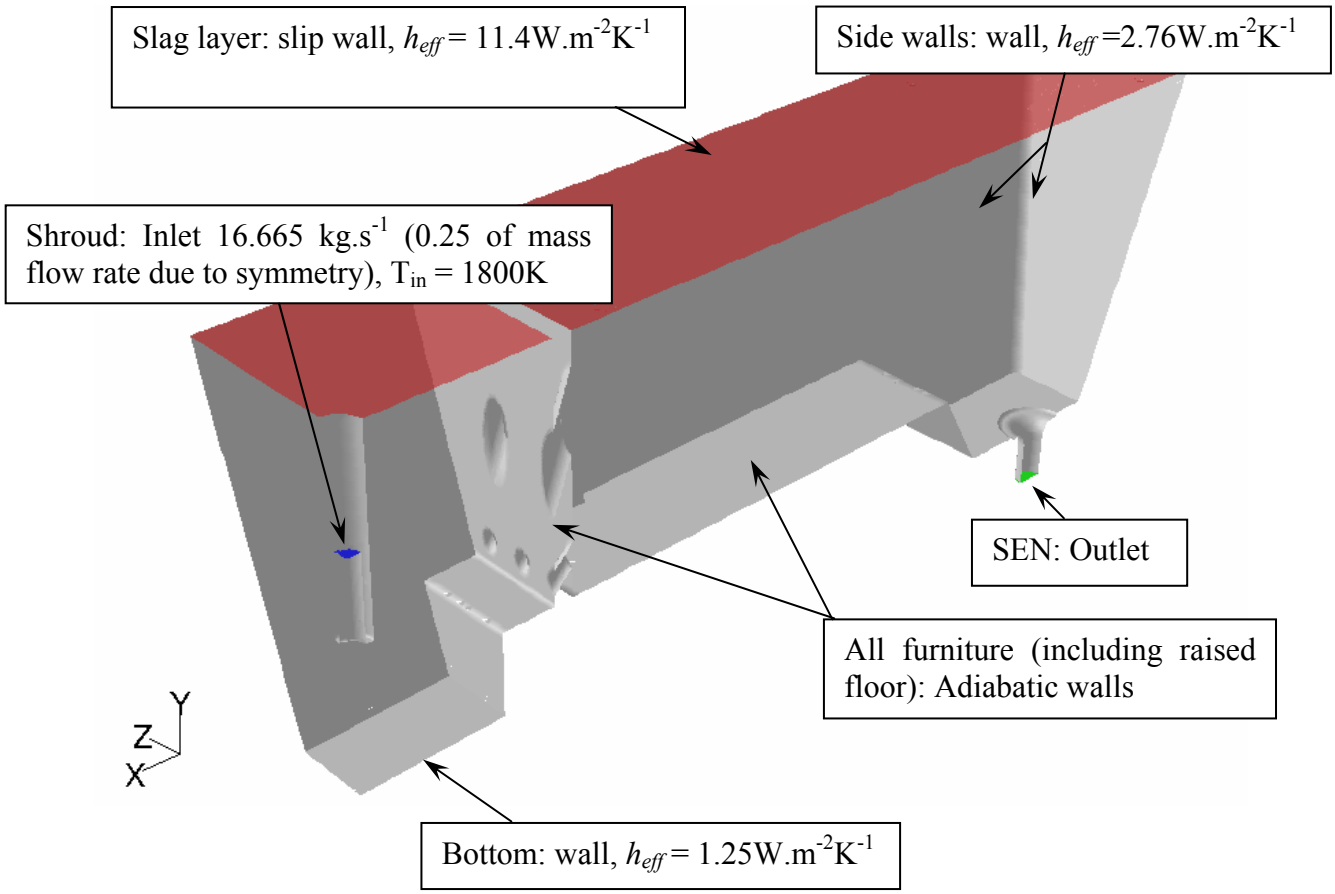

Figure 4-13: Boundary conditions used in tundish model (Case 2)

Table 4-6: Thermal properties of tundish (Case 2)

	Tundish construction	Insulation	Safety lining	Back lining	Work lining
Thickness [m]	0.03	0.025	0.025	0.114	0.04
Conductivity [W.m^{-1}.K^{-1}]	72.93	0.15	1.48	1.57	1.65

Table 4-7: Properties of liquid steel (Case 2)

Property	Value
Thermal expansion coefficient [K^{-1}]	1.1970×10^{-4}
Reference density [$kg.m^{-3}$]	7026.8
Reference temperature [K]	1800
Specific heat coefficient of steel [$J.kg^{-1}.K^{-1}$]	822
Conductivity of liquid steel [$W.m^{-1}.K^{-1}$]	52.535
Dynamic viscosity of steel [Pa.s]	5.3×10^{-3}

Solver

For the simulations presented in this study, the Reynolds-Averaged Navier-Stokes equations are solved using the segregated solver available in FLUENT. The standard k-ε turbulence model is used to provide turbulent closure. Second-order discretisation is used for all the flow equations while a three-order drop in the sum of the scaled residuals was considered to constitute a converged solution.

4-3.2 Flow Simulation Results

Typical results obtained from the CFD simulations are given in this section. The starting design RTD curves for the operating level and transition level are given in Figure 4-14 and Figure 4-15 respectively. The spikes in the RTD curve are indicative of possible short-circuiting in the tundish. The RTD data for the starting design for the operating level and transition level are given in Table 4-8.

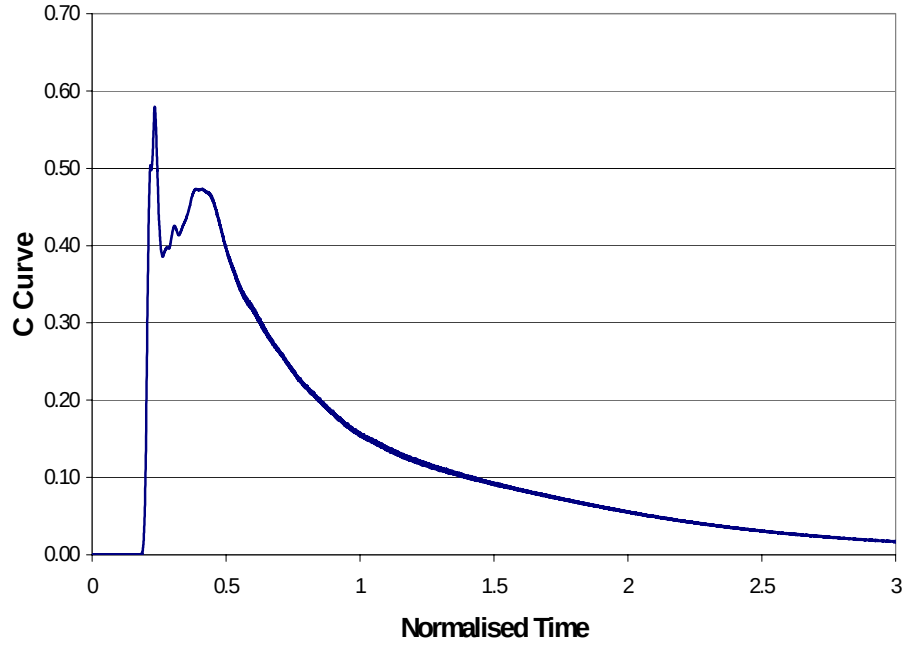

Figure 4-14: RTD obtained from CFD simulation for starting design at operating level ($x = (300,100,70,100,70,0)^T$ and MRT=0.189) (Case 2)

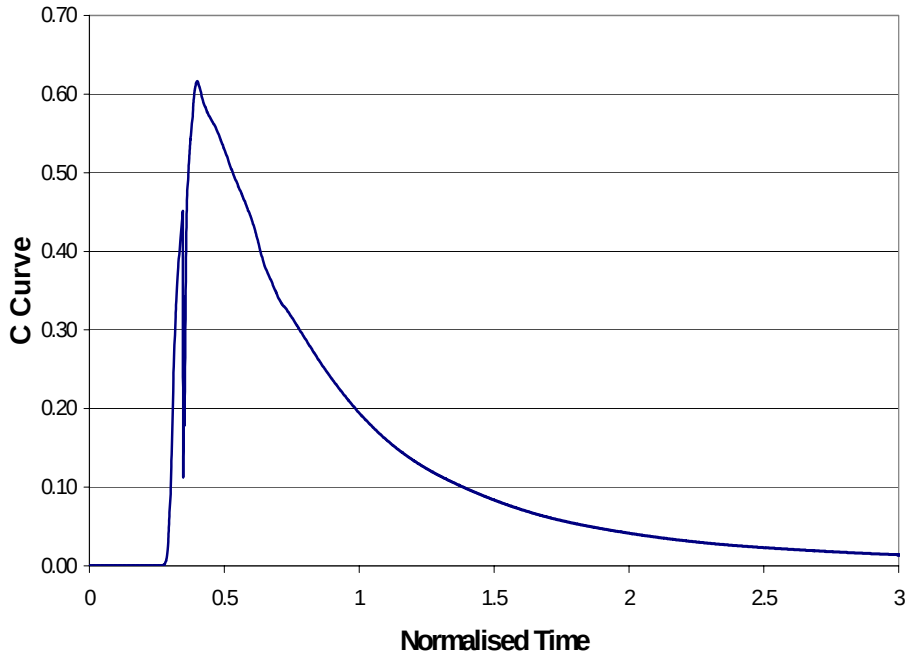

Figure 4-15: RTD obtained from CFD simulation for starting design at transition level ($x = (300,100,70,100,70,0)^T$ and MRT=0.283) (Case 2)

Table 4-8: RTD data for starting design ($x = (300,100,70,100,70,0)^T$)(Case 2)

	Full	700mm Level
Dispersed Plug Flow [%]	21.2	34.2
Dead Volume [%]	23.2	19.9
Mixed Volume [%]	55.7	46.0
MRT (non-dimensionalised)	**0.189**	**0.283**
PRT (non-dimensionalised)	0.234	0.400
AMRT (non-dimensionalised)	0.768	0.801

Path lines for the starting design are given in Figure 4-16 for the full operating level. Figure 4-16 shows that the tundish flow exhibits a large recirculation zone behind the baffle. Temperature contours for the operating level are given in Figure 4-17. As expected, the steel is the hottest in the pouring box region, with the coolest regimes being in the cornets above the tundish outlet. The hot jet of steel that is caused by the baffle holes can also be clearly seen in Figure 4-17.

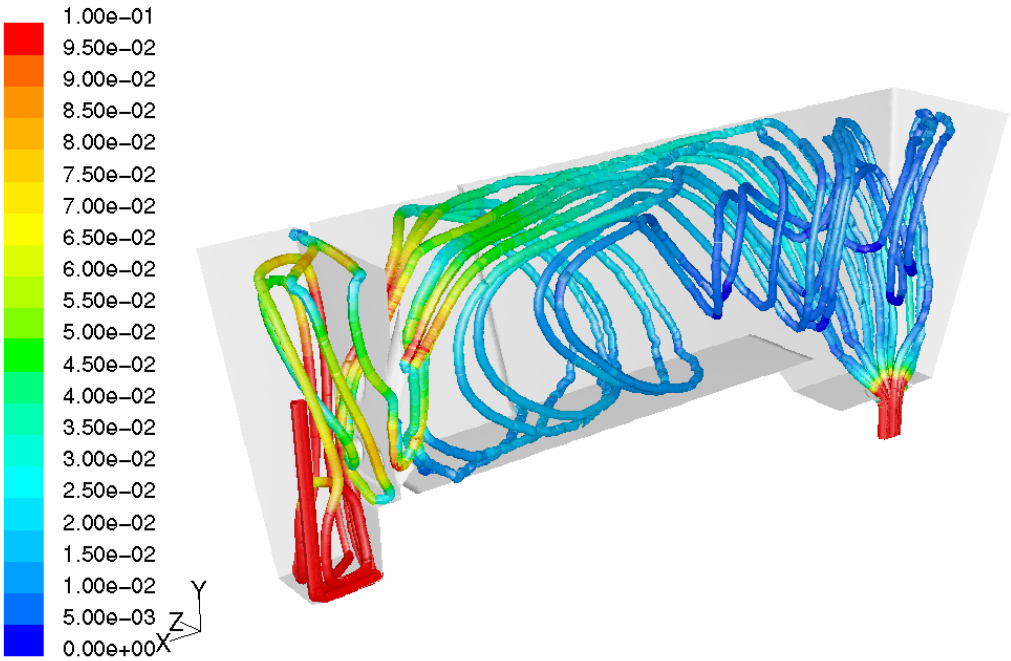

Figure 4-16: Path lines coloured by velocity magnitude [m.s^{-1}] from CFD simulation at full operating level for starting design ($x = (300,100,70,100,70,0)^T$) (Case 2)

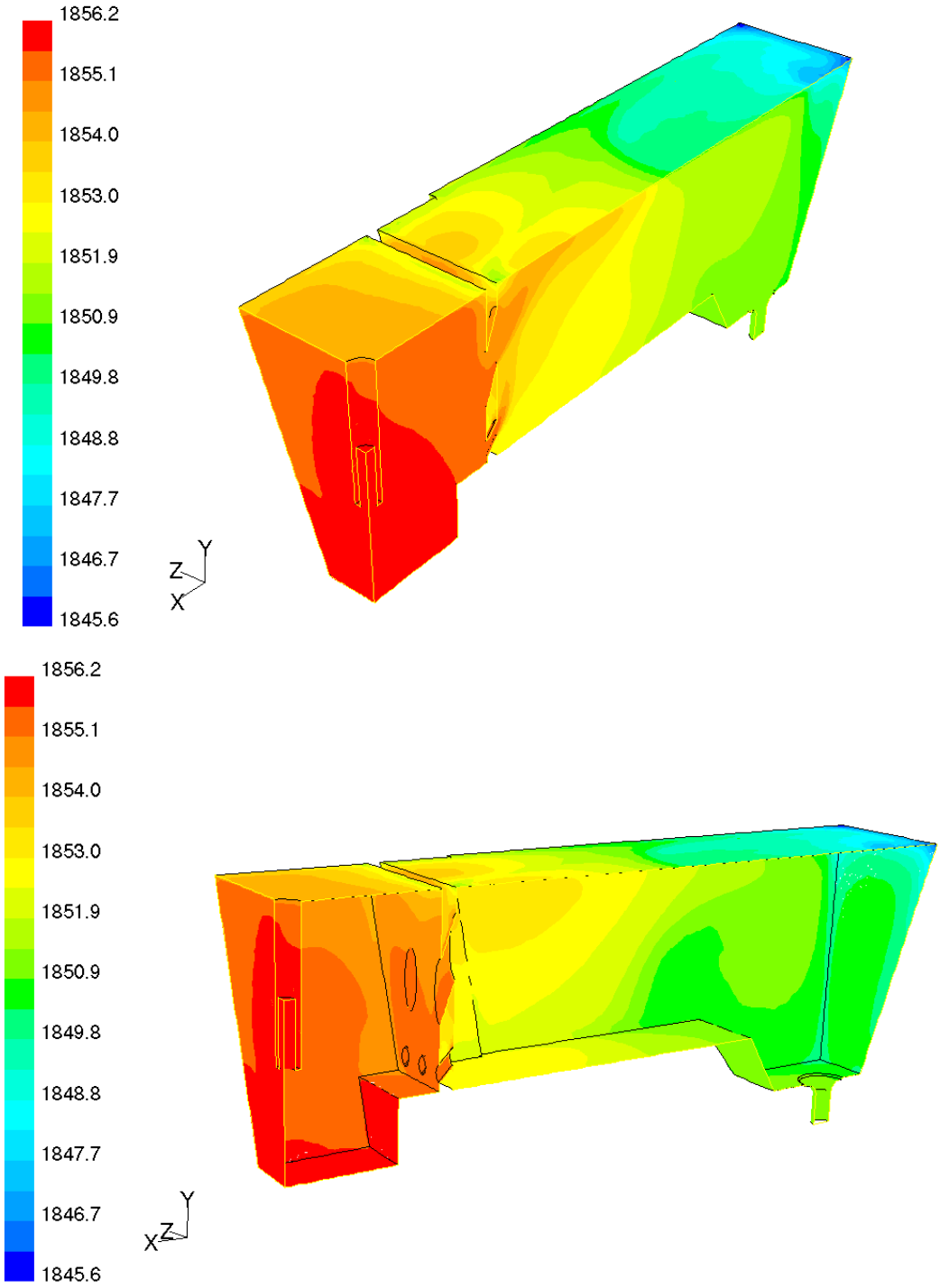

Figure 4-17: Typical temperature contours [K] at full operating level ($\boldsymbol{x} = (300,100,70,100,70,0)^T$) (Case 2)

A validation study between on-site measurements (provided by ISCOR Vanderbijlpark) and the CFD modelling was also conducted to ensure the

validity of the CFD model. The results from this study are given in Appendix B.

4-3.3 Optimisation Results (DYNAMIC-Q)

The results of the optimisation run obtained using the DYNAMIC-Q algorithm are given and discussed in this section. Figure 4-18 shows the optimisation history of the objective function as well as the MRT for operating level and at 700mm level. It can be seen that the objective function essentially levels out after 4 design iterations showing that the objective function has converged. The MRT for the operating level increased from 0.18 to 0.43 which represents an increase of 138%, while the MRT for the 700mm level increased from 0.29 to 0.31 which is an increase of 6.9%. The weighted combination of these two values (the objective function) can be seen to be dominated by the full operating level value. This relative insensitivity of the transition level MRT with respect to the design variables, is partly due to the fact that only 3 of the 6 variables influence the performance at the lower level, due to the fact that the upper hole in the baffle protrudes above the liquid steel at this level.

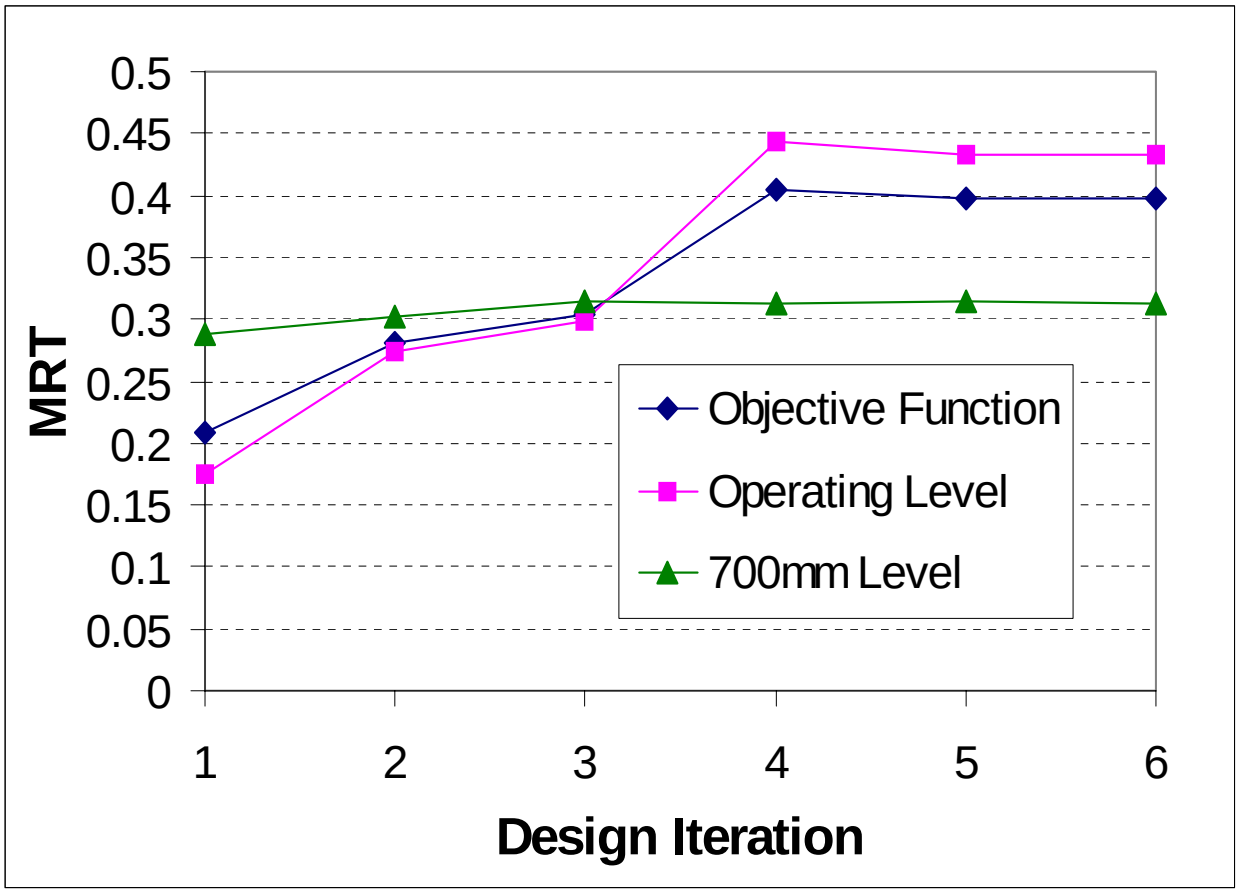

Figure 4-18: Optimisation history of objective function (DYNAMIC-Q) (Case 2)

Figure 4-19 shows the optimisation history of the design variables. An interesting fact to note is that the design variables are still changing after the 4th design iteration although the objective function has levelled off. This fact indicates that the last three designs in the optimisation run all have the same MRT although their geometries differ.

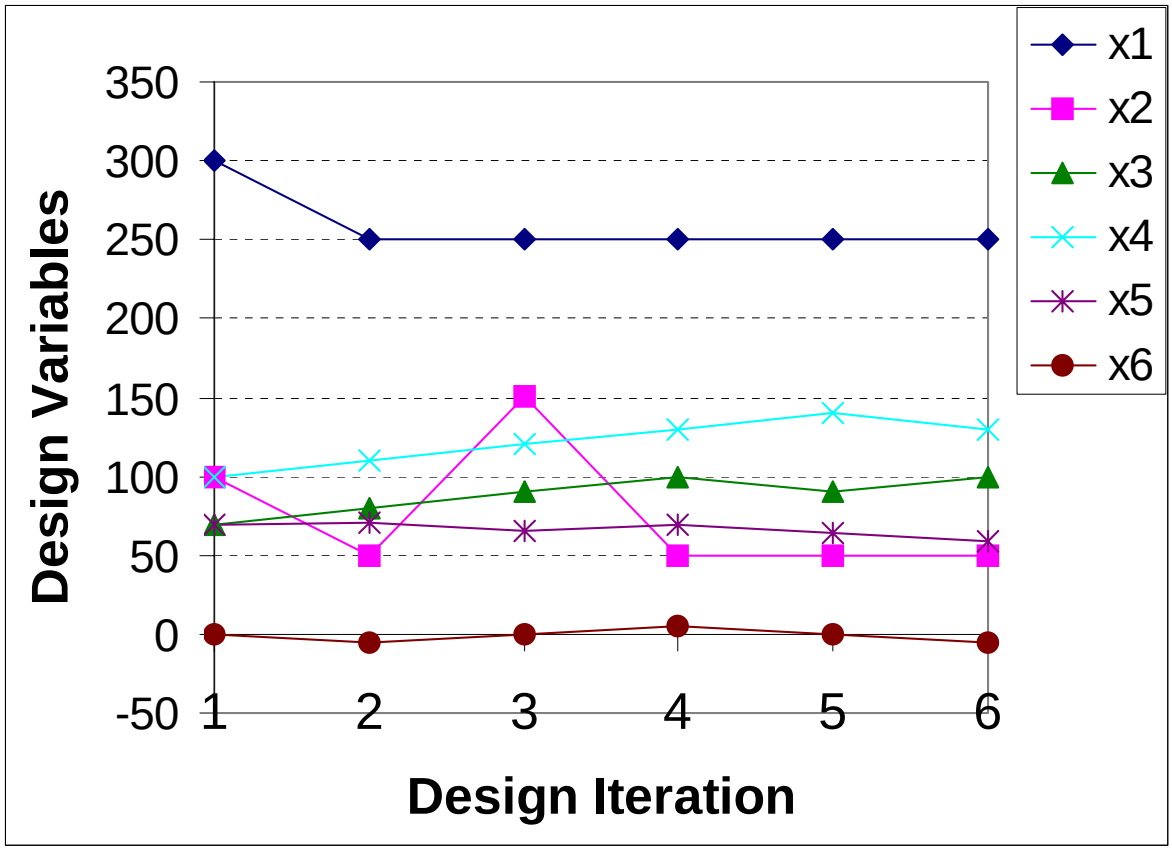

Figure 4-19: Optimisation history of design variables (DYNAMIC-Q) (Case 2)

Both the pouring box width (x_1) and the baffle position (x_2) converged to their respective allowable minimum values. The bottom hole diameter (x_3) increased, while the top hole diameter (x_4) and the top hole angle as seen from the side (x_5) found a certain combination to establish a favourable flow pattern inside the tundish. The value of the top side hole angle as seen from the top (x_6) oscillated around zero degrees, and the objective function seems to be relatively insensitive to this design variable.

4-3.4 Optimisation Results (LS-OPT)

It can be seen that the objective function using LS-OPT essentially levels out after three design iterations showing that the objective function has converged (Figure 4-20). Due to the nature of the response surface approximation used in LS-OPT, it requires approximately 1.5 more simulations per optimisation iteration than DYNAMIC-Q. This implies that more or less the same number

of function evaluations (or CFD simulations) was performed for both DYNAMIC-Q and LS-OPT to achieve their respective optima.

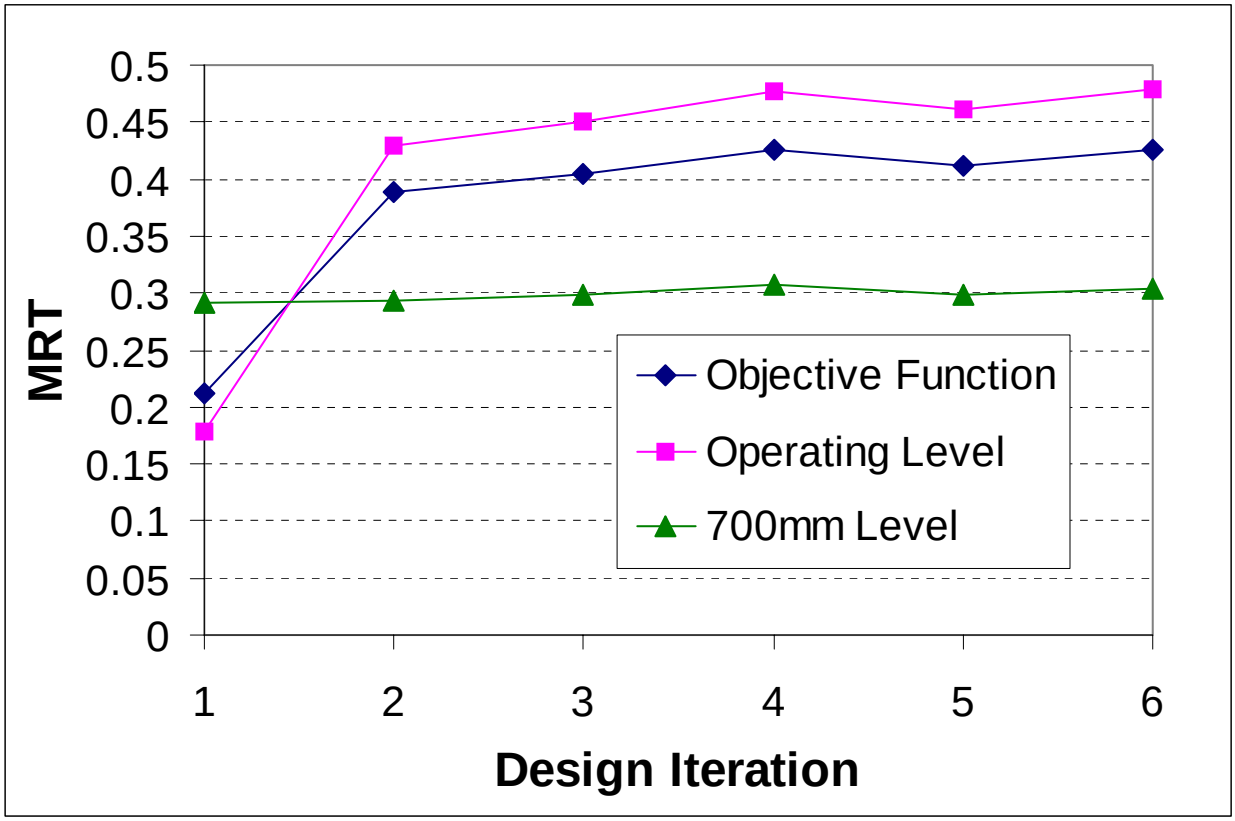

Figure 4-20: Optimisation history of objective function (LS-OPT) (Case 2)

The MRT for the operating level increased from 0.18 to 0.48, which represents an increase of 167%, while the MRT for the 700mm level again proved insensitive to the design changes. When using LS-OPT, x_3, x_4 and x_5 converge to different values, while x_1 and x_2 again reached their respective minimum values (Figure 4-21).

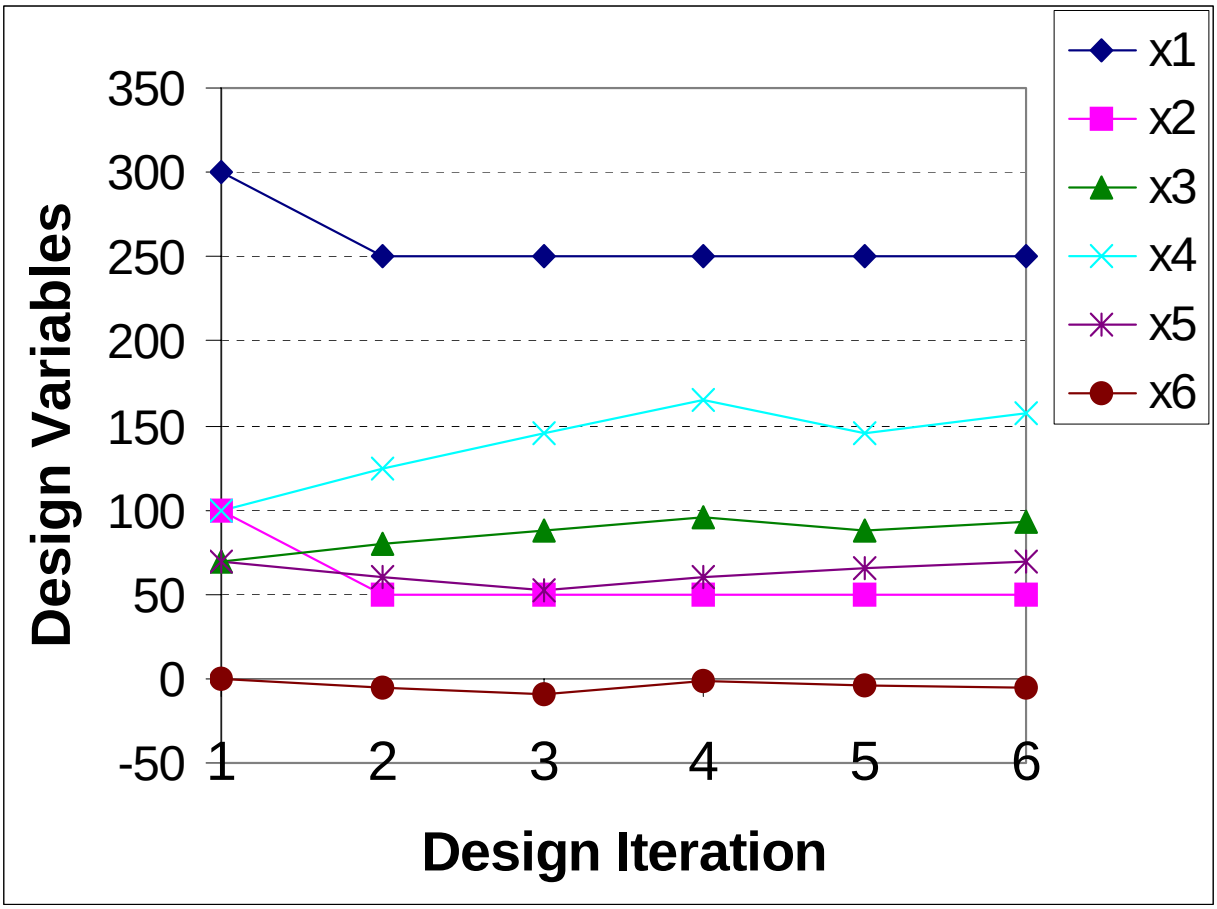

Figure 4-21: Optimisation history of design variables (LS-OPT) (Case 2)

The differences in the optimum design obtained by Dynamic-Q and LS-OPT are visually shown in Figure 4-22 together with the starting design. The difference between the MRT of the two optima obtained is mainly due to the top baffle hole diameter and angle. In the case of the optimum of DYNAMIC-Q, the top baffle hole diameter and angle is smaller than the optimum design obtained by LS-OPT. These smaller values have the effect of a higher velocity jet directed towards the outlet of the tundish. In turn, this has the effect that the MRT of the optimum obtained with DYNAMIC-Q is slightly less than that obtained with LS-OPT.

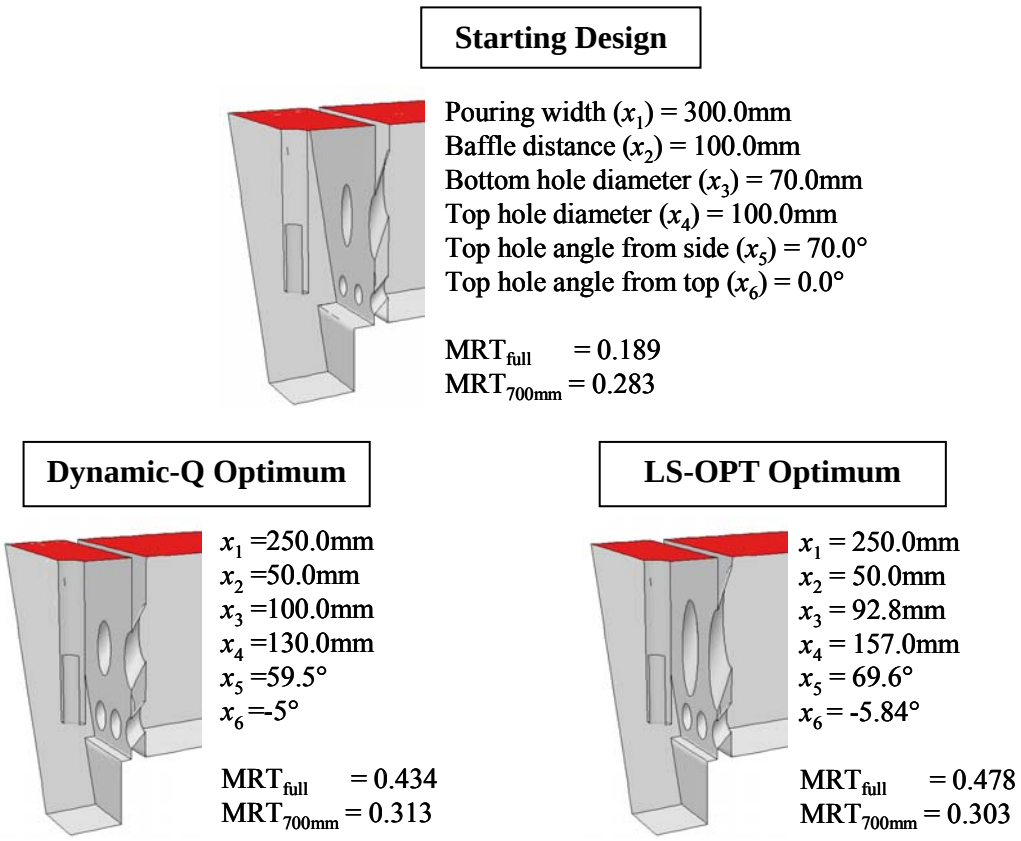

Figure 4-22: Starting and final designs (DYNAMIC-Q and LS-OPT) (Case 2)

A comparison of the surface Turbulent Kinetic Energy (TKE) for the starting design and the optima of Dynamic-Q and LS-OPT is given in Figure 4-23. The TKE for the two optima is higher then the starting design in the pouring box area, while the TKE downstream of the baffle is lower for the two optima.

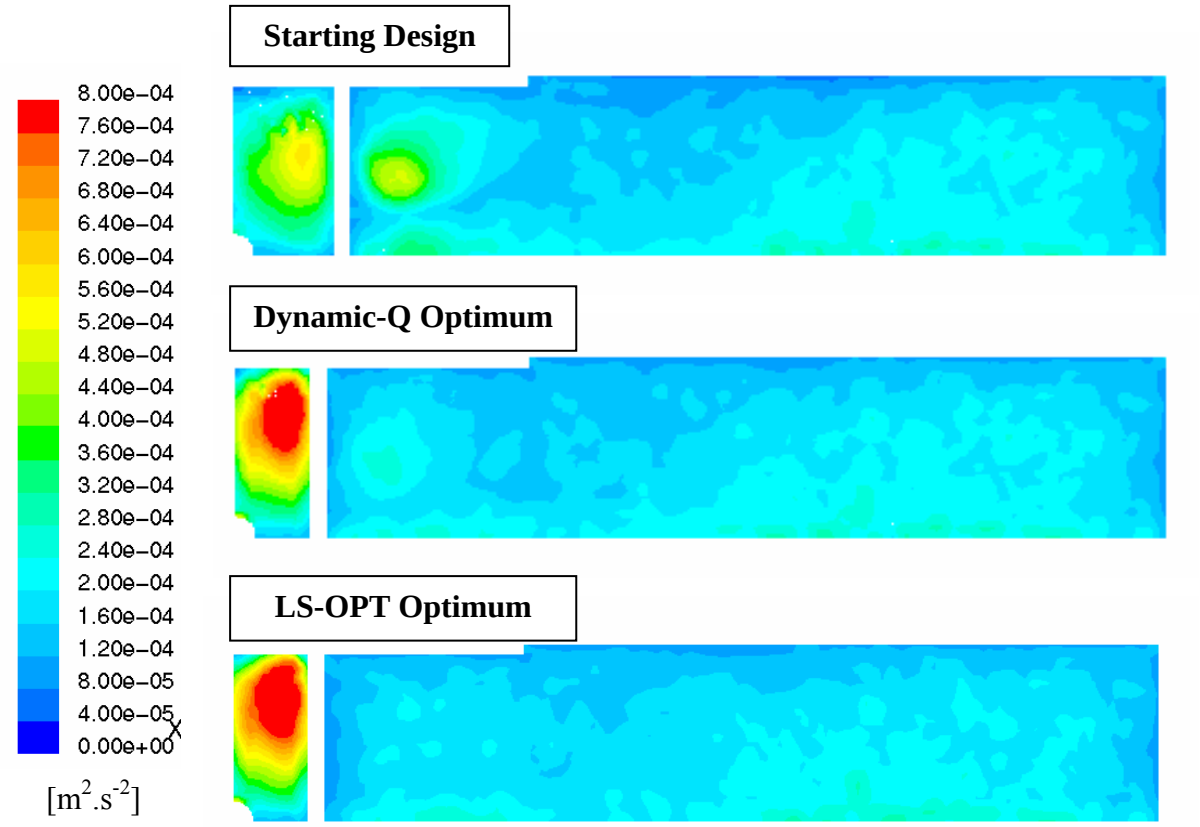

Figure 4-23: Comparison of turbulent kinetic energy on slag layer for the starting and final designs (DYNAMIC-Q and LS-OPT) (Case 2)

4-3.5 Conclusion

This section showed the second case study where a commercial CFD package was combined with mathematical optimisation techniques to give optimum designs of tundish geometry and tundish furniture. The objective function used in this case was the maximisation of the MRT at operating and a typical transition level. The MRT was used as an indication of the cleanliness of the steel. The pouring box area and the baffle geometry were chosen as design variables in this case. FLUENT with its pre-processor GAMBIT was easily incorporated into an automatic loop for the optimisation. The two optimisation techniques used in this case study proved to be robust and economical. A 138% and a 167% improvement in the operating level MRT were obtained using the DYNAMIC-Q method and the LS-OPT method respectively.

4-4 CASE STUDY 3: IMPACT PAD OPTIMISATION

The third case study is on a new impact pad design. Impact pads in tundishes have as their aim the reduction in the turbulence levels in the tundish. For this specific impact pad, the aim was to reduce the free-surface turbulence levels [74]. The design of the impact pad is also such that the flow is angled upwards toward the free-surface to improve the inclusion removal of the tundish. The impact pad is designed to be used in the single-strand stainless steel continuous caster in operation at the Middelburg plant of Columbus Stainless. This is the same tundish used in the first case study.

4-4.1 Parameterisation of Geometry

The impact pad geometry is shown Figure 4-24. The characteristics of the impact pad implies that it resorts under the Turbostop® [75] patent. The aim of the pad is to suppress turbulence through the creation of a recirculation zone within the pad through two overhead wings. As can be seen from the location of the impact pad in the tundish in Figure 4-25, the jet emanating from the shroud would impact the pad and then bend over on itself to flow towards the outlet. The pad has to suppress the turbulence of the jet so that it does not reach the surface above the pad with sufficient energy that could entrain slag. The lip on the pad has the function of angling the flow in the pouring box area upwards, much as a baffle with angled holes would do.

In order to optimise the impact pad, its geometry needs to be parameterised. The parameters chosen are shown in Figure 4-24. Initially, eight variables were chosen of which the values of two were fixed to the values shown in the figure. The value of w_1 is assumed to be the full width of the tundish (refer Figure 4-25), while the value of w_2 is such that the gap between the wings accommodates the possible motion of and uncertainty of the shroud position during casting. The three curvatures (d_1 through d_3) are parameterised as control points of Nonuniform Rational B-Splines (NURBS) used to define the geometry. A GAMBIT journal file that creates the impact pad given the of design variables and parameters is given in Appendix D.

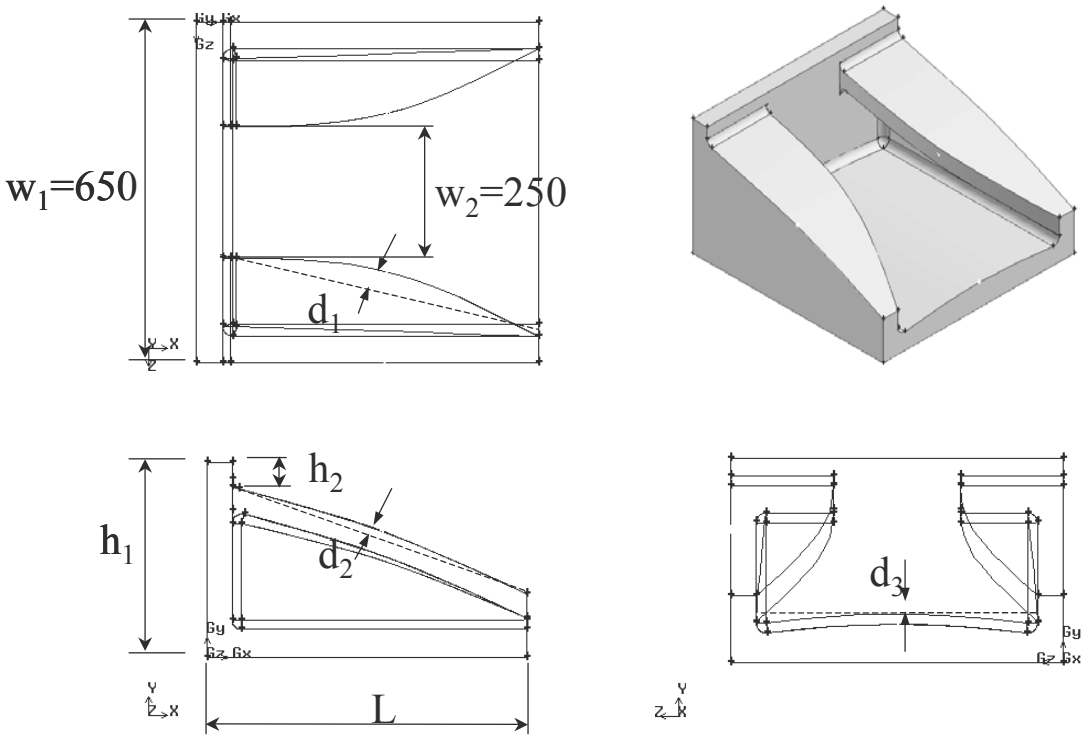

Figure 4-24: Schematic representation of impact pad with the design variables and fixed parameters (Case 3)

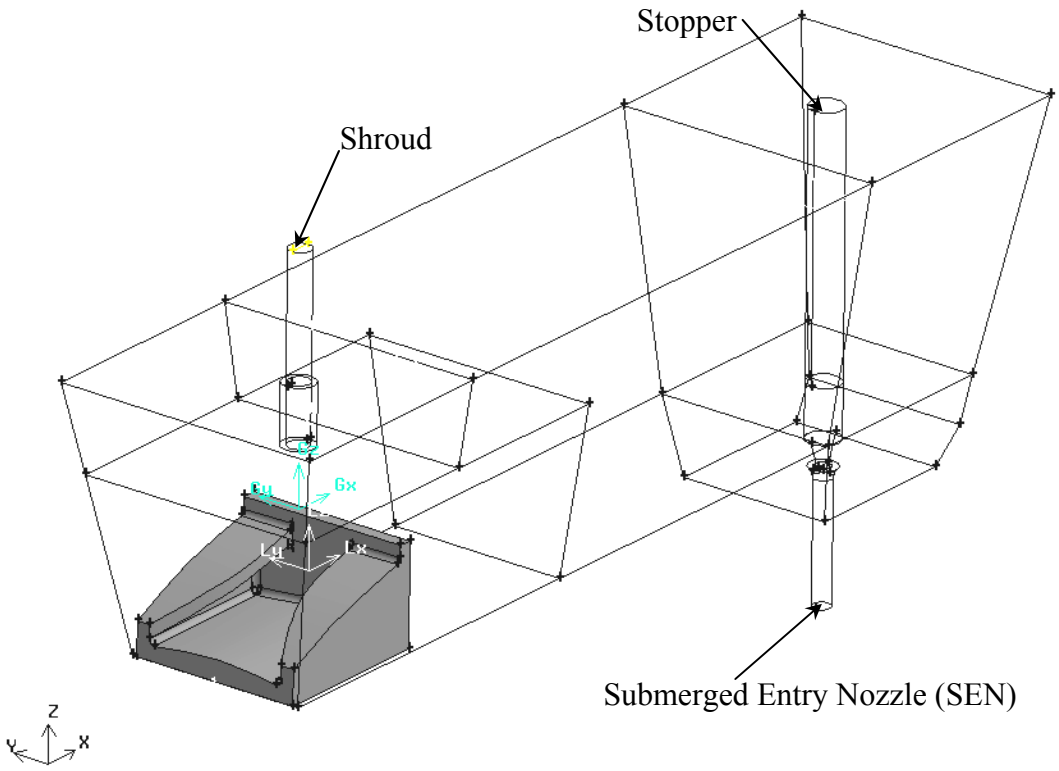

Figure 4-25: Graphical representation of impact pad inside tundish (Case 3)

4-4.2 Definition of Optimisation Problem

The complete mathematical formulation of the optimisation problem, in which the constraints are written in the standard form, $g(\boldsymbol{x}) \leq 0$, where $\boldsymbol{x}$ denotes the vector of the design variables $(x_1, x_2, x_3, x_4, x_5, x_6)^T = (L, h_1, h_2, d_1, d_2, d_3)^T$, is as follows:

$$\text{Minimize } \left[f(\boldsymbol{x}) = \max(\text{Turbulent kinetic energy on slag}) \right],$$

$$\text{subject to: } \begin{cases} g_j = -x_j + x_j^{\min} \leq 0; j = 1,2,3,...,6 \\ g_{j+6} = x_j - x_j^{\max} \leq 0; j = 1,2,3,...,6 \\ g_{13} = 200 - h_1 + h_2 \leq 0 \end{cases} \quad (4\text{-}4)$$

where $x_j^{\min}$ and $x_j^{\max}$ are suitable minimum and maximum constraints for the j^{th}-component of the design vector, $\boldsymbol{x}$. The upper and lower bounds on the variables are given in Table 4-9 together with the initial subregion size as required by the optimiser. The last constraint in (4-4) is to prevent the fluid volume below the impact pad wings from collapsing.

Table 4-9: Minimum, maximum and initial subregion of design variables (Case 3)

Variable	Minimum	Maximum	Initial subregion size
Length (L) [mm]	400	1200	600
Total height (h_1) [mm]	300	600	500
Lip height (h_2) [mm]	40	N/A	20
Wing curvature (d_1) [mm]	0	100	50
Side curvature (d_2) [mm]	0	100	20
Floor curvature (d_3) [mm]	0	40	10

4-4.3 CFD Modelling

Grid Generation and Model Set-up

A typical grid of the tundish is shown in Figure 4-26. The grids used in the optimisation contained in the order of 400 000 cells after grid adaption. It can

be seen in Figure 4-26 that most of the tundish contains hexahedral cells while the complex regions (i.e., around the impact pad and at the bottom of the stopper) contain tetrahedral cells. Due to the off-set of the shroud, the model had no symmetry that could be used to reduce the computation domain.

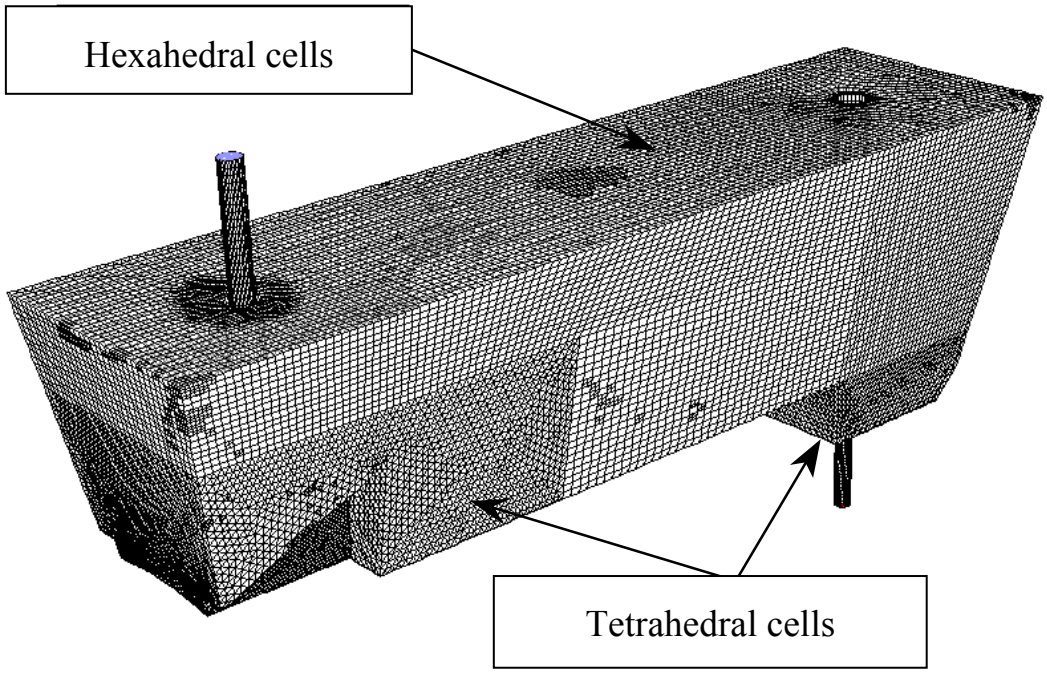

Figure 4-26: Typical grid of tundish with impact pad (Case 3)

Boundary Conditions and Fluid Properties

The boundary conditions used are shown in Figure 4-27. The heat fluxes were derived from on-site temperature measurements provided by Columbus Stainless. The fluid and thermal properties of the steel used are given in Table 4-10.

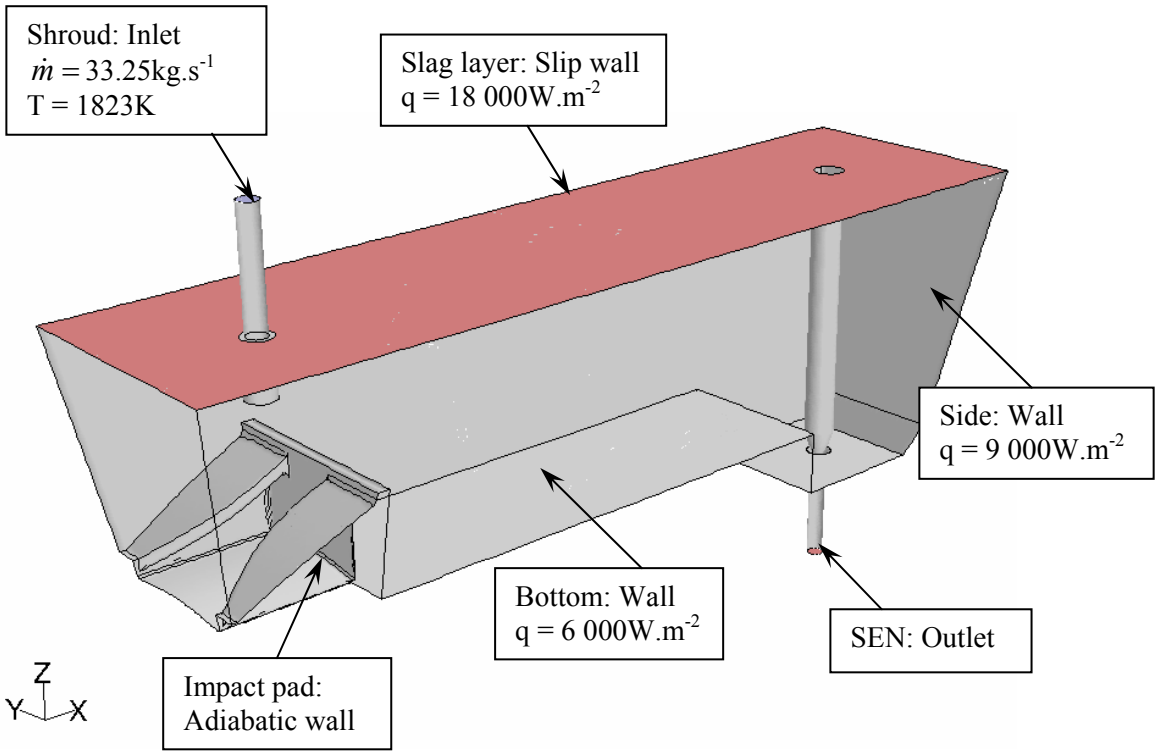

Figure 4-27: Boundary conditions (Case 3)

Table 4-10: Fluid and thermal properties of steel used for Case 3

Property	Value
Thermal expansion coefficient	0.1107×10^{-3}
Reference density [kg.m^{-3}]	6975
Reference temperature [K]	1773
Specific heat of liquid steel [J.kg^{-1}.K^{-1}]	817.3
Conductivity of liquid steel [W.m^{-1}.K^{-1}]	31.0
Dynamic viscosity of liquid steel [Pa.s]	0.0064

Computational Implementation and Run-Time

As mentioned above, the commercial CFD code, FLUENT is used in this case study. For the simulations presented in this case, the Reynolds-Averaged Navier-Stokes equations are solved with the k-ε turbulence model providing the turbulent closure. Second-order discretisation is used for all the flow equations while a three-order drop in the sum of the scaled residuals was considered to constitute a converged solution. The CFD model was run in parallel on three Pentium 4 1.7GHz machines operating under RedHat Linux

Version 7.2 . In this mode, each steady-state CFD simulation had a run-time of approximately 6 hours. Due to the 50% over-sampling used in the *D*-optimality implementation in LS-OPT, each optimisation iteration required $N = 11$ experimental designs or CFD simulations, implying 66 hours per optimisation iteration.

The set-up and solution procedure in FLUENT was automated by using a FLUENT journal file and is given in Appendix E. This journal file writes the appropriate files to the computer's hard disk. The Fortran programs given in Appendix F are used to extract the appropriate data from these files that is to be used by the optimiser.

4-4.4 Optimisation Results

The optimisation results presented here are firstly the optimisation history of the objective function defined in (4-4), and then the optimisation history of the six design variables, $\boldsymbol{x}$. In addition, some functions were monitored during the optimisation process. These include inclusion particle statistics, yield information and impact pad volume.

Objective Function

The optimisation history for the objective function defined in (4-4) is shown in Figure 4-28. The improvement obtained is not very significant (12.5% improvement compared to the starting design), mainly due to the fact that the chosen initial design had a fairly low TKE so start with.

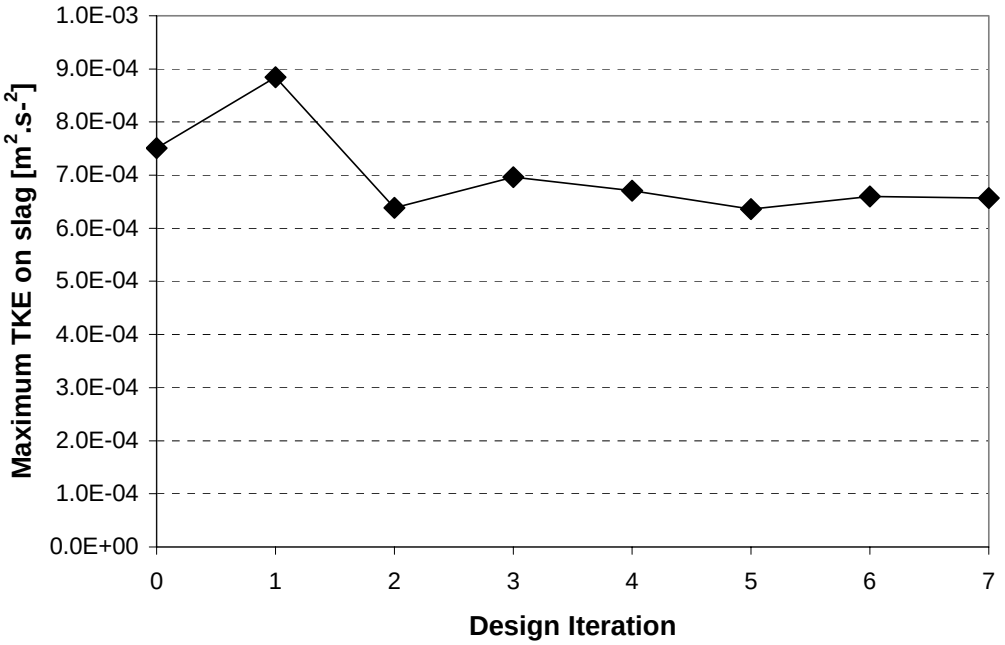

Figure 4-28: Optimisation history of objective function (Case 3)

As the objective function only represents the maximum TKE value on the slag surface, it is of interest to see how its reduction influences the distribution of TKE on the whole slag layer. This can be seen in Figure 4-29, where the TKE contours on the slag layer are shown for the different designs obtained during the optimisation history. All the contours range between 0 and 8e-4 $m^2.s^{-2}$. The surface TKE for the tundish with Turbostop® and baffle [76] is shown for comparison. It can be seen that that design had much higher TKE values than the current design. The higher TKE levels can be due to the fact that the Turbostop® is not optimised for the specific tundish configuration or the presence of the baffle. Note how the size of the maximum contour level in TKE is reduced by the optimiser for the current impact pad. Also shown in Figure 4-29, is design 3a that represents design iteration 3 where the values of the design variables were rounded to the nearest millimetre for manufacturing purposes.

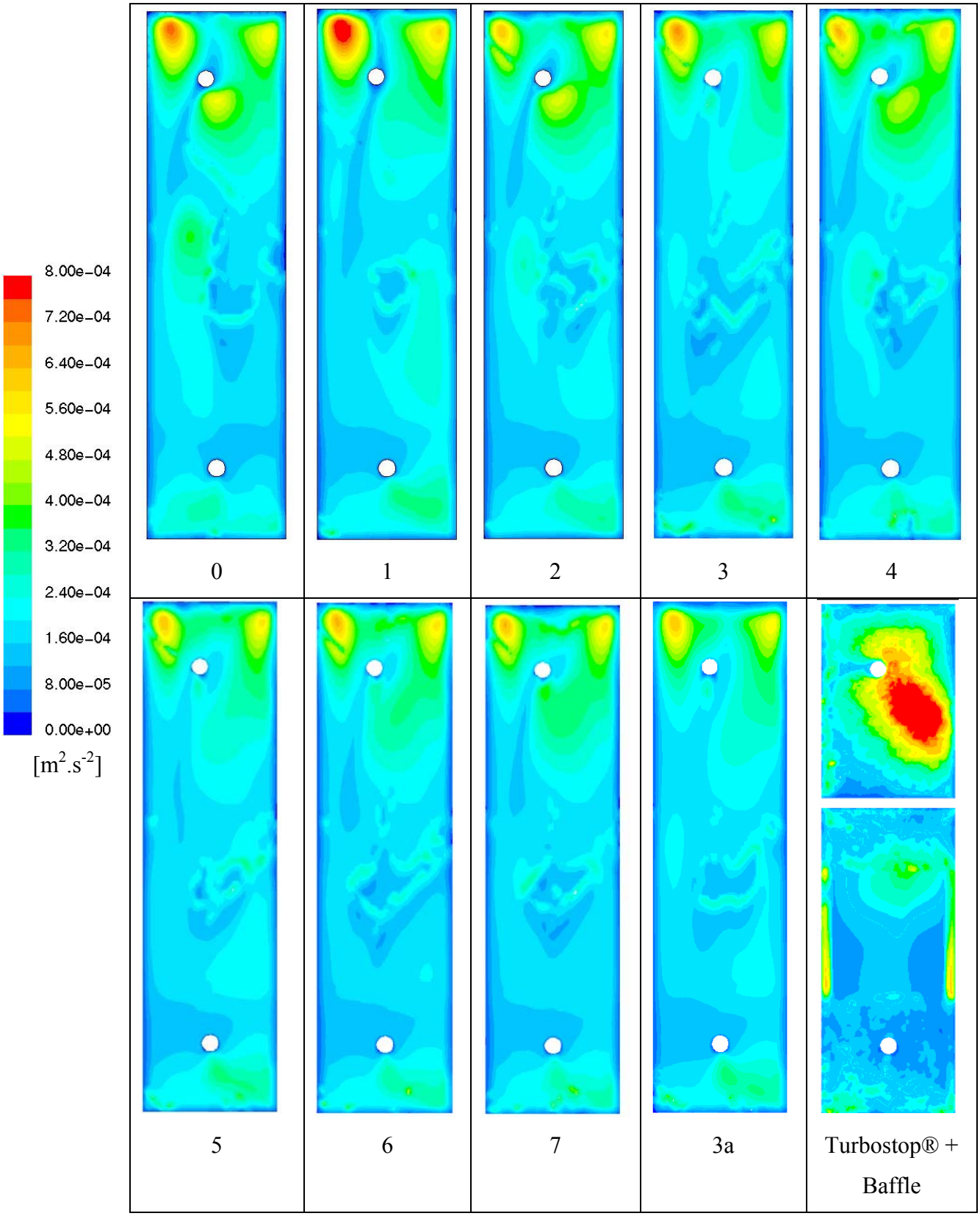

Figure 4-29: Turbulent kinetic energy on slag layer for different designs in optimisation history compared to the Turbostop™ and baffle configuration (Case 3)

Design Variables

The history of the design variables is shown in Figure 4-30. The two height variables exhibit the largest change during the optimisation. The physical influence of these variables on the geometry can be seen more clearly in Figure 4-31 where isometric views of the impact pads of which the TKE contours were shown in Figure 4-29, are displayed. The most notable difference in the optimum design from that of the baseline, is an overall reduction in height (h_1) with an increase in the lip height (h_2). Although the length of the impact pad (L) was not constrained, the optimiser did not attempt to increase its length. In fact, the length was reduced slightly. The maximum TKE proved relatively insensitive to the three curvatures (d_1, d_2, and d_3). Both the wing and floor curvatures increased slightly, while the side curvature remained constant.

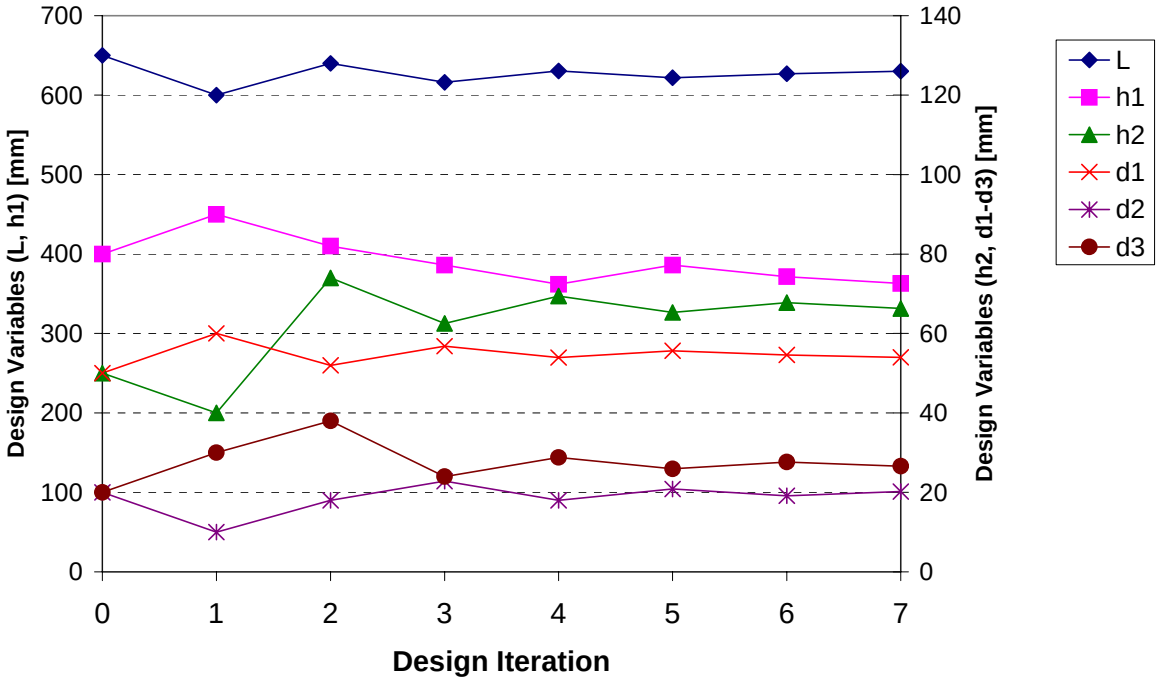

Figure 4-30: Optimisation history of design variables (Case 3)

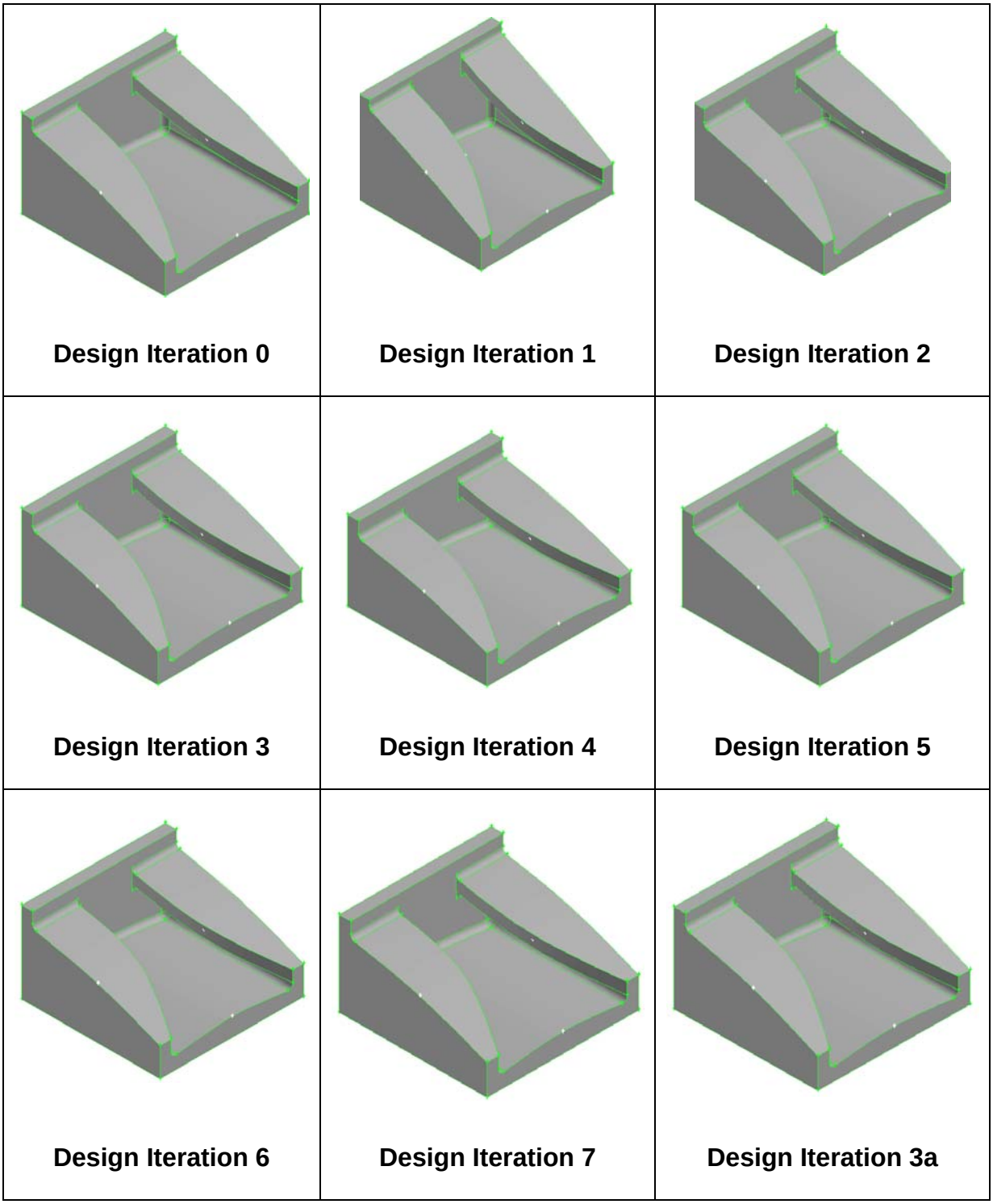

Figure 4-31: Optimisation history of design (Case 3)

Monitored Functions

Although not included in the design optimisation process, three other possible design criteria were monitored. Firstly, the inclusion particle removal capability due to the impact pad design was monitored. A typical size

distribution obtained from on-site sampling of the steel in the ladle (provided by Columbus Stainless), as shown in Figure 4-32, was introduced into the inlet to the tundish.

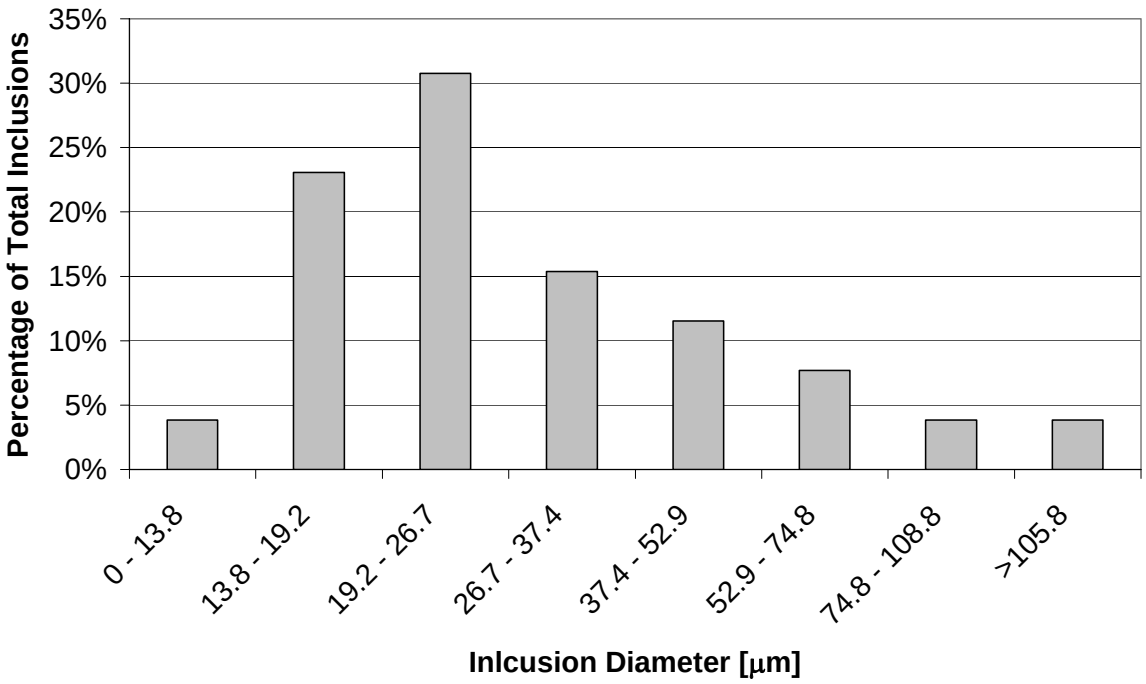

Figure 4-32: Size distribution of inclusion at inlet of tundish (Case 3)

Figure 4-33 shows the particle removal on the slag layer during the optimisation process using the Lagrangian tracking method explained in section 2-2.4.4 as available in FLUENT. Two methods for the particle tracking are investigated. The first is without the effects of the turbulence on the particle trajectory, indicated by the abbreviation *Lam* in brackets in Figure 4-33. The second is including the effect of turbulence using 100 stochastic tracks for each release point as explained in 2-2.4.4, indicated by the abbreviation *100RW* in brackets in Figure 4-33.

The removal efficiencies for the above two mentioned methods are shown for the larger particles as well as for all the particles size combined. Interestingly, note how the particle removal trend is initially opposite to that of turbulence suppression, but from the third iteration onwards, a reduction in turbulence

levels on the slag surface (as quantified by TKE) corresponds to fewer particles being trapped on the slag layer. The trapping of the four largest particle groups considered (all larger than 37μm) correlate with the trapping of all the particle sizes modelled.

The particle tracking without including the effect of turbulence on the particle trajectory is consistently lower than the case where turbulence is considered. This can be explained as follows. For the case without turbulence effects, the particles get close to the slag surface due to the nature of the flow in the tundish, but tend to travel along the surface without touching the surface as the buoyancy forces are too small to let the particles float to the top. For the case where turbulence is considered in the particle trajectory calculation, the particles also tend to get close to the slag surface but due to the nature of the stochastic tracking model, the particles are perturbed due to the effect of turbulence, causing them to touch the slag layer in more instances.

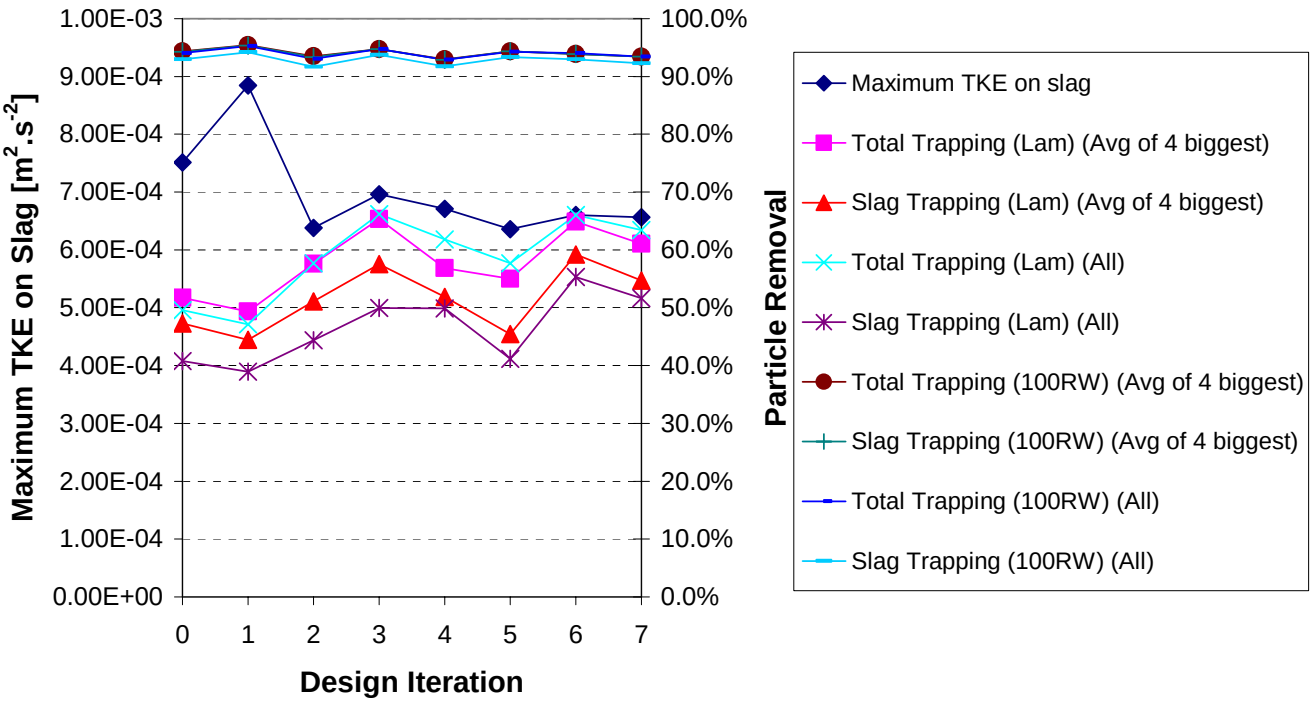

Figure 4-33: Optimisation history of monitoring functions (particle removal) (Case 3)

The second and third functions that were monitored to assist in the evaluation of the design are the impact pad volume (as a measure of its cost and weight for handling purposes) and the volume of steel remaining in the tundish behind the impact pad after draining. These two functions are given in Figure 4-34 together with the objective function. Although not expected because these functions were not explicitly used in the optimisation formulation, both these quantities were reduced as the objective was minimised.

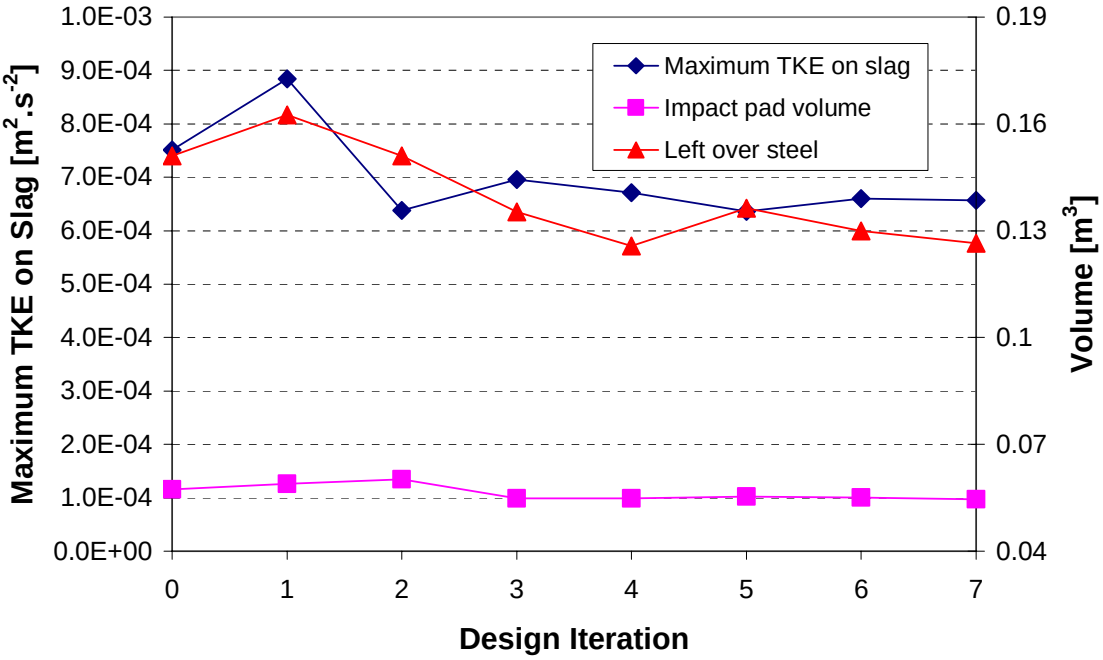

Figure 4-34: Optimisation history of monitoring functions (volumes) (Case 3)

The numerical values of the objective and monitored functions are given in Table 4-11 for direct comparison. Again design 3a represents design iteration 3 where the values of the design variables were rounded to the nearest millimetre for manufacturing purposes. The details are discussed in 4-4.5 below.

Table 4-11: Optimisation history of objective and selected monitoring functions (Case 3)

Iteration	Maximum k on slag [$m^2.s^{-2}$]	Total trapping percentage (Laminar) Avg of 4 largest)	Total trapping percentage (100RW) Avg of 4 largest)	Volume steel left over [m^3]	Impact pad volume [m^3]
0	0.000751	47.25%	94.25%	0.15098	0.05734
1	0.000884	44.42%	95.35%	0.16255	0.05888
2	0.000638	51.09%	93.36%	0.15100	0.06020
3	0.000696	57.55%	94.71%	0.13530	0.05476
4	0.000671	51.89%	92.86%	0.12576	0.05481
5	0.000636	45.41%	94.30%	0.13638	0.05538
6	0.000660	59.20%	93.84%	0.13001	0.05503
7	0.000657	54.72%	93.39%	0.12647	0.05458
3a	0.000640	55.25%	94.88%	0.13464	0.05457

4-4.5 Chosen design

In an attempt to present a compromised design, the design in iteration 3 was chosen for manufacture. This is because its maximum TKE is reasonable, but more importantly it had the highest particle removal rate of the first five designs (those available when the design was frozen). The variables describing the geometry of Iteration 3 were rounded to values as would be required for the manufacture of the impact pad. The performance parameters (TKE and particle removal statistics) for this design were included in the results above (See 3a in Figure 4-29 and Figure 4-31). As can be seen in Table 4-11, the modified design 3a outperforms design 3, in that it has a lower maximum TKE, and similar particle removal. The values of the rounded variables are given in Table 4-12.

Table 4-12: Rounded variable values – Design 3a (Case 3)

Variable	Value
Length (L) [mm]	615.0
Total height (h_1) [mm]	385.0
Lip height (h_2) [mm]	60.0
Wing curvature (d_1) [mm]	56.0
Side curvature (d_2) [mm]	20.0
Floor curvature (d_3) [mm]	24.0

4-4.5.1 Flow Results of Chosen Design

In addition to the optimisation results of design 3a given above, Residence Time Distribution (RTD) results are given in this section. Detailed steady flow results are given in Appendix G. These results are to serve as comparison to that of other previous and future designs as well as with water model results.

RTD data of chosen design

A transient simulation of the chosen was performed. This simulation took the form of monitoring the outlet concentration for a step input of tracer at the inlet. The resulting distribution was differentiated numerically to obtain the familiar RTD curve. The typical RTD related quantities were calculated and are given in Table 4-13. The values obtained with this impact pad are again compared to that of the Turbostop® and baffle configuration calculated in a previous study [76]. The dead volume in the tundish has increased to nearly 40% compared to the 26% of the original Turbostop® and baffle (also in Table 4-13). This result emphasises the need for a well-designed dam near the outlet to not only prevent short-circuiting, but to also reduce the dead zones in the tundish.

Table 4-13: RTD-related data (Case 3)

Quantity	Impact pad	Turbostop® + baffle [76]
Theoretical Mean Residence Time, $\bar{t}$	679.9 s	669.8 s
Tundish volume	3.241 m^3	3.193 m^3
Dispersed Plug Flow Volume	19.4%	23.6 %
Mixed Flow Volume	41.1%	50.4 %
Dead Volume	39.5%	25.9 %
Minimum Residence Time (MRT)	0.170	0.192
Peak Residence Time (PRT)	0.216	0.281
Actual mean residence time (θ_{mean})	0.605	0.741

4-4.6 Water Model and Plant Implementation

The optimised impact pad was manufactured and tested in the tundish water model at the University of Pretoria [77]. Visual observations of the water model were made with respect to surface appearance and dye flow patterns as detailed in the technical note [78]. A summary of the observations of water model with the impact pad as compared to an empty tundish is given in Table 4-14.

Table 4-14: Visual observation of surface and dye flow patterns [78]

Configuration	Visual observation
New impact pad design	Quiet surface appearance around inlet stream Slight movement visible along the back wall (wall furthest from outlet) area No stagnant zones visible
Empty tundish	Quiet surface appearance Short circuiting of dye to outlet stream No stagnant zones visible.

The optimised impact pad was also manufactured for plant trials at Columbus Stainless, where it underwent extensive plant trials [79,80]. The initial trials

[79] indicated that the 304 stainless steel grade showed a reduction in defects with the new impact pad compared to the case without any furniture. The 409 stainless steel grade however showed an increase in the number of defects when using the new impact pad compared to Columbus Stainless' current furniture. The results from the initial trial motivated a long-term trial for the new impact pad [80]. The long-term trial indicated that the impact pad decreased the defects in the austenitic material (e.g., 304, 316), while increasing the defects in the ferritic material (e.g, 409). From this, it was recommended that the new impact pad should be implemented on a long-term basis on the 304 steel grade. The difference in performance for the ferritic and austenitic material in the plant trials highlighted the current challenge for CFD to model the detailed metallurgical reactions that occur in different steel grades (e.g., inclusion formation and the interaction with the slag layer) to explain why there is difference in the impact pad performance of these two grades.

4-4.7 Conclusions

This section described the optimisation of an impact pad for the single-strand tundish of Columbus Stainless. The techniques of CFD coupled with mathematical optimisation were used in the form of the commercial solver FLUENT, its pre-processor GAMBIT and the commercial optimiser, LS-OPT. The objective function used was the maximum turbulent kinetic energy on the slag surface. Six design variables describing the impact pad geometry were used. A 12.5% reduction in maximum surface turbulent kinetic energy was obtained during the optimisation. During the optimisation process, the inclusion particle removal capability of the design was monitored as well as impact pad volume and liquid steel yield.

4-5 CASE STUDY 4: DAM OPTIMISATION WITH IMPACT PAD

In the last test case, a dam was introduced in the tundish combined with the previously optimised impact pad. This introduction of the dam was an attempt to deflect the flow upwards in order to remove inclusions by trapping them on the slag layer without affecting the turbulence suppressing capability of the tundish with impact pad.

4-5.1 Parameterisation of Geometry

The chosen design (design 3a) of the impact pad of Case Study 3 was kept fixed, while the dam introduced two additional variables, i.e., the height of the dam (p_1), and the position of the dam from the left corner of the tundish (h_3), as shown in Figure 4-35.

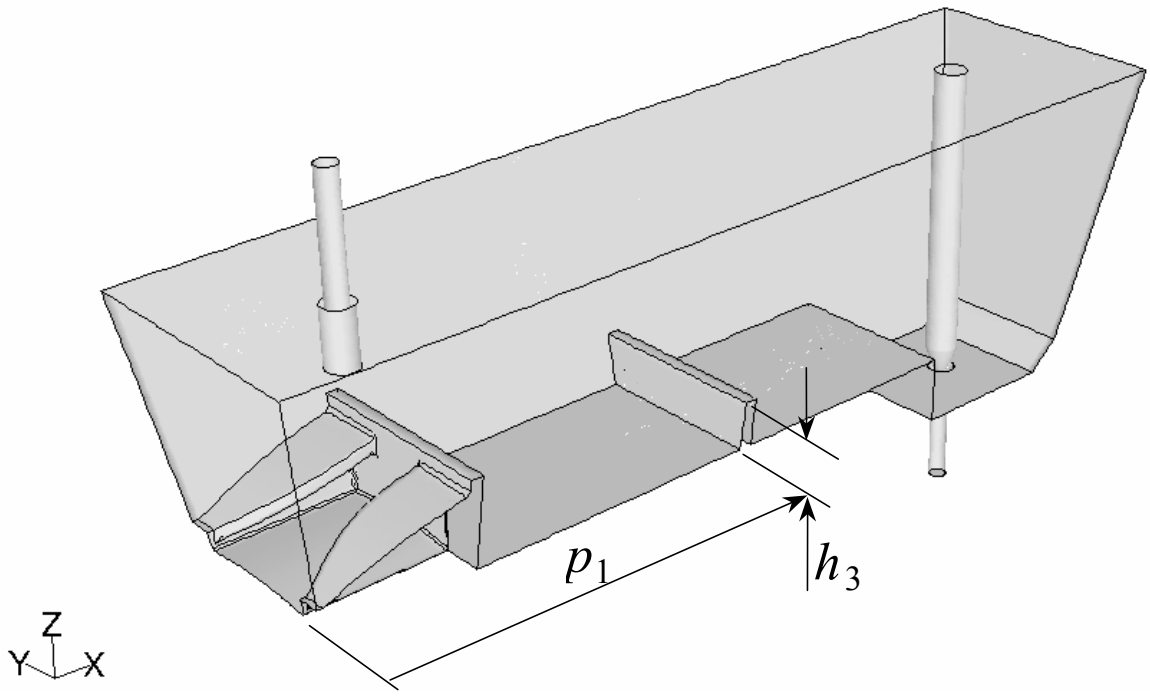

Figure 4-35: Design variables of dam (Case 4)

4-5.2 Definition of Optimisation Problem

In this case study, the inclusion removal on the slag layer was maximised. The inclusion particles were assumed to be trapped by the slag layer when they came in contact with the slag layer. The definition of the optimisation problem in the standard form is given in equation (4-5) where $\boldsymbol{x}$ denotes the vector of design variables $(x_1, x_2)^T = (p_1, h_3)^T$.

$$\text{Maximise } [f(\boldsymbol{x}) = \text{Particle Trapping}(\boldsymbol{x})]$$

$$\text{subject to: } \begin{cases} g_j = -x_j + x_j^{\min} \le 0; j = 1,2 \\ g_{j+2} = x_j - x_j^{\max} \le 0; j = 1,2 \end{cases} \quad (4\text{-}5)$$

The minimum and maximum allowable values for the optimisation problem are given in Table 4-15 together with the initial subregion size required by LS-OPT. The minimum and maximum values were chosen purely from a geometrical constraint, i.e., the values were chosen so that the dam would fit into the tundish and that there is space between the top of the dam and the slag layer to allow the steel to flow over the dam.

Table 4-15: Minimum, maximum and initial subregion of design variables (Case 4)

Variable	Minimum	Maximum	Initial subregion size
Position of dam (p_1) [mm]	1500	2700	1000
Height of dam (h_3) [mm]	50	750	400

4-5.3 Inclusion Particle Modelling Approach

In this case study the Lagrangian particle tracking method, as described in section 2-2.4.4, is used. The effect of turbulence on the inclusion removal is included by using the stochastic tracking method discussed in the same section. 100 stochastic tracks for each injection point are used and the same inclusion size distribution as in the third case study is used as given in Figure 4-32.

Particles touching the sides and bottom of the tundish and the tundish furniture are assumed to be reflected back into the molten steel flow.

4-5.4 Optimisation Results

Objective function and monitoring function

The history of the objective and monitored function is given in Figure 4-36. As shown, the particle removal increased from just under 95% removal to above 97% removal by the slag layer. Although the maximum turbulent kinetic energy on the slag layer did not form part of the optimisation problem, it was monitored to see what the effect of the introduction of the dam would have on the turbulence of the slag surface. In this case, the maximum turbulent kinetic energy proved to be insensitive to the introduction of the dam and the optimised case even had a slightly lower value. This can be explained by the fact that the maximum values on the slag surface occur close to the shroud and the dam does not introduce higher levels of turbulence in the slow-moving liquid in the area of the dam.

If it were found that the turbulent kinetic energy was higher than the starting design, it could explicitly form part of the optimisation through the introduction of a constraint function limiting the maximum turbulent kinetic energy on the slag layer to be below the value of the case without a dam.

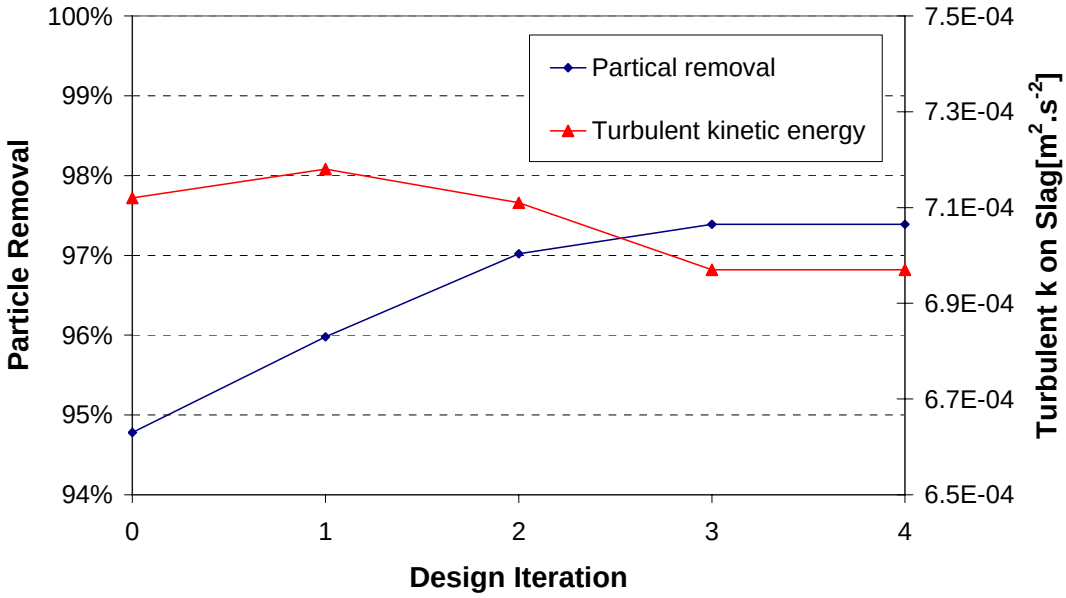

Figure 4-36: Optimisation history of objective function (Case 4)

Design Variables

The history of the design variables is shown in Figure 4-37. As can be seen in this figure, the optimum dam configuration for particle removal is the highest allowable dam as close to the shroud as allowed. The result makes intuitive sense as the flow is deflected upwards and the chance of a particle reaching the slag layer is improved. This optimum design is however impractical looking at it from a yield prospective unless draining holes are inserted into the dam. This shows how important the initial formulation of the optimisation problem is. The yield can also form part of the optimisation problem as a constraint and then the optimiser will find an optimum within the prescribed yield limit.

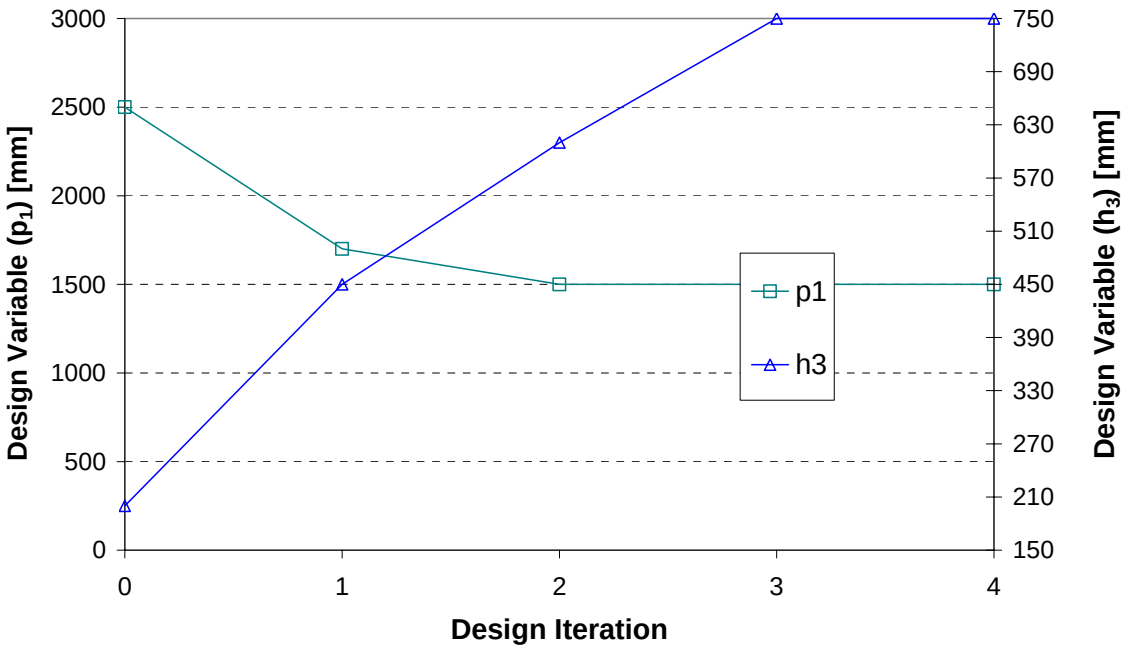

Figure 4-37: Optimisation history of design variables (Case 4)

4-5.5 Flow Results

An important aspect of introducing a dam, is that the dam should not increase the surface turbulent kinetic energy. The turbulent kinetic energy for the case without the dam, with the initial design dam, and the optimised dam are shown in Figure 4-38. The higher turbulence levels that are introduced by the dam can be seen by the higher (more green) contours present in the centre of the slag layer shown in Figure 4-38c). These higher turbulence levels are still lower than the maximum values that occur near the shroud.

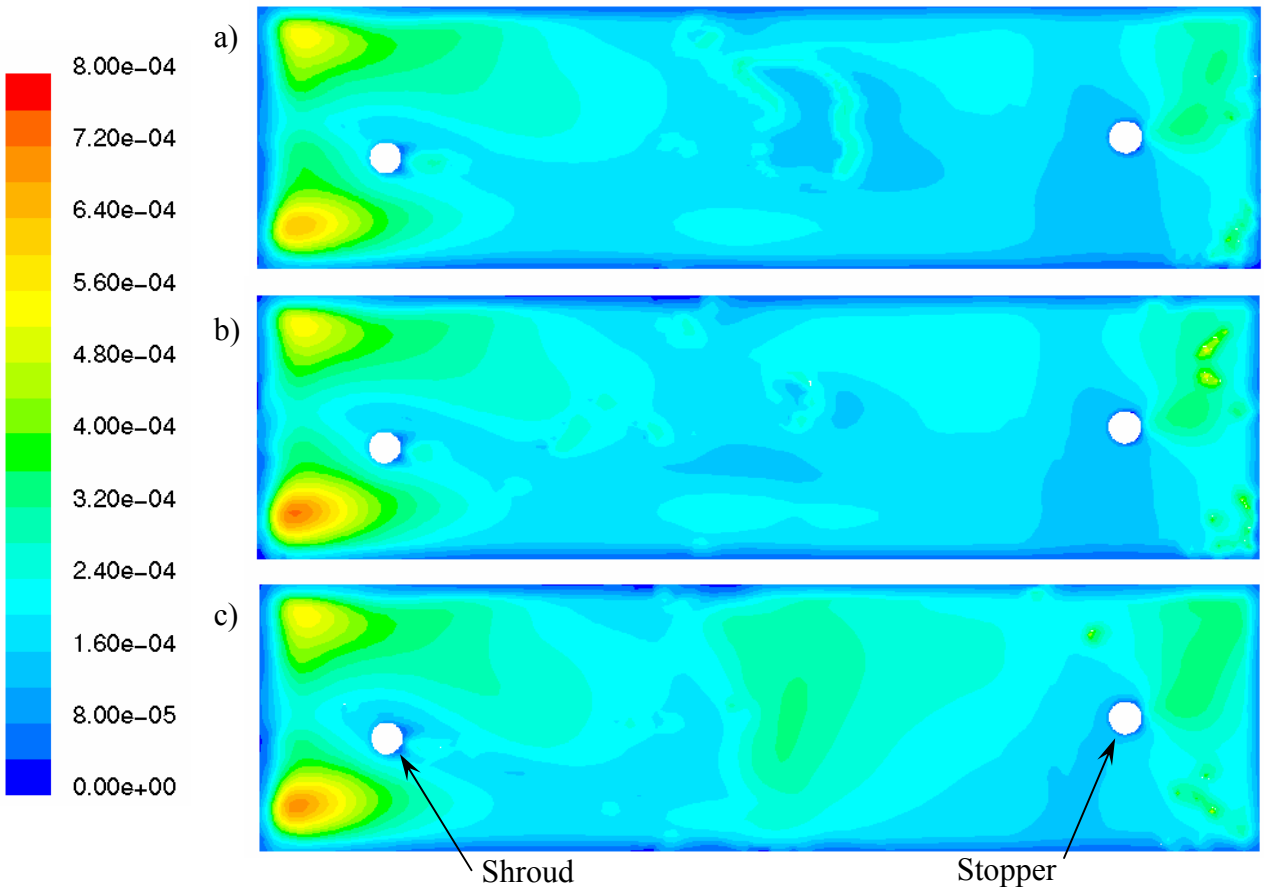

Figure 4-38: Turbulent kinetic energy without dam (a) and with initial dam (b) and with optimised dam (c) (Case 4)

4-5.6 Conclusion

A dam was used in conjunction with the optimised impact pad of case study 3. The position and height of the dam were optimised to give the maximum inclusion removal from the steel by the slag layer. Monitoring the turbulent kinetic on the slag layer showed that the maximum turbulent kinetic did not increase from the optimum of case study 3. The optimum dam position was as close to the shroud as possible with the highest allowable height. Although this configuration is good for inclusion removal, it is very bad from a yield perspective unless draining holes are added. This showed the importance of the correct formulation of the optimisation problem. If a value like yield does not form part of the optimisation formulation, the optimiser ignores these values and undesirable optimum designs can be obtained.

4-6 CONCLUSION

This chapter applied the methodology developed in Chapter 3 to different test cases. The first case optimised the position of a dam and a weir of a single-strand tundish. Two optimisation formulations were considered in this case, the first was the minimisation of the dead volume in the tundish and the second the maximisation of the inclusion removal of the tundish. Two different optima were obtained for the two different formulations, highlighting the importance of the correct formulation of the optimisation problem.

The second case optimised the baffle and pouring box area of a two-strand continuous caster. In this case, the minimum residence time was maximised by changing the geometry of the pouring box and baffle area. In this optimisation formulation a weighted value of the minimum residence time at the operating condition and that of the minimum residence time at a transition level were used. Significant improvements, in excess of 130%, were made to the design compared to the starting design.

The third case investigated the design of a new impact pad. An impact pad in a tundish has as its aim the reduction of turbulence in the tundish. For this reason the surface turbulent kinetic energy was minimised by changing the geometry of the impact pad.

The inclusion removal capabilities of the impact pad on its own, as optimised in the third test case, are not very good. The last case optimised a dam height and position in conjunction with the previously designed impact pad. The dam improved the particle removal capabilities of the tundish without increasing the turbulent kinetic energy on the free surface, but the suggested design seems to be impractical. This again highlights the importance of the correct formulation of the optimisation problem.

5

CHAPTER 5: CONCLUSION

The continuous casting process is not a very old manufacturing process, but in the last four decades, it became the most common process for producing most basic metals. One of the particular important components in this system is the tundish. Traditionally, the tundish acted as a reservoir between the ladle and the mould but more recently it has been used a grade separator, an inclusion removal device and a metallurgical reactor. A continuous drive to understand the molten metal flow patterns inside the tundish has led to many research papers being published in the modelling of the flow patterns, through either water modelling or numerical modelling. Included in these papers, researchers changed the design of the tundish by adding tundish furniture or changing the dimensions of the tundish. They showed that these changes can improve the flow patterns that ultimately improve the performance of the tundish. These changes were however based on trial-and-error experimentation or relied on the experience of the modeller to propose the design changes. This type of design methodology can lead to non-optimal solutions.

In this thesis, a methodology has been developed to optimise the molten steel flow patterns in a tundish by changing the tundish and tundish furniture. The methodology makes use of mathematical optimisation and Computational Fluid Dynamics (CFD) to give an optimum tundish and tundish furniture design based on certain design criteria as specified by the engineer. A literature survey that describes CFD modelling of a tundish and the optimisation algorithms used in this work were presented in Chapter 2.

The proposed methodology (as outlined in Chapter 3) consists of a number of steps. The first step is the validation the numerical (CFD) mode. This can be achieved by

either comparing the numerical results to a water model or to a plant trial. The second and most important step is the formulation of the optimisation problem. This step involves deciding on the design variables, objective function and constraint function(s). The last step before running the optimisation involves the automisation of the optimisation process. This involves the creation of appropriate files and scripts so that the CFD model can be created, solved and data extracted for a specific set of design variables without user intervention.

The methodology developed in the thesis was tested on four cases as described in Chapter 4. The first case optimised a simple dam-weir configuration for the lowest dead volume and for high inclusion removal on the slag layer. The second case optimised the baffle and pouring-box area in order to maximise the minimum residence time. In the third case, the methodology was used to design a new impact pad to reduce the slag layer turbulence. The newly designed impact pad was built and tested in the full-scale water model at the University of Pretoria. The new impact pad has also undergone trials in the single-strand continuous caster of Columbus Stainless Steel. The fourth and last case, described the optimisation of the position and height if a dam to be used with the impact pad developed in the third case, in order to increase the trapping of inclusion by the slag layer.

The methodology proved to work extremely well in all cases. The results show good improvements in the performance of the tundishes under investigation. From this, it is concluded that this methodology provides an improved alternative over the traditional design methods of developing and redesigning tundish and tundish furniture.

An important aspect that was highlighted by the study is that the correct formulation of the optimisation problem is crucial for the success of the optimisation procedure. This correct formulation is reliant on the understanding and skill of the design engineer. The resulting optimum is sensitive to the formulation of the optimisation problem.

One drawback of this methodology is the computational time that the optimisation procedure takes. This time can be reduced by using multiple computers to run the

simulations in parallel. The continued growth of computer power is leading to a reduction in the required optimisation time, but at the same time allowing more detailed CFD model to be constructed. This drawback is however offset by the fact that an optimum design is obtained which would not be possible or highly unlikely using traditional experimental modelling (water modelling or plant trials) or trial-and-error numerical modelling.

The methodology developed can now be applied in general to other tundishes with other tundish furniture, providing that the design engineer formulates the optimisation problem correctly.

6

CHAPTER 6: RECOMMENDATIONS AND FUTURE WORK

A number of new areas that can follow on this current research have been identified and are given below.

6-1 APPLICATION OF METHODOLOGY TO OTHER ELEMENTS OF THE CONTINUOUS CASTING PROCESS

The optimisation methodology developed in this study should be applied to the Submerged Entry Nozzle (SEN), mould design and other components downstream of the tundish in the continuous casting process. It is important to have favourable flow patterns in the mould as poor flow patterns can result in slag entrainment that will render all the improvements made in the tundish useless. If electromagnetic stirring is used in the mould, the operating parameters of the stirrer could be optimised.

The optimisation methodology should also be applied to components upstream of the tundish, e.g., the ladle. This could include the optimum design of gas sparging in the ladle to reduce temperature stratification, or the design of the refractory to minimise the heat losses from the ladle.

6-2 TRANSIENT COMPUTATIONAL FLUID DYNAMICS MODEL

The cases in the thesis were all steady state. As the actual tundish and ladle operation involves transient periods as well, especially during mixed grade transition, the optimisation of the transient performance can also be treated with this methodology as computing power allows.

The cascading that corresponds to high oxidation of the steel also occurs during the initial filling (first heat) of the tundish. This transient filling phenomenon and design of the furniture to reduce this effect can also be treated with this methodology.

6-3 TESTING OF OPTIMISATION FORMULATIONS

Additional tundish and tundish furniture designs can be optimised and the methodology can be tested on some of the other optimisation formulations given in Chapter 3. Some of the optimisation formulations at the time of this study were computationally too expensive, but with the rapid growth in computational power, these formulations could soon be investigated.

6-4 EXTENSION AND VALIDATION OF INCLUSION MODELLING

Validation of the inclusion modelling should be undertaken to validate the accuracy of the models when using stochastic tracking. There remains some uncertainty as to the accuracy of the CFD model of the small inclusions in a turbulent flow field.

A model should also be developed to include the detailed chemistry of the inclusions in the CFD analysis. This model should include aspects such as inclusion generation, amalgamation, and reaction with the slag layer. In this study, a particle touching the free surface was assumed to be trapped which is not the case in a physical tundish. A first attempt was made to improve the modelling of the capturing of a particle on the slag surface. For this purpose, a FLUENT User Defined Function was developed and is given in Appendix H. This first attempt is a simple model and calculates the maximum continuous time that a particle spends in a user-defined region close to the slag layer. A correlation is then used that relates the probability of a particle being trapped, to the size of the particle and the time it spent near the slag layer. Other possible correlations should also be investigated and the detailed reaction of the particle on the slag surface can be included. One of the anticipated difficulties for this future work is to get quantative data from the plant operations to validate the numerical model.

The erosion of the tundish furniture is a further source of inclusions. A model describing the erosion rate of the furniture and the corresponding size and chemical composition of the inclusions that are introduced into the steel should be developed. The movement of these inclusions and interaction with the slag layer should then be modelled in a similar manner as described in the paragraph above.

REFERENCES

[1] Thomas, BG, 'Continuous Casting', The Encyclopedia of Materials: Science and Technology, K.H. J. Buschow, R. Cahn, M. Flemings, B. Ilschner, E. J. Kramer, S. Mahajan.(D. Apelian, subject ed.) Elsevier Science Ltd., Oxford, United Kingdom, Vol. 2, pp. 1595-1599, 2001.

[2] Wolf MM, 'History of Continuous Casting', *Steelmaking Conference Proceedings*, Iron & Steel Society, Warrendale, PA, pp. 83-137, 1992.

[3] Thomas BG, 'Introduction to Continuous Casting', Continuous Casting Consortium, URL: *http://bgtibm1.me.uiuc.edu*, 1999.

[4] Thomas BG, 'Continuous Casting of Steel', Chapter 15 in Modeling for Casting and Solidification Processing, O. Yu, editor, Marcel,Dekker, New York, NY, pp. 499-540, 2001.

[5] Mazumdar D, Yamanoglu G, Shankarnarayanan R, Guthrie RIL, 'Similarity Considerations in the Physical Modelling of Steel Making Tundish Systems', *Steel Research*, Vol. 66, No. 1, 14-19, 1995.

[6] Sahai Y, Ahuja R, 'Fluid Flow and Mixing of Melt in Steelmaking Tundishes', *Ironmaking & Steelmaking*, Vol. 13, No. 5, pp. 241-247, 1986.

[7] López-Ramirez S, De J Barreto J, Palafox-Ramos J, Morales RD, Zacharias D, 'Modeling Study of the Influence of Turbulence Inhibitors on the Molten Steel Flow, Tracer Dispersion, and Inclusion Trajectoris in Tundishes', *Metallurgical and Materials Transactions B,* Vol. 32B, pp. 615-627, 2001.

[8] Koria SC, Singh S, 'Physical Modeling of the Effects of the Flow Modifier on the Dynamics of Molten Steel Flowing in a Tundish', *Iron and Steel Institute of Japan Int.*, Vol. 34, No. 10, pp. 784-793, 1994.

[9] Sheng DY, Jonsson L, 'Investigation of Transient Fluid-Flow and Heat-Transfer in a Continuous-Casting Tundish by Numerical-Analysis Verified with Nonisothermal Water Model Experiments', *Metallurgical and Materials Transactions B,* Vol. 30B, No. 5, pp. 979-985, 1999.

[10] Sinha AK, Vassilicos A, 'Physical Modelling of Thermal Effects on Steel Flow and Mixing in Tundish', *Ironmaking & Steelmaking,* Vol. 25, No. 5, pp. 387-393, 1998.

[11] He Y, Sahai Y, 'The Effect of Tundish Wall Inclination on the Fluid Flow and Mixing: A Modeling Study', *Metallurgical Transactions B*, Vol. 18, pp. 81-92, 1987.

[12] Joo S, Han JW, Guthrie RIL, 'Inclusion Behavior and Heat-Transfer Phenomena in Steelmaking Tundish Operations', *Metallurgical and Materials Transactions B*, Vol. 24B, pp. 767-777, 1993.

[13] Chakraborty S, Sahai Y,' Mathematical Modelling of Transport Phenomena in Continuous Casting Tundishes' *Ironmaking & Steelmaking*, Vol. 19, (6), pp. 479, 1992.

[14] Sahai Y, Ahuja R, 'Fluid Flow and Mixing of Melt in Steelmaking tundishes', *Ironmaking & Steelmaking*, Vol. 13, No. 5, pp. 241-247, 1986.

[15] Kemeny F, Harris DJ, McLean A, Meadowcroft TR, Young JD, 'Fluid Flow Studies in the Tundish of a Slab Caster', *Proceedings of the 2nd Process Technology Conf.,* Warrendale, PA, 1981.

[16] Mazumdar D, Guthrie RIL, 'The Physical and Mathematical Modelling of Continuous Casting Tundish Systems', *Iron and Steel Institute of Japan Int.,* Vol. 39, No. 6, pp. 524-547, 1999.

[17] Sahai Y, Burval M, 'Validity of Reynolds and Froude similarity criteria for water modeling of melt flow in tundishes', *Proc. Electric Furnace Conference*, ISS-AIME, Vol. 50, pp.469-474, 1992.

[18] Morales RD, Lopez-Ramirez S, Palafox-Ramos J, Zacharias D, 'Numerical and Modeling Analysis of Fluid Flow and Heat Transfer of Liquid Steel in a Tundish with Different Flow Control Devices', *Iron and Steel Institute of Japan Int.,* Vol. 39, No. 5, pp. 455-462, 1999.

[19] López-Ramirez S, De J Barreto J, Palafox-Ramos J, Morales RD, Zacharias D, 'Modeling Study of the Influence of Turbulence Inhibitors on the Molten Steel Flow, Tracer Dispersion, and Inclusion Trajectories in Tundishes', *Metallurgical and Materials Transactions B,* Vol. 32B, pp. 615-627, 2001.

[20] Koria SC, Singh S, 'Physical Modeling of the Effects of the Flow Modifier on the Dynamics of Molten Steel Flowing in a Tundish', *Iron and Steel Institute of Japan Int.*, Vol. 34, No. 10, pp. 784-793, 1994.

[21] Sheng DY, Jonsson L, 'Investigation of Transient Fluid-Flow and Heat-Transfer in a Continuous-Casting Tundish by Numerical-Analysis Verified with Nonisothermal Water Model Experiments', *Metallurgical and Materials Transactions B,* Vol. 30B, No. 5, pp. 979-985, 1999.

[22] Lievenspiel O, *Chemical Reaction Engineering – An Introduction to the Design of Chemical Rectors*, John Wiley and Sons Inc., New York, 1967.

[23] Singh S, Koria SC, 'Model Study of the Dynamics of Flow of Steel Melt in the Tundish', *Iron and Steel Institute of Japan Int.*, Vol. 33, No. 12, pp. 1228-1237, 1993

[24] Nakajima H, Sebo F, Tanaka S, Dumitru I, Harris DJ Guthrie RIL, *Proc. of the 2nd Process Technology Conference*, TMS, Warrendale, PA, pp232, 1981.

[25] Martinez E, Maeda M, Heaslip LJ, Rodriquez G, McLean A, 'Effects of Fluid Flow on the Inclusion Separation in Continuous Casting Tundish', *Trans. Iron Steel Jpn*., Vol. 26, No. 9, pp. 724-731, 1986.

[26] Collur MM, Love DB, Patil BV, *Proc. of the Steelmaking Conf.,* TMS, Warrendale, PA, pp. 629, 1995.

[27] Ackerman J, Personal Communication, *Columbus Stainless Steel, Middelburg, South Africa,* 2002.

[28] Pretorius CA, Personal Communication, *ISCOR Vanderbijlpark, South Africa*, 2002.

[29] Spectro Analytical Instruments Inc., www.spectro.com, 2002.

[30] Zhang L, Thomas BG, 'State of the Art in Evaluation and Control of Steel Cleanliness', *Iron and Steel Institute of Japan Int.*, Vol. 43, No. 3, pp. 271-291, 2003.

[31] Fluent Inc., 'Fluent 6 Introductory Training Notes', 2003.

[32[Fluent Inc., *Gambit Version 2 Manuals*, Centerra Resource Park, 10 Cavendish Court, Lebanon, New Hampshire, USA, 2001 (www.fluent.com).

[33] White FM, *Viscous Fluid Flow*, 2nd Edition, McGraw-Hill International, New York, 1991.

[34] Stokes GG, 'On the Theories of Internal Friction of Fluids in Motion', *Trans. Cambridge Phil. Soc.*, Vol. 8, pp. 287-305, 1845.

[35] Bousinessq J, *Théorie Analytique de la Chaleur*, Vol. II, Gauthier-Villars, Paris, 1903.

[36] Zeytounian RKh, 'Joseph Boussinesq and his approximation: a contemporary view', *C.R. Mecanique*, Vol 331, pp. 575-586, 2003.

[37] Fluent Inc., *Fluent Version 6 Manuals*, Centerra Resource Park, 10 Cavendish Court, Lebanon, New Hampshire, USA, 2001 (www.fluent.com).

[38] Baldwin BS, Lomax H, 'Thin Layer and Approximation and Algebraic Model for Separated Turbulent Flow', *AIAA Paper 78-257*, 1978.

[39] Kline SJ, Morkovin MV, Sovran G, Cockrell D J, 'Computation of Turbulent Boundary Layers – 1968 AFOSR-IFP Stanford Conference', *Proceedings 1968 Conference*, Vol. 1, Stanford University, Stanford, California, 1968.

[40] Launder BE, Spalding DB, 'The Numerical Computation of Turbulent Flow', *Comp. Meth. in Appl. Mech. & Eng.*, Vol. 3, pp. 269-289, North-Holland Publishing Co., 1974.

[41] Rodi W, 'Influence of Boyancy and Rotation on Equations for Turbulent Length scale', *Proceedings of the 2nd Symposium on Turbulent Shear Flows*, 1979.

[42] El Thary SH, 'k-ε Equation for Compressible Reciprocating Engine Flows', *AIAA J. Energy*, Vol. 7, No. 4, pp. 345-353, 1983.

[43] Choudhury D, 'Introduction to the Renormalization Group Method and Turbulence Modeling', Technical Memorandum TM-107, Fluent Inc., 1993.

[44] Spalding DB, 'A Single Formula for the Law of the Wall', *Journal of Applied Mechanics,* Vol. 28, pp. 455-457, 1961.

[45] Launder BE, Reece BJ, Rodi W, 'Progress in the Development of a Reynolds Stress Turbulent Closure', *Journal of Fliud Mechanics*, Vol. 68, pp. 537-566, 1975.

[46] Kline S, Cantwell BJ, Liley GM, 'The 1980-1981 ASFOSR-HTTM Stanford Conference on Complex Turbulent Flows: Comparison of Computation and Experiment', Vols. 1-3, Mech. Engineering Dept., Stanford University, Stanford, California, 1982.

[47] Miki Y, Thomas BG, 'Modeling of Inclusion Removal in a Tundish', *Metallurgical and Materials Transactions B*, Vol. 30B, pp. 639-654, August 1999.

[48] Morsi SA, Alexander AJ, 'An Investigation of Particle Trajectories in Two-Phase Flow Systems', *Journal of Fluid Mechanics*, Vol. 55, No. 2, pp. 193-208, September 1972.

[49] Daly BJ, Harlow FH. 'Transport Equations in Turbulence', *Phys. Fluids*, Vol. 13, pp. 2634-2649, 1970.

[50] Miki Y, Thomas BG, Dennisov A, Shimanda Y, 'Model of Inclusion Removal During RH Degassing of Steel', *Iron and Steelmaker,* Vol. 24, No. 8, pp. 31-39, 1997.

[51] Snyman JA, *Introduction to Mathematical Optimisation*, Post-graduate course, Department of Mechanical and Aeronautical Engineering, University of Pretoria, South Africa, 1994.

[52] Snyman JA, *Practical Mathematical Optimization: An Introduction to Basic Optimization Theory and Classical and New Gradient-Based Algorithms,* Springer, New York, New York, 2005.

[53] Snyman JA, 'A New Dynamic Method for Unconstrained Minimization', *Applied Mathematical Modelling*, Vol. 6, pp. 449-462, 1982.

[54] Snyman JA, 'An Improved Version of the Original Leap-Frog Dynamic Method for Unconstrained Minimization LFOP1(b)', *Applied Mathematical Modelling*, Vol. 7, pp. 216-218, 1983.

[55] Snyman JA, Stander N, Roux W J, 'A Dynamic Penalty Function Method for the Solution of Structural Optimization Problems', *Applied Mathematical Modelling*, Vol. 18, pp. 453-460, August 1994.

[56] Snyman JA, Frangos C, Yavin Y, 'Penalty Function Solutions to Optimal Control Problems with General Constraints via a Dynamic Optimisation Method', *Computer & Mathematics with Applications*, Vol. 23, pp. 46-47, 1992.

[57] Snyman JA, 'The LFOPCV3 Leap-Frog Algorithm for Constrained Optimisation', *Computers & Mathematics with Applications*, Vol. 40, pp. 1085-1096, 2000.

[58] Snyman JA, Stander N, 'A New Successive Approximation Method for Optimum Structural Design', AIAA Journal, Vol. 32, pp. 1310-1315, 1994.

[59] Snyman JA, Stander N, 'Feasible Descent Cone Methods for Inequality Constrained Optimisation Methods in Engineering', *International Journal for Numerical Methods in Engineering*, Vol. 38, pp. 119-135, 1995.

[60] Snyman JA, Hay AM, 'The Dynamic-Q Optimization Method: An alternative to SQP?', *Computers & Mathematics with Application*, Vol. 44, No. 14, pp. 1589-1598, 2002.

[61] Snyman JA, *Private Communication*, Department of Mechanical and Aeronuatical Engineering, University of Pretoria, Pretoria, South Africa, 1998.

[62] Stander N, Craig KJ, 'On the robustness of a simple domain reduction scheme for simulation based optimization', *Engineering Computations*, Vol. 19, No. 4, pp. 431-450, 2002.

[63] Stander N, Eggleston TA, Craig KJ, Roux W, *LS-OPT User's Manual Version 2*, Livermore Software Technology Corporation, Livermore, CA, (October 2003).

[64] Myers RH, Montgomery DC, *Response Surface Methodology*, Wiley, New York, 1995.

[65] Venter PJ, Craig KJ, Hasse GW, De Kock DJ, Ackerman J, 'Comparison of Water Model and CFD Results for a Single-Strand Continuous Caster', *Mechanical Technology*, April 2000.

[66] Hasse G.W., Design, Construction, Commissioning & Initial Experimental Tests for a Full Scale Tundish Water Model, Technical report, Gübau cc., July 1999.

[67] UFM 600 User Manual, Krohne Altosonic, The Netherlands, 1990.

[68] De Kock DJ, Craig KJ, Pretorius CA. 'Mathematical Maximisation of the Minimum Residence Time for a Two-Strand Continuous Caster', *Ironmaking and Steelmaking*, Vol. 30, No. 3. pp. 229- 234, 2003.

[69] Craig KJ, De Kock DJ, Makgata KW, De Wet GJ, 'Design Optimization of a Single-strand Continuous Caster Tundish Using Residence Time Distribution Data', *Iron and Steel Institute of Japan Int.*, Vol. 31, No. 10, pp. 1194-1200, 2001.

[70] Craig KJ, De Kock DJ, Snyman JA, 'Continuous Casting Optimization using CFD and Dynamic-Q', *20th International Congress of Theoretical and Applied Mechanics*, Chicago, 27 August – 2 September 2000.

[71] Pretorius CA, *Personal Communication*, ISCOR Vanderbijlpark Works, South Africa , 2000.

[72] De Kock DJ, Craig KJ, Pretorius CA. 'Mathematical Maximisation of the Minimum Residence Time for a Two-Strand Continuous Caster', *Proceedings of the 4th European Continuous Casting Conference,* Birmingham, United Kingdom, pp. 84-93, 14-16 October 2002.

[73] Mills AF, *Basic Heat and Mass Transfer*, 2nd Edition, New Jersey, Prentice-Hall Inc., 1999.

[74] Craig KJ, De Kock DJ, De Wet GJ, Haarhoff LJ, Pretorius CA, 'Design Optimization of Continuous Caster Refractory Components', submitted, *ASME 2005 International Design Engineering Technical Conferences and Computers and Information in Engineering Conference*, Long Beach, California, USA, September 2005.

[75] US Patent Number 6159418, 'Tundish Impact Pad', Foseco International Ltd., Wiltshire, United Kingdom, 12 December 2000.

[76] Craig KJ, De Kock DJ & De Wet GJ, 'CFD Analysis of the Single-strand Tundish of Columbus Stainless – Modelling of New Tundish (with 150mm lining) with Existing Turbostop and Baffle', Internal Report to Columbus Stainless, 2002.

[77] Venter PJ, Craig KJ, Hasse GW, De Kock DJ, Ackerman J, 'Comparison Of Water Model and CFD Results for a Single-Strand Continuous Caster', *Proceedings of International Conference on Applied Mechanics*, Durban, South Africa, 2000.

[78] Orban W, Technical Note, Columbus Stainless (Pty) Ltd, 2004.

[79] De Beer G, 'Trial 155: Trial on "Cash Register" tundish furniture', Columbus Stainless (Pty) Ltd, Internal Report, January 2004.

[80] De Beer G, 'Trial 155: Trial on "Cash Register" tundish furniture (Progress report 1)', Columbus Stainless (Pty) Ltd, Internal Report, June 2004.